Fermilab Library
0 1160 0020100 8

INTERACTIONS OF HADRONS WITH HEAVY NUCLEI AT 200 GEV/C

By ROBERT LOUIS DIMARCO

PHYSICS DEPARTMENT

RUTGERS
THE STATE UNIVERSITY
OF NEW JERSEY

LIBOFFCE
FERMI
THESIS

FERMILAB
LIBRARY

E 565/570

INTERACTIONS OF HADRONS WITH HEAVY NUCLEI AT 200 GEV/C

By ROBERT LOUIS DIMARCO

A dissertation submitted to the

Graduate School-New Brunswick

Rutgers, The State University of New Jersey

in partial fulfillment of the requirements

for the degree of

Doctor of Philosophy

Graduate Program in Physics

Written under the direction of

Professor Richard J. Plano

and approved by

Richard J. Plano

John J. Brennan

Jacques Kollar

Mohan S. Kalelkar

New Brunswick, New Jersey

May 1985

FERMILAB
LIBRARY

1185945

ABSTRACT OF THE THESIS

Interactions of Hadrons With

Heavy Nuclei at 200 GeV/c

by Robert Louis DiMarco

Dissertation Director: Professor Richard J. Plano

We study hadron-nucleus collisions using a tagged beam of 200 GeV/c π^+, K^+ and p on Mg, Ag and Au targets. This data was taken using the Fermilab 30" bubble chamber filled with liquid H_2, and the Fermilab hybrid spectrometer. A method is presented for reconstructing charged tracks from events of all multiplicities. This method yields a sample of 461 events for all beams and targets with a minimum bias in the multiplicities. A sample of complete and charge balanced H_2 events is used for comparison. Calculated cross-sections from this sample are consistent with previous published values. Average charged particle multiplicities are presented. The average net charge and average identified protons are studied and compared to previous results based on scan data from this experiment. We conclude that the net positive charge at low momentum is due to protons and not to an excess of positive pions. The charged particle multiplicity, net charge and secondary collisions are examined as a function of projectile collisions. The slope of the multiplicity distribution is constant for all beams and targets within our statistics. There is no evidence in our data for an increase in multiplicity versus projectile collisions for K^+ interactions as has been reported elsewhere. Net

charge and secondary collisions depend on target type as well as on the number of projectile collisions. Normalized rapidity distributions are presented and compared to those for H_2. The rapidity differences are explained in terms of the formation length for charged secondaries.

ACKNOWLEDGMENT

It is a pleasure to acknowledge some of the many people who helped me with this research. First I thank Dorte Jensen, my wife, for her unwavering support through many years. A special thanks also goes to my scanning and measuring crew, Amos Danube, John Doroshenko and Julia Sotory, who did a beautiful job on these difficult events.

An experiment like E565/570 does not run without the hard work of many people; in this case those people were the Fermilab bubble chamber crew and my colleagues in the International Hybrid Spectrometer Consortium. I also thank my fellow graduate students, Jim Bober, Tom Frank, Rob Steiner and Victor Suchorebrow for their companionship and aide during the days at Fermilab.

I thank my adviser Richard Plano for teaching me physics and programming; and my other professional friends at Rutgers, E. B. Brucker, Pieter Jacques, Mohan Kalelkar, Len Koller and Pete Stamer for their help and encouragement over the years.

Title page.....i

Abstract.....ii

Acknowledgment.....iv

Table of contents.....v

List of tables.....vii

List of illustrations.....viii

1) Introduction.....1

2) Experimental apparatus.....13

2.1) Beam.....13

2.2) Upstream spectrometer.....13

2.3) Bubble chamber.....16

2.4) Downstream spectrometer.....24

2.5) Coordinate systems.....28

2.6) Online data handling.....30

2.7) Data-taking.....31

3) Event processing.....32

3.1) TRIFID.....36

3.2) Measuring.....42

3.3) PRECIS.....49

3.4) GEOHYB.....54

3.5) DST and ID scan.....61

4) Analysis.....66

4.1) Data sample.....66

4.2) Cross-sections.....73

4.3) Multiplicity.....76

4.4) Net charge and observed protons.....80

4.5) Projectile collisions.....89

4.6) Rapidity shifts.....97

5) Conclusion.....102

Appendicies.....106

A) PIG.....106

B) SOW.....115

References.....119

Vita.....121

Tables

2-1: Beam identification.....17

2-2: Physical parameters of metal plates.....21

3-1: Main additions to plate processing chain.....35

4-1: Nonbiased rejects.....67

4-2: Biased rejected events.....69

4-3: Final analysis sample.....71

4-4: Track summary.....72

4-5: Quantities used in cross-section calculation.....74

4-6: Cross-sections in millibarns.....75

4-7: Quantities for calculating multiplicity correction factor...78

4-8: Average multiplicities.....79

4-9: Average net charge.....81

4-10: Net charge and protons binned by momentum.....84

4-11: Average number of projectile collisions by beam and target.90

4-12: Aerage rapidity for pions and protons.....99

Figures

1-1: Proton-nucleus interaction with 2 projectile collisions.....10

2-1: Upstream spectrometer arm.....14

2-2: Fermilab 30" bubble chamber.....18

2-3: Plate holder and plates.....20

2-4: 30" bubble chamber and camera ports.....22

2-5: Downstream spectrometer.....25

2-6: Angles of downstream wire chamber planes.....27

3-1: Processing chain for hydrogen events.....33

3-2: Processing chain for plate events.....34

3-3: Sample TRIFID output.....40

3-4: Sectioning example, view 1.....45

3-5: Sectioning example, view 2.....46

3-6: Sectioning example, view 3.....47

3-7: Light ray geometry.....57

3-8: Light rays for sections 57, 51, and 52 of frame 448320.....58

3-9: Vertex errors for sectioned events.....60

4-1: Topology distributions for nonrejected events, nonbiased rejected events and biased rejected events.....68

4-2: Net charge less than p versus p.....83

4-3: Protons with momentum less than p versus p.....86

4-4: Positive pions with momentum less than p versus p.....87

4-5: Net charge of pions with momentum less than p versus p.....88

4-6: Average multiplicity versus projectile collisions.....91

4-7: Net charge versus projectile collisions.....94

4-8: Secondary collisions versus projectile collisions.....95

4-9: Normalized rapidity distribution for hydrogen, Mg, Ag, Au.....98

4-10: Average rapidity versus average projectile collisions.....101

A-1: PIG hybridizations.....114

1) INTRODUCTION

For many years people have realized that studying hadron-nucleus collisions at high energy can yield useful insights into strong interaction physics. At first glance this might seem surprising since simple hadron-nucleon collisions are not understood in detail and hadron-nucleus interactions allow for even more complexity. The presence of additional scattering centers in the nucleus does add to the complexity, but by studying the features of recollisions of the projectile or collisions of secondary particles we can gain insight on the time evolution of the interaction. We can examine the state of the projectile and produced particles at short times because of the possibility of these extra collision at short distances. Experimental analysis in this field has been aimed at separating the effects of interactions of the beam particle (projectile interactions) and interactions of particles produced in projectile interactions (secondary interactions). This thesis reports a study of π^+, K^+, and p interactions with H_2, Mg, Ag, and Au targets at 200 GeV/c. In this introduction we will begin by discussing an intuitive picture of the hadron-nucleus interaction due to Busza (ref. 1) emphasizing these points. Next we will discuss methods of counting the various kinds of collisions. A short review of theoretical approaches and recent experiments follows.

It will be useful to describe a particle by its rapidity. The rapidity of a particle along an axis is defined as:

$y = \frac{1}{2} \ln \left(\frac{E + p}{E - p} \right)$, where p is the component of momentum along the axis and E is the particle's energy. A Lorentz

transformation with speed $v=\beta c$ along the rapidity axis corresponds to a change in rapidity: $y^* = y - \frac{1}{2} \ln \left(\frac{1+\beta}{1-\beta}\right)$. Thus the shape of a rapidity distribution will be invariant under a parallel Lorentz boost. Rapidity is a measure of the particle's motion relative to the reference frame. We usually work in a center of mass frame of the beam target system where the target is always assumed to have the proton mass. In this system the beam rapidity is about 3 (proton beam) and the target about -3 rapidity units, for the experiment on which this thesis is based.

One way to look at hadron-nucleus interactions is to consider the interactions as viewed in the rest frame of produced particles (ref. 1). We will look at three cases; the secondaries have rapidity near that of the projectile, the secondaries are at rest in the center of mass (rapidity far from either projectile or target), and the secondaries have rapidity near the target. In the first case, since the beam rapidity is close to that of our reference frame, the beam is moving very slowly. The target however is far away in rapidity, moving very quickly through the interaction and highly Lorentz contracted (see below). In this picture each line represents a

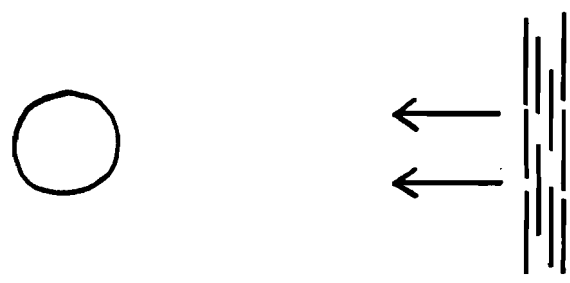

contracted nucleon in the nucleus, the circle on the left represents the beam particle. Secondaries produced in this frame will not have a chance to interact in the the nucleus because the nucleus will be beyond them before they form. They can recombine with pieces of the

beam since these fragments move slowly in this frame. Another way to say this is that the formation length, which is proportional to $\frac{1}{\lambda}$ (λ is the Compton wavelength), increases with momentum (ref. 2). At high energy the formation length is greater then the absorption length of the nucleus or even the radius of the nucleus. The beam particle itself can interact repeatedly with different nucleons since it already exists. In this rapidity range we will see a) secondaries which could not have reinteracted in the nucleus, and b) fast beam fragments. This rapidity range is called the leading particle or beam fragmentation region.

In the second case we are at rest in the center of mass system. Both the beam and target are highly Lorentz contracted and will move rapidly through the interaction. Secondaries produced in this region

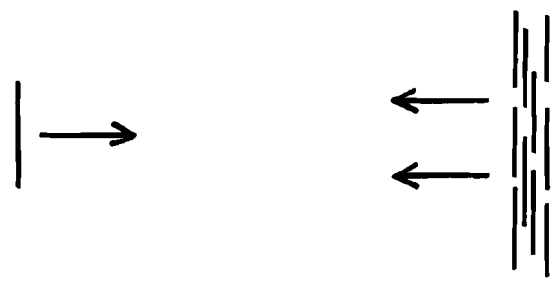

will recombine without reinteracting. Also there will be no beam or target fragments to help determine the hadronization. Particles produced in this rapidity region, called the central or central field region, should not depend on the beam or target type but only on the amount of energy left in the field of the passing beam and target.

Finally, there is the target fragmentation region. Here the nucleus has rapidity close to that of the reference frame and the beam will move rapidly through. Secondaries produced in this rapidity range will be formed inside the nucleus. They will have the opportunity to interact with other nucleons before leaving the

nucleus. Each interaction will produce more slow secondaries which can then also interact. Thus, the presence of slow particles can lead

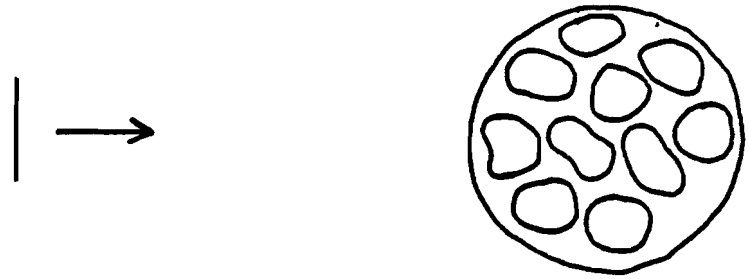

to a cascade of interactions that will depend on the size of the nucleus and the impact parameter of the original hadron-nucleus interaction. This target fragmentation region should contain slow particles (in the lab) with many coming from secondary interactions inside the nucleus.

In practice these three separate pictures are not distinct but are joined by a continuum of intermediate possibilities. This way of looking at the interaction nicely emphasizes the important distinction between projectile and secondary collisions inside the nucleus. A projectile collision is an interaction between the incident beam particle and a nucleon in the nucleus; the projectile may interact with more than one nucleon and in general it does. The number of projectile collisions is a measure of the thickness of the nucleus at the point of the interaction. The impact parameter is inversely related to the number of projectile collisions. A small impact parameter means that the beam interacted near the center of the nucleus and so statistically will have the maximum number of projectile collisions. In projectile collisions the difference in rapidity between the projectile and target is large. Secondary collisions occur when a particle produced in a projectile collision has a rapidity close enough to that of the target so that it is formed

inside the nucleus and then interacts before leaving. Secondary collisions can also occur between a particle formed in another secondary collision and the nucleus. There is clearly a possibility of different physics going on in these two types of collisions. For example, their dependence on beam and target type might be different. The general feeling in the field is that secondary collisions can be understood with simple cascading models and that the processes of interest are the projectile collisions. How can we tell if a particle is the result of a projectile or secondary collision? This is the key question currently being studied on the experimental side.

For a given event there is no sure way to tell the exact number of projectile collisions (ν_p) that occurred. We can define for a given beam type (h) and target nucleus (A) the quantity $\langle\nu_p\rangle_{hA}$ which is the average number of projectile collisions. It can be shown (ref. 2) that:

$\langle\nu_p\rangle_{hA} = \frac{A\ \sigma_{hN}}{\sigma_{hA}}$ where σ_{hN} and σ_{hA} are the inelastic cross-sections for hadron-nucleon and hadron-nucleus collisions. This average value has a large dispersion $\langle\nu_p^2\rangle_{hA} - \langle\nu_p\rangle_{hA}^2 = 0.5\ \langle\nu_p\rangle^2_{hA}$ (ref. 3); and so is not too useful when examining individual events.

Several groups have tried to correlate the number of projectile collisions with some observable in the event. One proposal is to relate ν_p to the number of protons seen in the event (n_p) (ref. 3,4). This type of relation, $\nu_p(n_p)$, is useful for bubble chamber, streamer chamber and emulsion experiments where all tracks are seen and slow protons can be identified by their ionization in the visible medium. Each of the groups working on this problem uses a model of the nucleus

to predict a relation between ν_p and n_p and also the expected probability distribution of protons $P(n_p)$. The prescriptions arrived at are all similar and one group Chao et al. (ref. 5) have come up with a simple analytical formula:

$$\nu_p(n_p) = \langle\nu_p\rangle_A \sqrt{\frac{n_p}{\langle n_p\rangle}} \quad .$$

Other groups have also used this formula and found it in good agreement with their data (ref. 6). Because of uncertainties in identifying protons and statistical uncertainties in the theory this function is only true on average; but the dispersion is much smaller than using just $\langle\nu_p\rangle_A$. Chao et al. claim:

$\langle\nu_p^2(n_p)\rangle - \langle\nu_p(n_p)\rangle^2 \approx 0.4\ \langle\nu_p(n_p)\rangle$. There are several advantages in using $\nu_p(n_p)$ over $\langle\nu_p\rangle_A$, the most important is that we can unambiguously group the events into bins which make sense. Using $\langle\nu_p\rangle_A$ we are averaging over events which range from a few tracks to over seventy tracks; clearly something different is occurring at these two extremes. $\nu_p(n_p)$ allows us to parameterize this difference. Another advantage is that the largest value of $\langle\nu_p\rangle_A$ is about 4 for uranium; using $\nu_p(n_p)$ we can examine events where ν_p is greater than 7. We will see in the analysis section of this thesis that certain features of the events seem to depend only on ν_p while other features also depend on beam or target type.

Each collision in the nucleus, whether projectile or secondary, must conserve charge. So at each collision the average net charge of the secondaries goes up by $\frac{Z}{A}$. Once we have a handle on the number of projectile collisions we can calculate the number of secondary

collisions knowing the average net charge of the events (which we measure). This will be done in the analysis section.

Theories of hadron-nucleus interactions may be grouped into general categories depending on how they treat the projectile collisions. Collective models treat the interaction as having only one collision between the incoming hadron and some effective "target" which depends on how many nucleons were struck in the nucleus. Other theories consider the collisions separately but do not explicitly consider what is colliding. Finally there are models which treat the collisions explictly as quark-quark (or parton-parton) interactions. In spite of their various starting assumptions, models in each of these categories fit the available data (ref. 5). In part this is due to lack of precision in the data and in part to the nebulous predictions of the models.

An example of a successful collective model is the "coherent tube" model of Berlad, et al. (ref. 7). In this model the beam is assumed to collide only with those nucleons in a cylinder around its path. The interaction is assumed to be a single collision between the beam and a particle whose mass is equal to the sum of masses of the nucleons in the tube. All physical quantities are parameterized by the available energy in the center of mass of the beam-target system. The number of nucleons struck depends on the impact parameter and the effective target mass is simply $M = \nu_p$ * (proton mass).

The "energy flux" model of Gottfried (ref. 8) treats the collisions separately. After the first collision in the nucleus the projectile breaks up into an energy flux cylinder expanding with time as it leaves the nucleus. This cylinder will eventually break up into

hadrons, but it can interact with other nucleons in the nucleus before it hadronizes. For simplicity it is assumed that the flux will scatter into two fluxes with different momenta fractions at each collision. Gottfried shows that the flux which will become the leading particle interacts almost as if it were still a real particle due to its lack of spreading. Both this model and the one described in the preceding paragraph are not very satisfying physically. They contain parameters which cannot be independently calculated but must be fit from the data. They cannot be ruled out by the present data, and are useful to point out regularities in the data, but they are unlikely candidates for a complete description of hadron-nucleus interactions.

The additive quark model of Nikolaev and Ostapcheck (ref. 9) and the dual parton model of Capella and Tran Thanh Van (ref. 10,11) are both based on interactions of single quarks (partons) in the beam and nucleus. While presenting a much more sensible picture of the interaction they contain much more detail and cannot be completely calculated. They do however, offer the hope of a complete description of hadron-nucleus interactions based on the standard model. In the additive quark model, each collision is an interaction between a quark in the projectile and a quark in a nucleon in the nucleus. The hadronization process can be broken into two steps which have different characteristic lengths. First new quarks will be formed. They will have probabilities described by the fragmentation functions that depend both on the quarks in the collision and the spectator quarks. After this step the quarks recombine to form hadrons. The characteristic length for the second process is long compared to that

of the first, so the two are treated separately. The formation length for the quarks is the length discussed earlier in our intuitive picture; it may be longer or shorter than the nucleus depending on the momentum of the quark being produced. In this model each quark in the projectile may only interact once in the nucleus. This would seem to cause trouble since the maximum number of projectile collisions for a proton beam would be 3 (2 for a meson beam) while we have seen that even on average some nuclei have more collisions ($\langle\nu_p\rangle = 4$ for U). Actually, as explained in reference 9, because of the formulation of the fragmentation functions in terms of both the leading and spectator quarks the quantity to compare with ν_p is the number of collisions times the number of quarks. This way the predictions of the behavior with ν_p match the experimental data. The theory explicitly takes into account the fact that some of the quarks are formed inside the nucleus and can recollide. Although the model cannot be calculated in detail, by using reasonable fragmentation and recombination functions it agrees quite well with the data.

The key difference between the additive quark and dual parton models can be seen in figure 1-1 which shows a hadron-nucleus interaction with two projectile collisions in each model. In the dual parton model the quark-antiquark chain between the projectile and target quarks appear twice (the outside chains) no matter how many collisions take place. Each additional collision adds two more chains between a sea quark and the target and a sea antiquark and the target (the inside chains). Final particle rapidity distributions are formed by summing up the contributions from each chain. To do this one needs to know the momentum distribution of the end quarks in the chain (this

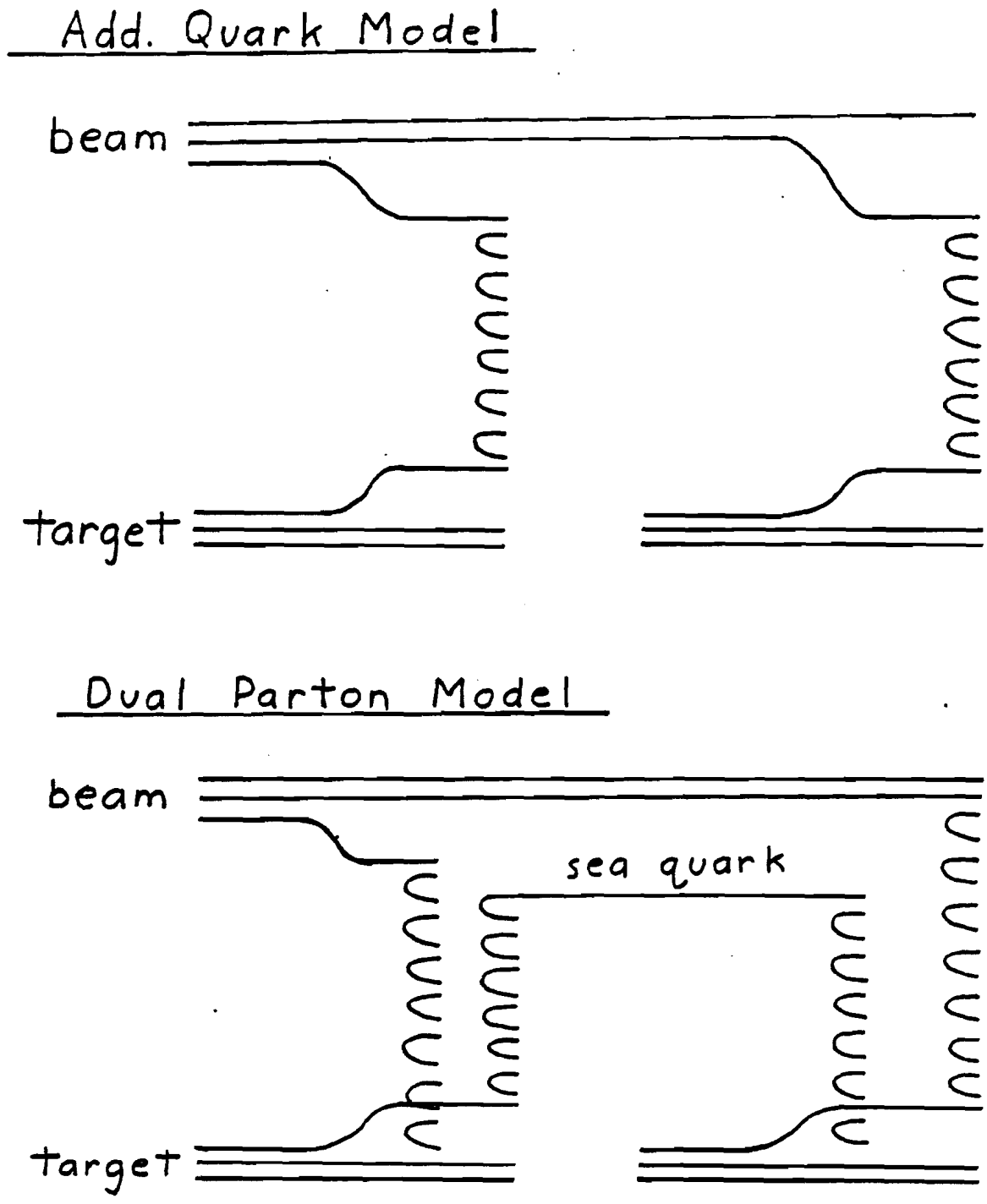

Figure 1-1: Proton-nucleus interaction with 2 projectile collisions.

means knowing the distribution in the beam, target and sea), and the fragmentation function of quarks into hadrons. As with the additive quark model, many details of the experimental rapidity distributions can be calculated, but only by assuming the fragmentation functions.

Several reviews of the experimental effort in this field have been published recently (ref. 1,12,13). There are two general kinds of experiments; counter experiments which we will not consider, and visible detector experiments of which the data presented here is one. New results from a number of visual detector groups using high energy beams have been presented lately. These experiments all include 4π particle tracking, momentum and charge data, and proton identification at low momentum. I will briefly discuss these experiments here. Later, in the analysis section, I will refer back to data from these experiments. Recall that the results presented here are 200 GeV/c π^+, K^+ and p on Au, Ag, Mg, and H_2. This experiment has presented results previously in references 14 and 15, based on scan data.

Several groups have used bubble chambers filled with a liquid neon-hydrogen mixture to record hadron-nucleus interactions at high energy. W. M. Yeager, et al. (ref. 16), used the 82" bubble chamber at SLAC to do π^--Ne and π^+-Ne at 10.5 GeV/c. Another group used the 30" bubble chamber at Fermilab (prior to our experiment) for p-Ne at 300 GeV/c (ref. 17).

Metal plates mounted in a hydrogen bubble chamber were used to make a visible high A target by some experiments other than our own. E597 which ran sandwiched between our two runs used this technique. They used our detectors except the FGD was replaced by a large segmented Cerenkov counter and a neutral hadron calorimeter. They

studied π^-, π^+, K^+, $\bar{p}$ and p at 100 GeV/c and π^- at 320 GeV/c; their targets were the same as ours. Since we used mostly the same equipment, their data will be comparable to ours. E597 presented some preliminary results in reference 18. The NA22 collaboration at CERN has also started to release hadron-nucleus data, but so far their results have only included scan data (no measurements). This experiment used the rapid cycling bubble chamber at CERN and the EHS spectrometer. The beam was 250 GeV/c π^+, and K^+; the targets were aluminum (A = 27) and gold (A = 197), see reference 6.

A recent streamer chamber experiment at the CERN SPS used gas filled tubes as targets. Their beam was 200 GeV/c protons and antiprotons on targets of hydrogen, argon (A = 40), and xenon (A = 131). There was a magnetic field over the chamber for momentum and charge determination. In the streamer chamber they could identify protons only up to 600 MeV/c. This group has recently published several papers (ref. 19,20) and their data has also been analyzed by Klar and Hufner (ref. 21). They currently have seven times more events measured than we do but we have a larger spread in A which enables us to go to larger ν_p even with our lower statistics. Our data is also different in that we have a meson beam.

2) EXPERIMENTAL APPARATUS

2.1) BEAM

E565/570 occupied the N7 beamline in the Fermilab neutrino area during the '80-'81 and '81-'82 running periods. In this beamline primary protons from the main ring at 400 GeV/c strike a target producing a secondary beam of mixed π, K, and p. These secondaries are then momentum and sign selected, giving a 200 GeV/c π^+, K^+, p beam (with some muon contamination). During each accelerator cycle one spill of particles was sent to the target. This spill lasted one second and was divided into sections called pings. In a ping the particles occur during 30 μsec and the rest of the time is used to read out the detectors. While taking data we ran with six pings per spill, so the readout time was 160 msec. Within the ping beam tracks occurred randomly with time spacings varying from 10 usec to nanoseconds. At the end of each ping one bubble chamber (BC) picture was taken unless the ping contained zero beams or more than ten beams.

2.2) UPSTREAM SPECTROMETER

For each incoming beam it is necessary to identify the beam type and to separate interactions of that beam from any previous or subsequent beams. This was the job of the upstream spectrometer arm. The upstream arm consisted of scintillator counters for time separation, proportional wire chambers (PWCs) for spatial separation, and Cerenkov counters ($\check{C}$) to determine beam type. See figure 2-1.

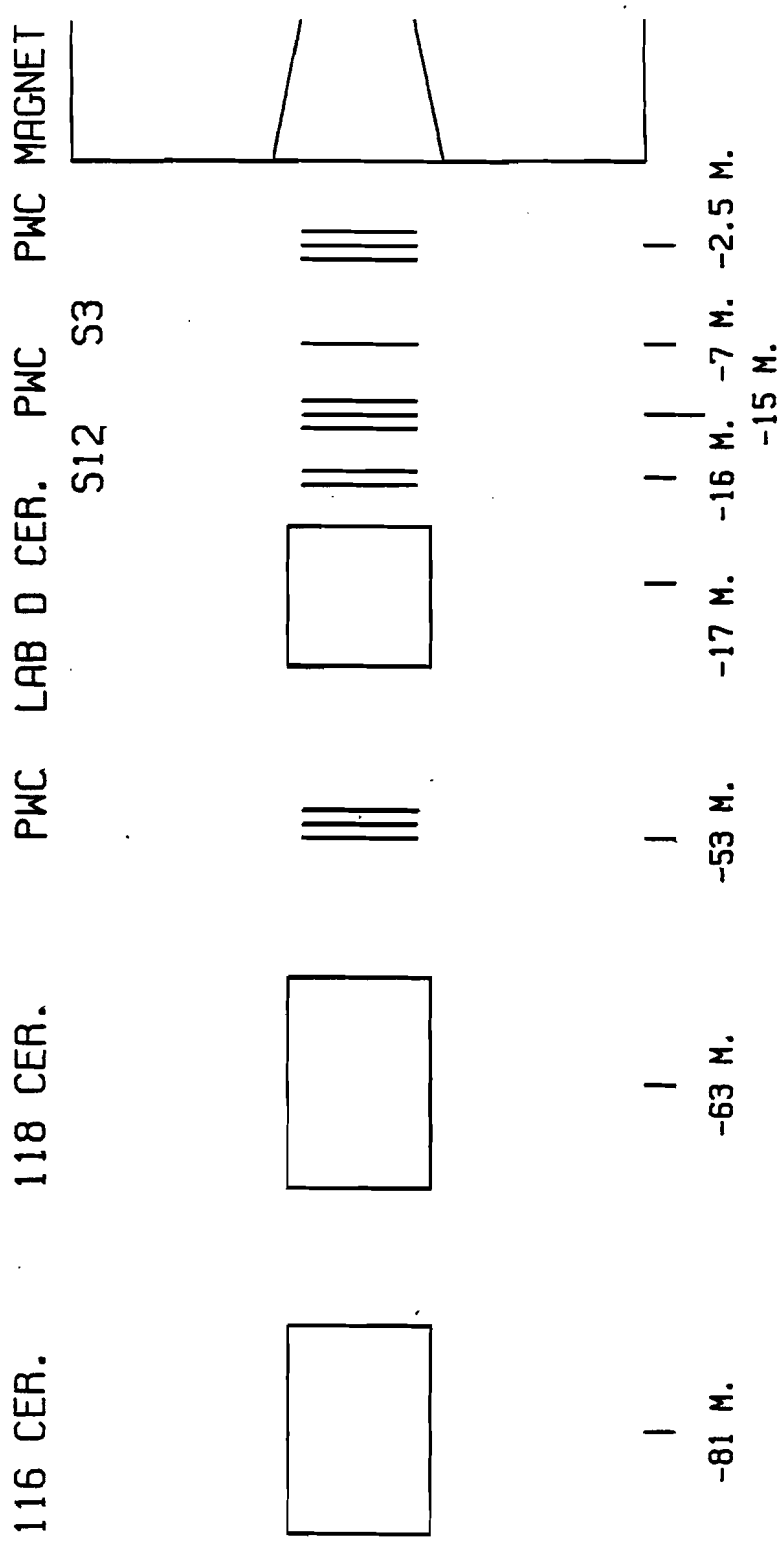

Figure 2-1: Upstream spectrometer arm.

The scintillator paddles were used to determine when a beam particle went through the system. As shown in figure 2-1 there were three paddles upstream. Signals from these paddles were placed in a 3-fold coincidence circuit. A charged particle traveling down the beamline will fire all paddles; this produces a pulse in the coincidence circuit called a master gate (MG) which defines the beam time. This MG signal was used to strobe data and start drift clocks in the detectors, as will be described later. The detector data associated with a particular master gate is called a time slot. The MG was 50 nsec wide, two beam tracks occurring within this time span would not be resolved. We know however that this happened less then 1% of the time, so this problem is ignored in the following.

There were nine planes of PWCs in the upstream arm, arranged into three triplets. Each plane had 48 channels with 2 mm wire spacing giving a square active area of 9.6 cm x 9.6 cm. During a ping each successive MG strobed the address of all activated wires occurring in coincidence with the MG into a random access memory (RAM). The RAMs could store up to 16 MG per ping. Data was read out between pings by a microprocessor which scanned the RAMs for stored hits.

The upstream chambers used the same frames as were used in E154, and E299. With equipment in the Fermilab beam chamber shop we rewound both sense and high voltage planes on these chambers. The gas mixture used in the upstream chambers was Ar, CO_2, and BrFreon. A discussion of the efficiency of these chambers can be found in ref. 22. For a typical beam these chambers allowed a position determination to 0.5 mm, and an angle determination to 0.02 mrad.

The mass of each beam particle was determined using the three cerenkov counters (see fig. 2-1). The furthest downstream counter was a threshold counter called the lab D $\check{c}$. The mirror was set to separate pions from kaons or protons at 200 GeV/c (pions giving a positive signal). Due to vacuum problems the efficiency of this counter was lower than the other two and its signal was used as a backup. The next counter was located in beamline enclosure 118, and so called the 118 $\check{c}$. This was a differential counter set to separate protons (inner mirror) from pions or kaons (outer mirror). There was another counter in the 116 beamline enclosure (116 $\check{c}$). 116 $\check{c}$ was also a differential counter but it was run as a threshold counter redundant with the lab D $\check{c}$. Pions gave a signal on the inner mirror, or the outer mirror, or both mirrors. Kaons and protons gave no signal. Hits on the mirror of the lab D $\check{c}$, and on the inner and outer mirrors of the 116 $\check{c}$ and 118 $\check{c}$ were treated as extra channels in the upstream PWC readout and so were automatically associated with their proper MG. The scheme used to determine beam type is shown in table 2-1. Beam composition for the data analysed here was 43% π^+, 14% K^+, 30% p, and 13% unidentified.

2.3) BUBBLE CHAMBER

E565/570 used the Fermilab 30" bubble chamber filled with liquid H_2 as a visual detector, fig. 2-2. The H_2 provided a target as well as a medium for growing bubbles. Metal plates were also placed in the BC as targets. The 30" BC has had a long and successful career as a

	118 $\check{c}$		116 $\check{c}$		Lab D $\check{c}$
Pion	outer mirror	and	any signal	or	any signal
Kaon	outer mirror	and	no signal	and	no signal
Proton	inner mirror	and	no signal	and	no signal
Junk		any other combination			

Table 2-1: Beam identification.

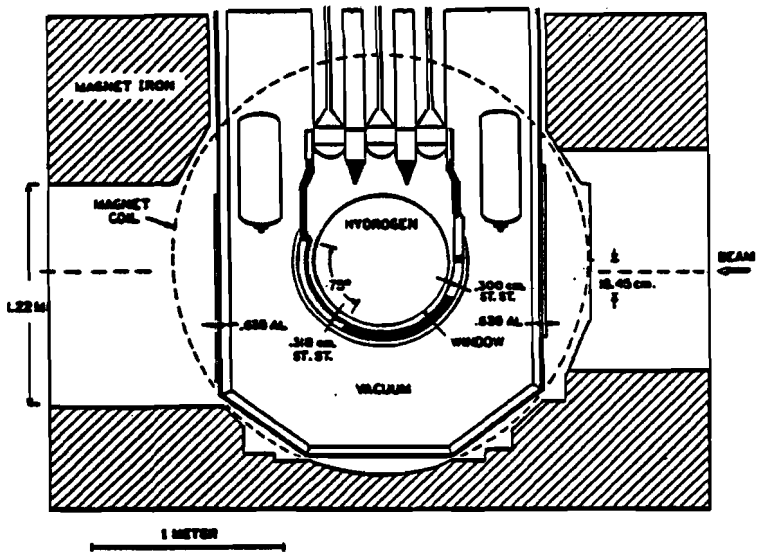

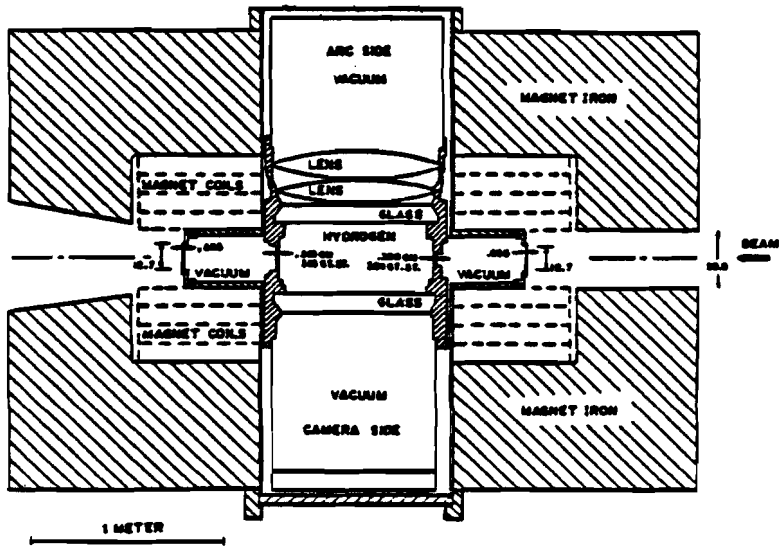

Figure 2-2: Fermilab 30" bubble chamber.

physics detector, and it was decommissioned after completion of this experiment.

The metal plates were added to this experiment so that interactions of hadrons with nuclei of various A could be compared to hadron-proton interactions with limited systematic errors. There were six plates, two each of Mg, Ag, and Au (see figure 2-3). The thicknesses were selected such that the thin plate of each element had the same interaction cross-section for beams. The second plate of each kind was three times as thick as the first. By comparing the results between the two plates of the same metal we could see any effects of secondary interactions in the plates. Parameters for the metal targets are shown in table 2-2.

We placed the plate holder behind the BC entrance window. The beam was narrow in the direction along the plates so that no beams struck the holder. Although the beam was spread in the other dimension most of the beam hit only plates one through four. The magnesium plates have some events but not as many as the silver and gold plates.

There were four camera ports used while we were taking pictures, see figure 2-4. We had three normal 30" BC cameras and a special high resolution camera, built at MIT, which gave a greater resolution with a concurrent loss of depth of field. In the 30" BC the flash system is set up so that only scattered light will reach the film. We look at the negative image so bubbles appear dark against a light background. The metal plates keep light scattered from bubbles behind them from reaching the film, and also keep light from the flashlamps from reaching bubbles in their shadow. On the negative film, this

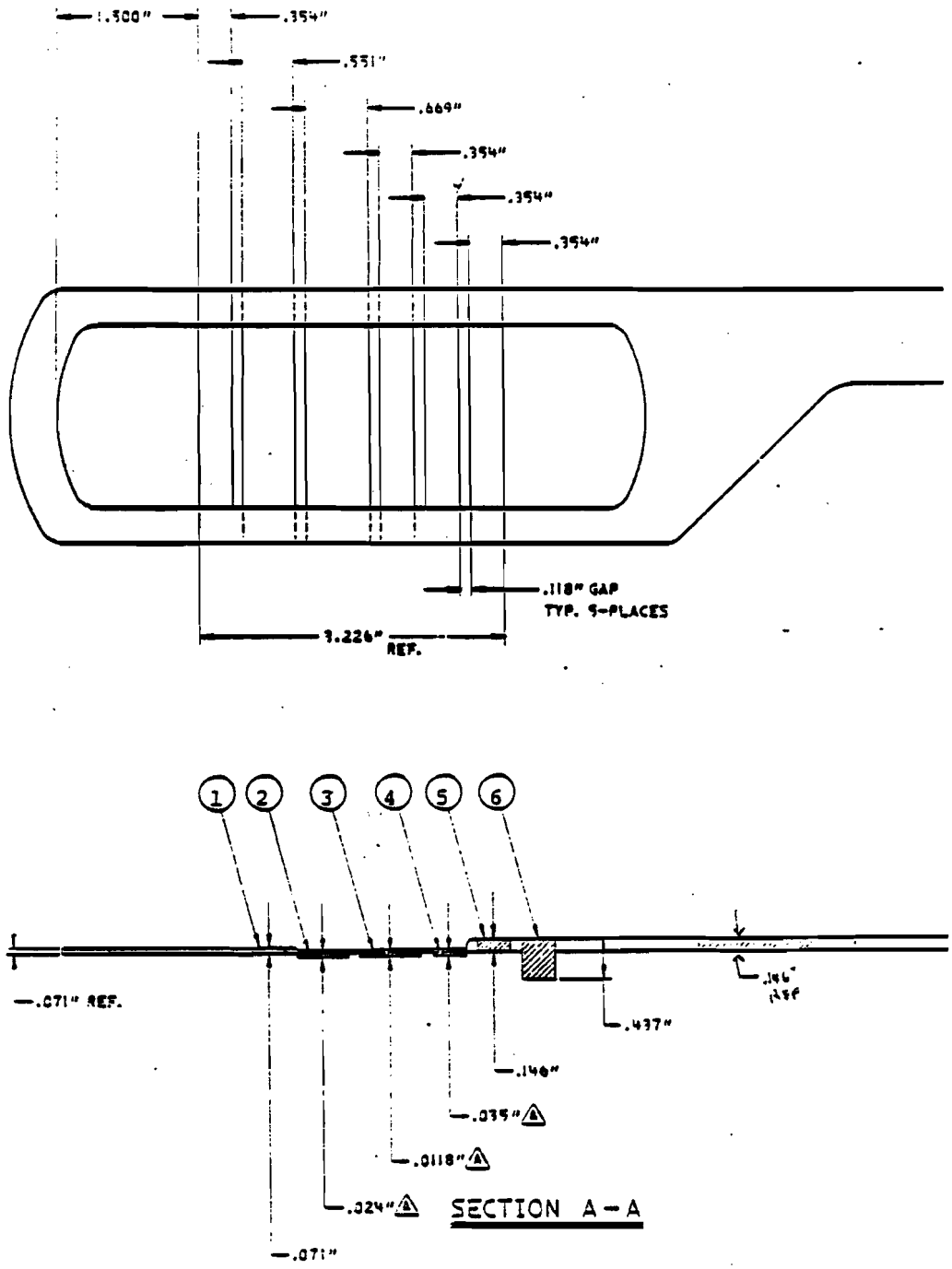

Figure 2-3: Plate holder and plates.

Plate	Element	A	Thickness (mm)	Density (gm/cm^3)
1	Ag	107.868	1.8	10.49
2	Ag	107.868	0.6	10.49
3	Au	196.996	0.3	18.88
4	Au	196.996	0.9	18.88
5	Mg	24.305	3.7	1.74
6	Mg	24.305	11.1	1.74

Table 2-2: Physical parameters of metal plates.

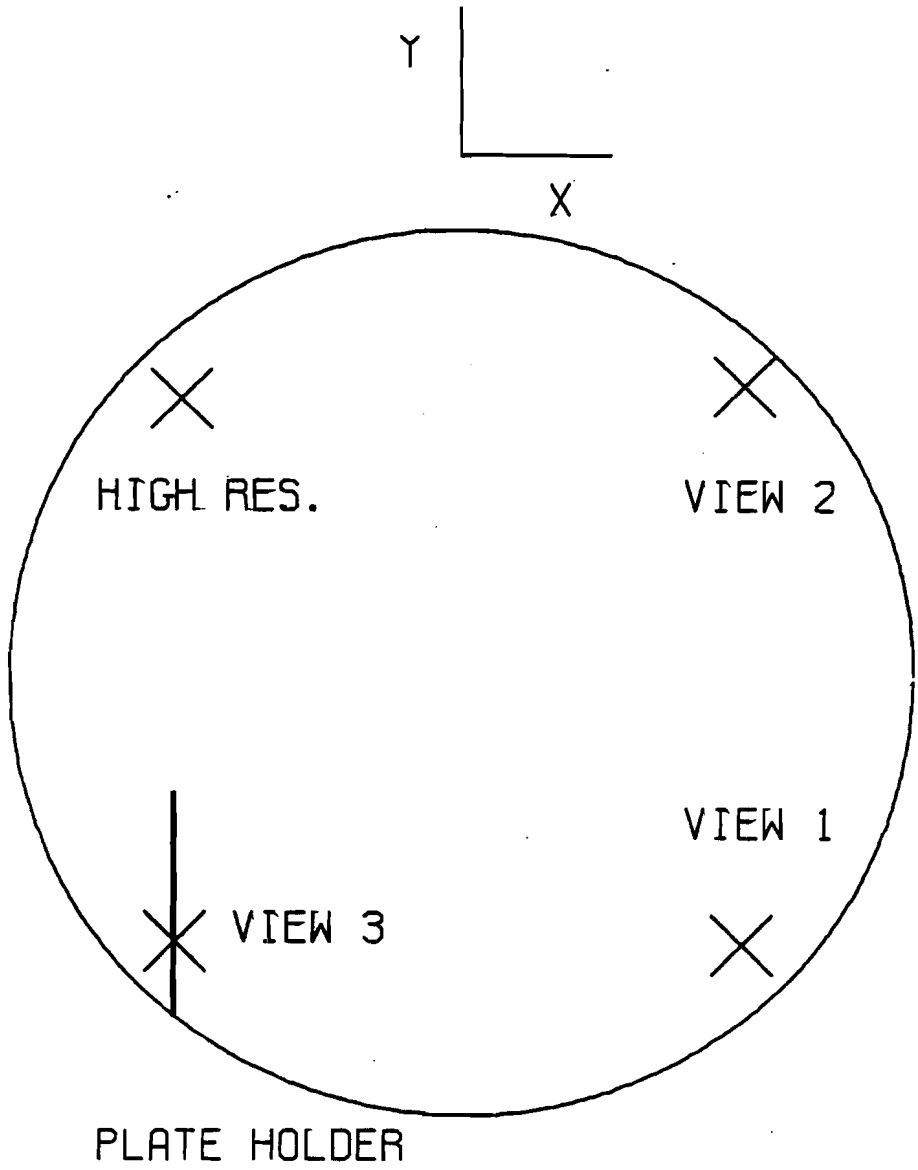

Figure 2-4: 30" bubble chamber and camera ports.

causes a bright region around the plates where all tracks are obscured. For interactions occurring in the plates this obscured region will necessarily include the vertex of the event. To minimize this problem the plate holder was placed directly opposite the upstream camera ports; these cameras viewed the plate holder edge-on so only a narrow region was shadowed. This problem will be discussed further in the data analysis section.

As stated previously, one BC picture was taken in each view per ping. Each picture has a unique frame number printed on the film and written out with the spectrometer data so that film and tape can be synchronized. Within a picture there are one to ten beam tracks, typically six. All of these beams, while resolved in time by the spectrometer are in one BC picture. The only way to make the correspondence between a beam track on film and its associated time slot is by its location in the chamber. More discussion of this will appear in the data analysis section.

As is usually the case, the BC was placed in a magnetic field so that the sign and momentum of charged particles could be determined from their curvature. The 30" BC magnet is a large iron magnet wound with copper which surrounds the BC. This magnet produces a field transverse to the plane of the film and uniform over the visible region of the liquid. The fringe field was measured previously and the E299 values were used. The magnetic field in the central part of the chamber was 20 kgauss. This magnet was usually run at 25 kgauss but Fermilab decided to run at reduced field to save on electricity costs.

2.4) DOWNSTREAM SPECTROMETER

The downstream arm of the Fermilab hybrid spectrometer was designed for four main purposes. These are to track charged particles which leave the BC, to determine the momenta of these particles, to determine the mass of these particles, and to determine the energy of pi-zeros which leave the BC. We used an array of different detectors to accomplish these purposes. These were proportional wire chambers (PWC), drift chambers (DC), the CRISIS detector (see below), and a forward gamma detector (FGD), see figure 2-5. Data from the FGD is not used in this thesis; a complete description of this device can be found in reference 23.

Built for this experiment by MIT, the CRISIS detector is used to Identify Secondaries by Ionization Sampling. CRISIS is a large drift box with two cells. The two cells are one over the other, each cell has high voltage at top and bottom with a sense plane in the middle. There are 192 wires in the sense plane of each cell strung transversely to the beam direction. As a charged particle traverses the drift volume it knocks electrons from the gas which then drift to the sense wires. At each sense wire the time of arrival, the width of the charge pulse, and the total charge are measured. Using the drift velocity of electrons in the gas and the drift time, the distance from the sense plane to the charged particle trajectory can be calculated at each channel (there is an ambiguity as to whether the particle was above or below the sense plane which must be resolved by other means). From the width information we can tell if two charged particles were too close to be resolved in time. The total charge, measured at up to

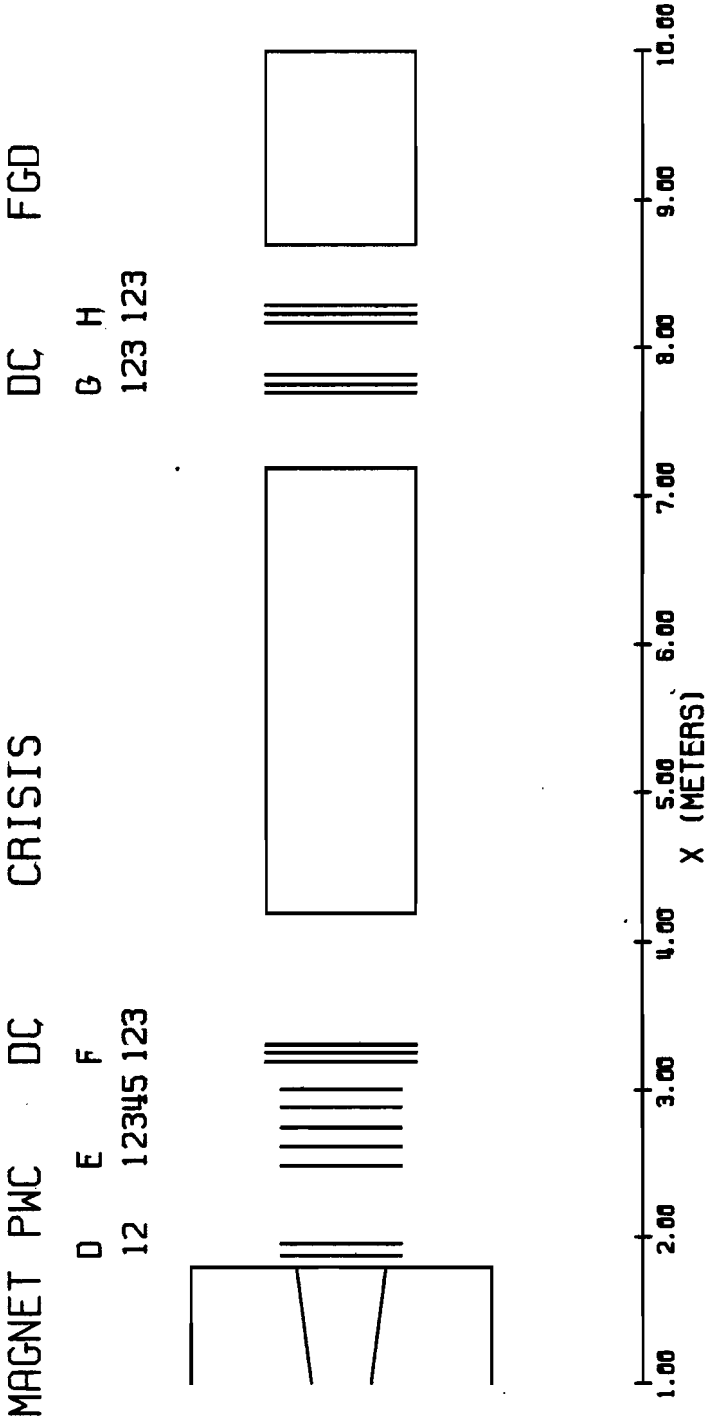

Figure 2-5: Downstream spectrometer.

192 locations along the path, is used to calculate the average ionization of the charged paticle. This ionization can be used, along with the momentum, to identify pions, kaons, and protons. With the drift gas that was used this technique should be effective in the range of momentum from 5 GeV/c to 50 GeV/c. More detail on the CRISIS detector can be found in reference 24.

We had seven downstream PWC planes operational for most of the experiment. Five had a 1.0 X 1.0 meter active area, while the other two were 0.9 X 0.9 meters; these smaller chambers were built to fit in a small space next to the bubble chamber exit window. The two small planes were placed horizontally so that the wires were parallel to the z-direction of coordinate space which is the nonbending direction. These two planes gave a redundant measurement of the y coordinate which is the direction carrying information about the momentum of the secondary. All downstream chambers were placed beyond the range of the magnetic field, so tracks travel in straight lines through the spectrometer. The other five planes were arranged at various angles as shown in figure 2-6. They were also distributed evenly in the available space between the first two planes and the drift chambers. This arrangement is a break with past hybrid bubble chamber experiments in which the wire chamber planes were grouped closely into units called modules. The reasons for the change are connected to both the hardware and the software. To reconstruct data from a PWC module one converts the information of individual wire hits into points where the module was struck by requiring intersections of the hits in the various planes. This works well if the planes are efficient and there are at least three planes per module. In our case

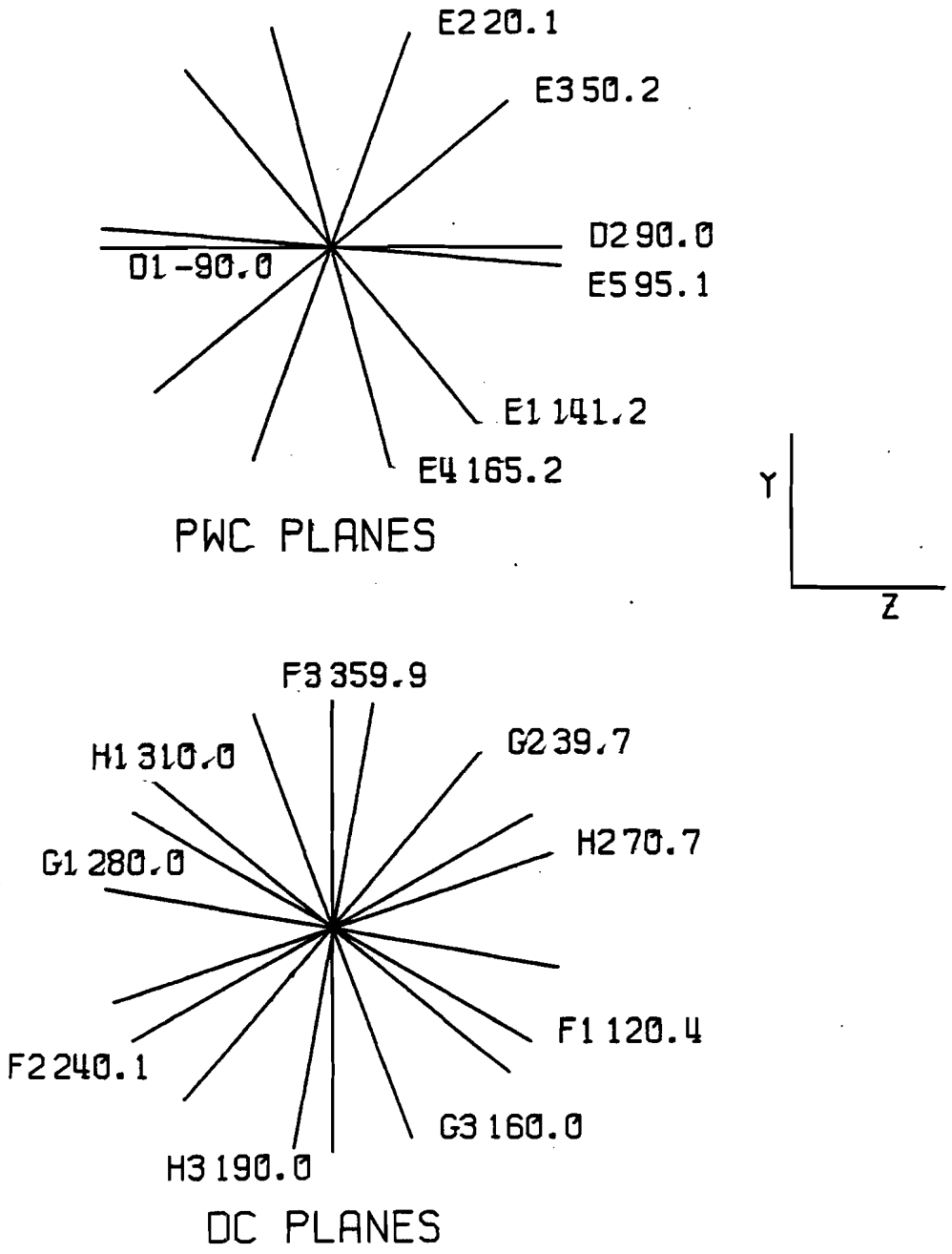

Figure 2-6: Angles of downstream wire chamber planes.

with a total of seven planes we could only make two modules. Also our chambers were not efficient enough that a three plane module would have been useful. This realization was combined with a new idea for reconstructing the downstream tracks that utilized the information from each plane separately and did not rely on the planes being grouped together. On this basis we set up the planes to uniformly cover the available space. This new method of reconstructing the downstream tracks will be discussed in the first appendix of this thesis.

The nine available drift chamber planes were grouped into three modules. Two planes never worked and this left us with seven planes for most of the run. While they were placed into modules the data from the drift chambers were also treated separately for each plane as with the PWC's. In this way we avoided the problem of 'ghost' hits (hits which are artifacts of the left-right ambiguity in drift chambers but cannot be distinguished from the real hit) in our two modules with only two working planes. The left-right ambiguity still exists for each plane and this problem was solved in the software as will be discussed later. The layout of the drift chambers can be seen in figures 2-5 and 2-6. Each drift plane had an active area of 1.2 X 1.2 meters. The drift cells were 5 cm. wide. A complete description of the drift chambers can be found in reference 25.

2.5) COORDINATE SYSTEMS

There are several coordinate systems used for convenience in various devices in the experiment (see ref 26). All of these systems

can be related to the basic spectrometer system (BSS). In the BSS the direction of the x axis is defined by the upstream PWC's. Four upstream chambers are chosen, a pair in the first and in the last chamber. The x axis passes through the point where the central wires cross in each of these pairs. The x axis is roughly parallel to the average beam direction because the upstream chambers are placed so the beam goes through their centers. Zero for this axis is near the center of the BC and the positive direction is downstream. The z axis is horizontal with its origin at the BC center and positive towards the cameras. To make a right handed coordinate system the y axis is vertical (roughly since the x axis is not exactly horizontal) and is positive downward. Beam tracks in this experiment go through the lower half of the BC so the origin is below the center of the BC.

Historically BC reconstruction has been done in a coordinate system which is a little different than the BSS described above. Note that the BSS will move in space if the upstream chambers are moved. However, BC measurements are made relative to fiducial marks on the BC windows which do not move unless the chamber is disassembled. A bubble chamber system (BCS) defined by the BC fiducials is used for these measurements. The directions of the axes generally follow those in the BSS but there are small angles between the two systems. In addition the origins of the axes are different. The origin is on the surface of the BC window closest to the cameras and near the center of this circular window. In order to transform between the BCS and BSS systems it is neccessary to calculate a translation vector and a 3 X 3 rotation matrix.

CRISIS also has its own coordinate system to make internal calculations easier. The CRISIS system has its origin at the center of CRISIS. The x axis is roughly in the beam direction and parallel to the central high voltage plane. Z is parallel to the sense wires and points towards the cameras as the other z axes do. For a right handed system y points downward and is perpendicular to the central high voltage plane. Since CRISIS only gives information on the x and y position of a particle the z coordinate is unimportant. To transfer from the CRISIS system to the BSS only x and y translations, and a rotation about the z axis are used (the z translation and the other rotations are set to zero).

2.6) ONLINE DATA HANDLING

Between each ping, which represents one bubble chamber expansion and up to ten timeslots, data was extracted from the various devices and stored on magnetic tape. During the gap between accelerator cycles calibration data from the FGD and CRISIS were logged on the same tape. This was all done using the program MULTI which read the data that was set up in CAMAC modules. For a detailed description of MULTI as modified for this experiment see reference 27.

The online tapes, called MULTI tapes, are difficult to use directly. Computer crashes result in data breaks and bubble chamber failures can mean long periods with no useful data. The MULTI format is cumbersome, and the data blocks, which were set up for speed of reading, are not in a convenient form. A program was written to operate on these MULTI tapes and to produce a tape with only the

useful information in a more easily accessed format. This program was called PURE (Programs United to Reduce Errors). Each time a roll was completed, the MULTI tape, or tapes, were driven from the experimental portakamp to the Fermilab highrise building. Here the tape was registered in the library and a copy was made. The program PURE was run on the copy to produce a PFC tape for the roll. The PFC format is detailed in reference 28. The completed PFC tapes typically contain three rolls of data per 6250 bpi tape. A complete set of PFC tapes for the experiment consists of 117 tapes (from over 300 MULTI tapes).

A program called CHECK was written to check the PFC formatted data. This program produced plots for each of the downstream devices which could be used to monitor their operation. Problems such as oscillating wires, or dead sections would show up in these plots. CHECK was run for every roll at the beginning of the run and for every few rolls later when most startup problems had been fixed. The CHECK output was brought to experimenters on shift at the portakamp so device experts could check their detector's output.

2.7) DATA-TAKING

E565/570 had two running periods 2/6/82 to 3/25/82 and 5/6/82 to 6/1/82. During this time we logged 787,000 pictures with positive beam and 218,000 pictures with negative beam. Most of the data used in this thesis came from the first part of the second run, during which the downstream spectrometer was working efficiently. All of these data were from the positive beam sample. The analysis of these data will be described in the next few sections.

3) EVENT PROCESSING

Detailed descriptions of data processing in hybrid bubble chamber experiments may be found in several places, (ref. 29,30). This description will emphasize the differences between the current analysis and the standard procedures. These differences may be separated into two types. There are some procedures new to this experiment which are used for all events. Also, there are special techniques specifically for handling plate events. Figures 3-1 and 3-2 show schematically the event processing chains for H_2 events and plate events respectively. Table 3-1 highlights in brief the differences between these two chains.

While this thesis deals with the physics of interactions in the metal plates, Rutgers also had a major responsibility for software in the experiment. In what follows there will be detailed descriptions of the program TRIFID and of the PIG and SOW subroutines in GEOHYB. These routines were used for, but were not special to, plate events. They were new to this experiment and represent a considerable change from older methods. As they were originated at Rutgers, and I spent much time working on them they will be documented here.

All of the programs used to process data for this expeiment were written using the HYDRA/PATCHY system from CERN. HYDRA (ref. 31) is a collection of subroutines for organizing data inside a FORTRAN program. It is especially useful for event processing because the data is organized into a tree structure from which branches can be discarded when they are no longer needed. This conserves space in the program. When an event is finished the processed tree is written out

HYDROGEN EVENT PROCESSING

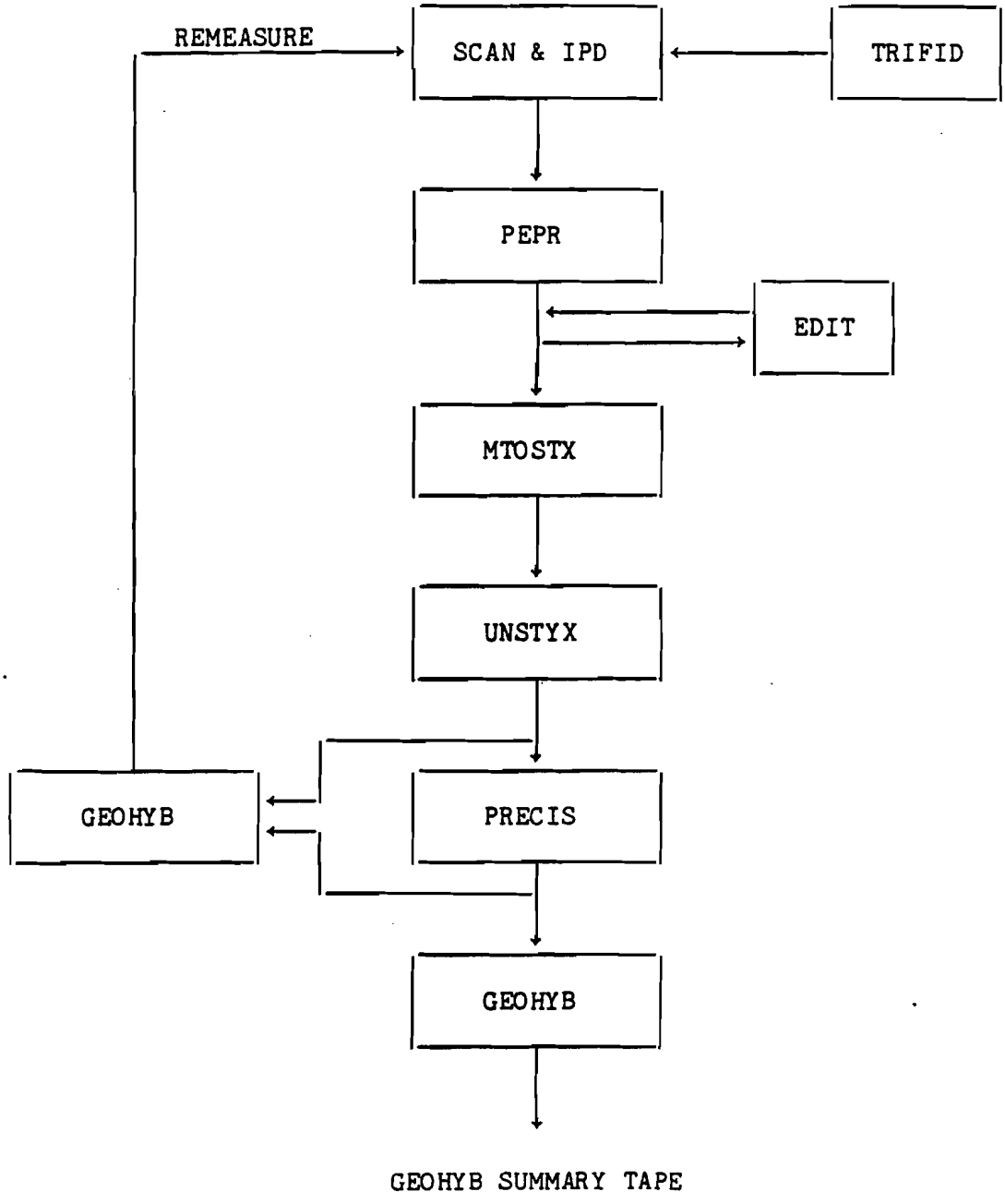

Figure 3-1: Processing chain for hydrogen events.

PLATE EVENT PROCESSING

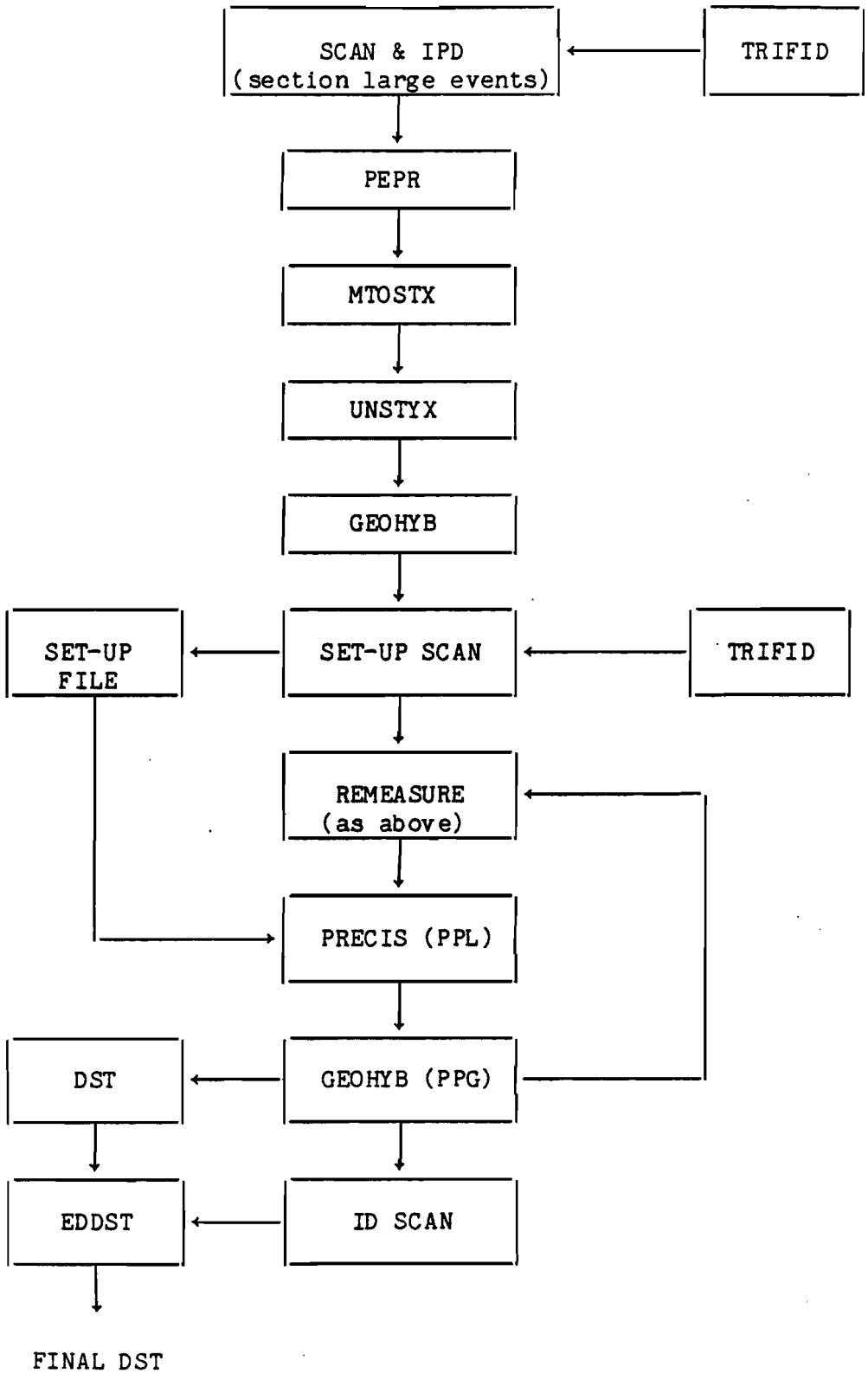

Figure 3-2: Processing chain for plate events.

1) Large plate events are IPD'd in sections (see sect. 3.2).

2) Set-up scan identifies beam type and plate number (see sect. 3.3).

3) Plate version of PRECIS is used (see sect. 3.3).

4) Plate version of GEOHYB is used (see sect. 3.4).

5) ID scan identifies mass of slow secondaries and picks up lost tracks (see sect. 3.5).

6) ID scan information is combined with GEOHYB output in DST format (see sect. 3.5).

Table 3-1: Main additions to plate processing chain.

and a new input tree is read in. HYDRA has many other useful features which facilitate communication between computers of different brands and enable error tracing in bad events. PATCHY (ref.32) is a system of programs which control software development in an environment where many different people are working on and using the software. Basic program versions are centrally stored in files called PAMs. These versions can be modified locally by using the PAM file and a CRA file which contains the modifications. Different users each have their own CRA files. If local corrections or additions become widely useful an updated PAM is created incorporating the changes. The HYDRA/PATCHY system has been used by the Fermilab hybrid spectrometer consortium since the group was formed to run E154. Francis Bruyant of CERN, an original consortium member, first introduced the system and was responsible for much of the original software.

3.1) TRIFID

In previous experiments much time was spent measuring events which later had to be rejected because the beam type was unknown (π, K, p). The $\check{C}$ information for each beam is encoded with the PWC data for each time slot; and so to identify the beam the linkup between film and electronics tape must be made. This linkup was done in the program PRECIS which was run after the events had been measured (see figure 3-1). In PRECIS three things could make the beam type indeterminant. First, the film beam might not match any time slot on

the tape. This can be due to an incoming track which misses the scintillator telescope, or a beam which is badly fit in the PWC's and so misses its image in the BC. Second, more than one time slot might match the film beam. This happens when two or more beams are very close in space. Third, the linkup might be unique but the Cerenkov detectors failed to identify the beam type. None of these problems is recoverable, so these events have to be discarded. In this experiment each of these effects occurs in approximately 10% of events.

To avoid spending time measuring these bad events (30% of sample) we developed a program to pick these events out at the scan level, TRIFID. While developing TRIFID to solve the above problems we realized that it could also be used to "trigger" certain kinds of events. That is we can measure or skip certain events to enhance the physics in our final sample. Event types with lower statistics, such as plate events and K-beam events are all measured; while only a fraction of the more common events are measured. The name TRIFID, short for TRIggered FIDucial volume, comes from this second function.

TRIFID is run on the PFC tape which contains the electronics information for each roll. For every timeslot of every frame TRIFID prints the location of the beam along with other information (for each roll the listing is about 15000 lines). The aim is for the scanner to correlate beams on the scan table with those on the TRIFID listing. From the other information on the listing the scanner can decide whether to measure, to reject, or to ignore the event.

For every frame for which there is electronics information TRIFID does the following. First the beam for a timeslot is

reconstructed in the upstream PWC's using the subroutine CHUP (CHi-squared fit for UPstream). This subroutine does a chi-squared fit to a straight line through the hits in the upstream PWC chambers. Typically 2% of the timeslots do not have a good fit here; these are discarded.

The fit beam is then swum through the magnetic field into the BC. Once inside, the beam is projected onto the film plane at two locations in each view. That is, knowing the predicted location of the beam in space we calculate a position on the film where the image of that beam should appear. This prediction is made at the same X position as a known fiducial, and the distance across to that fiducial is calculated. The distance from the beam to the fiducial is then scaled up to match the magnification of an individual scan table. For a given scan table the distance in cm. between two fiducials (numbers 16 and 22) is stored in a program variable (DFVWS) for each view. TRIFID is told which scan table the list is for and so can calculate the scale factor. The result, now in cm. on the table, is printed out for each view and the scanner can find the beam by measuring across from the reference fiducial. As long as the magnification does not change on the scan table these predictions are accurate to 2 mm on a life size image.

TRIFID makes a prediction as to whether the beam has interacted as it passed through the system. After swimming the beam through the chamber, as described above, it is continued out into the downstream spectrometer. At every downstream wire chamber plane a comparison is made between the predicted location and the hits in that plane. If the beam has not interacted somewhere in the system then there should

be a hit close to the prediction in each plane, except for misses due to inefficiency. Many hits in the plane or no hit at the expected location is an indication that an interaction has taken place. For each plane the perpendicular distance from the beam to the nearest hit wire is calculated. If this distance is too large, or if there are too many hits in the plane, or no hits, the plane is discarded. An average RMS is calculated from all contributing planes. If this RMS is too big, indicating that the beam changed direction, then the beam is flagged as interacting. Also, if too many planes are discarded the beam is flagged as interacting.

This interaction trigger worked well. Occasionally a two or four prong event with a fast forward particle will mimic a through beam. It is hard to tell how often through beams were flagged as interacting since we cannot see interactions beyond the visible liquid of the chamber. The trigger, while accurate, was not very useful in the scanning. It was used to corroborate that the beam associated with an interaction actually did interact.

When all the timeslots for a frame have been processed they are printed out in order from left to right across the frame. This is as a convenience to the scanner. Some sample TRIFID output is shown in figure 3-3. For each new frame the frame and ping number are printed. Beam tracks which are close in space cause a problem in identifying which beam to associate with an event. The predictions for the beams in a frame are compared. Those which are too close in one or two views are flagged CLS!, those which are too close in space (all three views) are flagged CL33. Interacting beams picked up by the trigger are flagged YES!. Beams which should be measured in the whole

TRIFID PREDICTIONS FOR ROLL 2020. 27-JULY-82 VERSION. RJP/RU **** PRODUCTION VERSION II 27-AUG-82 FIDS 22-:16.19

FRAME	PG	TS	INT?	BIG?	CLS?	BEAM	PLATE	NG	V4	V1	V2	HIGH RES.	YZ OF VERTEX	CHI2/P/D
708717	1	4				??	3-AU		11.80(12.05/3)	11.73(11.92/3)	17.24(17.41/3)	1.61(1.64/0)	6.83 -19.56	1.3/3/6
		3	YES!	BIG!		K	23		13.22(13.46/6)	13.14(13.33/6)	18.69(18.87/6)	1.77(1.80/0)	5.68 -19.38	0.01/5/0
		6	YES!		CL33	PR	2-AG		14.17(14.43/5)	14.09(14.29/5)	19.47(19.64/5)	1.86(1.89/0)	5.00 -19.91	0.00/0/0
		5	YES!		CL33	PI	2-AG		14.39(14.64/6)	14.31(14.50/6)	19.61(19.78/6)	1.88(1.91/0)	4.86 -20.13	0.50/5/0
		2				PI	12		15.09(15.36/1)	15.01(15.21/1)	20.50(20.67/1)	1.98(2.01/0)	4.22 -19.56	0.60/6/3
		1				PI	1-AG		15.62(15.88/2)	15.53(15.73/2)	21.00(21.18/2)	2.03(2.07/0)	3.81 -19.60	0.68/6/4
708718	2	1				PI	4-AU		9.91(10.14/2)	9.85(10.04/2)	15.36(15.52/2)	1.39(1.42/0)	8.33 -19.56	0.84/4/4
		2	YES!			PR	2-AG		13.83(14.08/3)	13.75(13.94/3)	19.26(19.44/3)	1.84(1.87/0)	5.21 -19.50	0.95/4/2
		3				PI	1-AG		15.94(16.20/2)	15.85(16.05/2)	21.27(21.45/2)	2.07(2.10/0)	3.57 -19.74	0.77/6/4
708719	4	3	YES!	BIG!		K	4-AU		10.01(10.25/4)	9.95(10.14/4)	15.58(15.74/4)	1.42(1.45/0)	8.19 -19.21	0.00/0/0
		4				??	3-AU		11.89(12.13/5)	11.81(12.01/5)	17.31(17.48/5)	1.62(1.64/0)	6.77 -19.58	0.82/6/5
		5	YES!			PI	2-AG		13.62(13.88/1)	13.54(13.74/1)	18.77(18.94/1)	1.78(1.81/0)	5.52 -20.35	0.00/0/0
		1				PR	2-AG		14.33(14.58/5)	14.25(14.44/5)	19.68(19.85/5)	1.88(1.92/0)	4.85 -19.74	0.28/6/4
		2	YES!			PR	12		15.41(15.67/1)	15.32(15.52/1)	20.78(20.96/1)	2.01(2.04/0)	3.98 -19.66	0.26/1/0
708720N	5	3		BIG!		K	56		7.64(7.86/1)	7.59(7.77/1)	13.03(13.19/1)	1.13(1.16/0)	10.18 -19.80	0.33/5/3
		1	YES!			??	12		15.42(15.68/2)	15.33(15.53/2)	20.75(20.93/2)	2.01(2.04/0)	3.99 -19.77	1.16/2/0
708721	6	6	YES!			PI	3-AU		11.03(11.27/1)	10.96(11.16/1)	16.61(16.77/1)	1.54(1.56/0)	7.37 -19.16	0.52/3/0
		1				PI	3-AU		11.43(11.67/6)	11.36(11.55/6)	16.90(17.07/6)	1.57(1.60/0)	7.11 -19.44	0.77/5/3
		3			CL33	PI	3-AU		12.75(13.00/7)	12.68(12.87/7)	18.08(18.25/7)	1.70(1.73/0)	6.12 -19.85	1.18/3/5
		7	YES!		CL33	PI	3-AU		12.76(13.00/3)	12.68(12.87/3)	18.09(18.26/3)	1.70(1.73/0)	6.12 -19.82	0.00/0/0
		5				PI	23		13.03(13.27/7)	12.95(13.14/7)	18.37(18.54/7)	1.74(1.77/0)	5.89 -19.79	0.31/4/5
		2				PI	91		17.05(17.32/4)	16.96(17.16/4)	22.33(22.50/4)	2.18(2.22/0)	2.71 -19.91	0.34/7/4
		4	YES!			PR	91		18.19(18.47/2)	18.09(18.29/2)	23.44(23.62/2)	2.31(2.34/0)	1.81 -19.94	0.51/6/0
708722	1	1	YES!			PI	4-AU		9.60(9.83/2)	9.54(9.73/2)	15.13(15.29/2)	1.37(1.40/0)	8.54 -19.33	0.00/0/0
		2				PR	34		10.70(10.93/1)	10.63(10.82/1)	16.21(16.37/1)	1.49(1.52/0)	7.67 -19.35	0.66/6/6
		3				PR	1-AG		15.88(16.14/2)	15.79(15.99/2)	21.16(21.34/2)	2.05(2.08/0)	3.64 -19.89	0.69/6/1
708723N	2	3				PR	56		7.55(7.76/2)	7.49(7.67/2)	13.01(13.17/2)	1.13(1.15/0)	10.21 -19.58	0.58/4/3
		2			CLS!	??	23		13.00(13.25/1)	12.92(13.12/1)	18.38(18.56/1)	1.74(1.77/0)	5.90 -19.67	1.11/3/4
		1	YES!		CLS!	??	2-AG		13.62(13.87/2)	13.54(13.73/2)	18.56(18.73/2)	1.76(1.79/0)	5.62 -20.99	0.00/0/0
708724N	3	2				PI	6-MG		7.03(7.25/6)	6.98(7.17/6)	12.45(12.61/6)	1.06(1.09/0)	10.65 -19.73	0.84/5/5
		6				PR	5-MG		8.65(8.87/2)	8.59(8.77/2)	14.10(14.26/2)	1.25(1.28/0)	9.34 -19.57	0.33/4/3
		4			CL33	??	3-AU		11.86(12.11/3)	11.79(11.98/3)	17.39(17.56/3)	1.62(1.65/0)	6.73 -19.27	0.88/4/5
		3			CL33	PR	3-AU		12.07(12.31/4)	12.00(12.19/4)	17.42(17.59/4)	1.63(1.66/0)	6.66 -19.81	1.25/3/6
		1				PI	2-AG		13.58(13.83/5)	13.50(13.70/5)	18.85(19.02/5)	1.79(1.82/0)	5.49 -20.01	0.20/5/6
		5				PI	2-AG		14.27(14.53/1)	14.19(14.39/1)	19.65(19.82/1)	1.88(1.91/0)	4.88 -19.65	0.97/6/6
708725N	4	2				PI	5-MG		8.54(8.76/3)	8.48(8.66/3)	13.94(14.10/3)	1.23(1.26/0)	9.45 -19.75	0.48/6/4
		3				PR	23		13.09(13.32/1)	13.00(13.19/1)	18.39(18.56/1)	1.74(1.77/0)	5.87 -19.87	0.87/4/6
		1				??	2-AG		14.53(14.79/3)	14.44(14.64/3)	20.14(20.32/3)	1.94(1.97/0)	4.57 -18.93	0.13/5/5
708726N	5	1				PR	23		13.30(13.55/0)	13.22(13.42/0)	18.62(18.80/0)	1.76(1.80/0)	5.69 -19.85	0.89/5/6

Figure 3-3: Sample TRIFID output.

fiducial region are flagged BIG!. This flag is currently set only for those beams identified as kaons. After these beam flags the beam type as determined from the $\check{c}$ code is printed, ?? means a $\check{c}$ failure. Next the plate number and type is printed. This information is calculated by comparing the beam prediction with the plate locations. This feature is accurate except near the edges of the plates; two digits in this column (ie. 12) indicate that the beam is between two plates. The rest of the information printed out for each timeslot is its predicted location relative to fiducial numbers 22 and 19, in each view.

TRIFID output is given to the scanner for the roll and scan table being used. When an event is found the scanner measures the distance from the beam across to fiducial 22. This distance is checked versus the TRIFID predictions to match the beam. If the beam is not listed on the TRIFID output, the event is ignored. Otherwise the scanner checks the other information for that beam to see if the event should be IPD'd (see section 3.2). If the Cerenkov code is no good (??) or if there is another beam too close (CL33), the event is recorded but not IPD'd. These events are recorded so that we can check for biases in the event rejection.

Not all of the remaining events were IPD'd. As stated earlier we wanted to enhance the sample of certain kinds of events. Events with kaon beams (flagged BIG!) and two pronged events were all IPD'd. Pion and proton beam events were IPD'd only in a reduced volume near the front of the chamber, about a third of the total. The rest of these events were just recorded so that we could go back and measure them later if we wanted. This procedure insured the maximum number of

kaon beam and two prong events while yielding a sufficient number of pion and proton beam events.

TRIFID enables us to solve several problems. We do not measure many events (30%) which we would have to discard later. Also we can maximize the physics content of our work by selecting which events to measure.

3.2) MEASURING

Once an event has passed the criteria in TRIFID it must be measured. Precise measurements of each track in each view are needed so that later programs can reconstruct the three momentum of each secondary particle. The precision measurements are made by a device called PEPR. PEPR runs semi-automatically; an operator helps when the device gets confused but otherwise it does all measurements by itself. As input PEPR requires rough locations of the vertex and tracks in an event. These locations or pointers are provided by a process called IPD'ing (Image Plane Digitization). The IPD'ing is usually done at the same time and on the same machine as the scanning. The PEPR output contains, for each view, fiducial measurements, vertex points, and points along each track.

Plate events present several problems which require special handling here. The most important point is that the charged topology for plate events can be very large; the largest event that we have counted has 97 charged secondaries. Several events per roll have more than 30 charged tracks. This can be compared to the situation in hydrogen events where in E299 out of 43,000 events four had 24 prongs,

two had 26 prongs, and none were larger. All of our programs had been designed to run on these smaller events. We originally tried to measure some events up to about 30 prongs in the old way and we found that the programs could not handle them. This was not simply a problem of increasing the dimensions in the programs; the time used by the algorithms that match tracks increased geometrically with the number of tracks. Either these algorithms had to be rewritten or some different method of measuring large events had to be found. At Rutgers we developed a new method for splitting these events into manageable sections at the IPD level, and then recombining them after the program chain. Other groups in our consortium are working at rewriting the software to handle these events without special measuring; this effort has not yet been successful.

The problem with large events is in the track matching, that is in deciding which track image from each view to combine to make a real track in space. In some bubble chamber experiments this matching is done on the scan table by the operator. For larger events this is a very time consuming task. Our current software can handle this problem up to about 20 tracks; so for hydrogen events and for many plate events the IPD'er simply marks each track in order without worrying about which track matches in the other views. Our new procedure is a combination of these two extremes. Large events are measured in sections. Each section contains a set of up to twelve tracks with these same tracks measured in each view. In this way it is neccessary to match only sets of tracks, not each track separately. In practice this distinction makes the task of the IPD'er doable. Each section is then treated as a separate event through the rest of

the program chain. Special handling is required so that the sections can be recombined for physics analysis, but since each section contains fewer than thirteen tracks (or so) no other changes in the software are needed.

As an example, figures 3-4, 3-5, and 3-6 show the three views of a typical 33 prong event split into three sections. The IPD'er takes advantage of the geometry of the individual event. Most tracks are easy to place, although special care must be taken where sections overlap and with tracks which make a large angle to the film plane (these tracks can move from view to view). The section number is placed in the scanner comment word in the header, 57 denotes a section with neutral activity. Otherwise the section number starts with 51 and increases till all tracks are IPD'd. Events with up to 97 charged tracks have been processed in this way.

For each sectioned event a record is kept of how it was measured. In view 3, usually the clearest view, a drawing is made of each section showing which tracks were measured in that section. These drawings are kept in notebooks arranged by roll. In this way it is possible to recreate the sequence of measured tracks in a section. This is useful if a section has to be remeasured and also during the ID scan which will be discussed later.

Another difficulty with plate events which is not found in hydrogen events is that the plates and plate holder cast a shadow on the film that obscures the vertex region. This is a problem in several ways. First the vertex position is not clear. At the IPD level the operator makes a best guess of the vertex position by

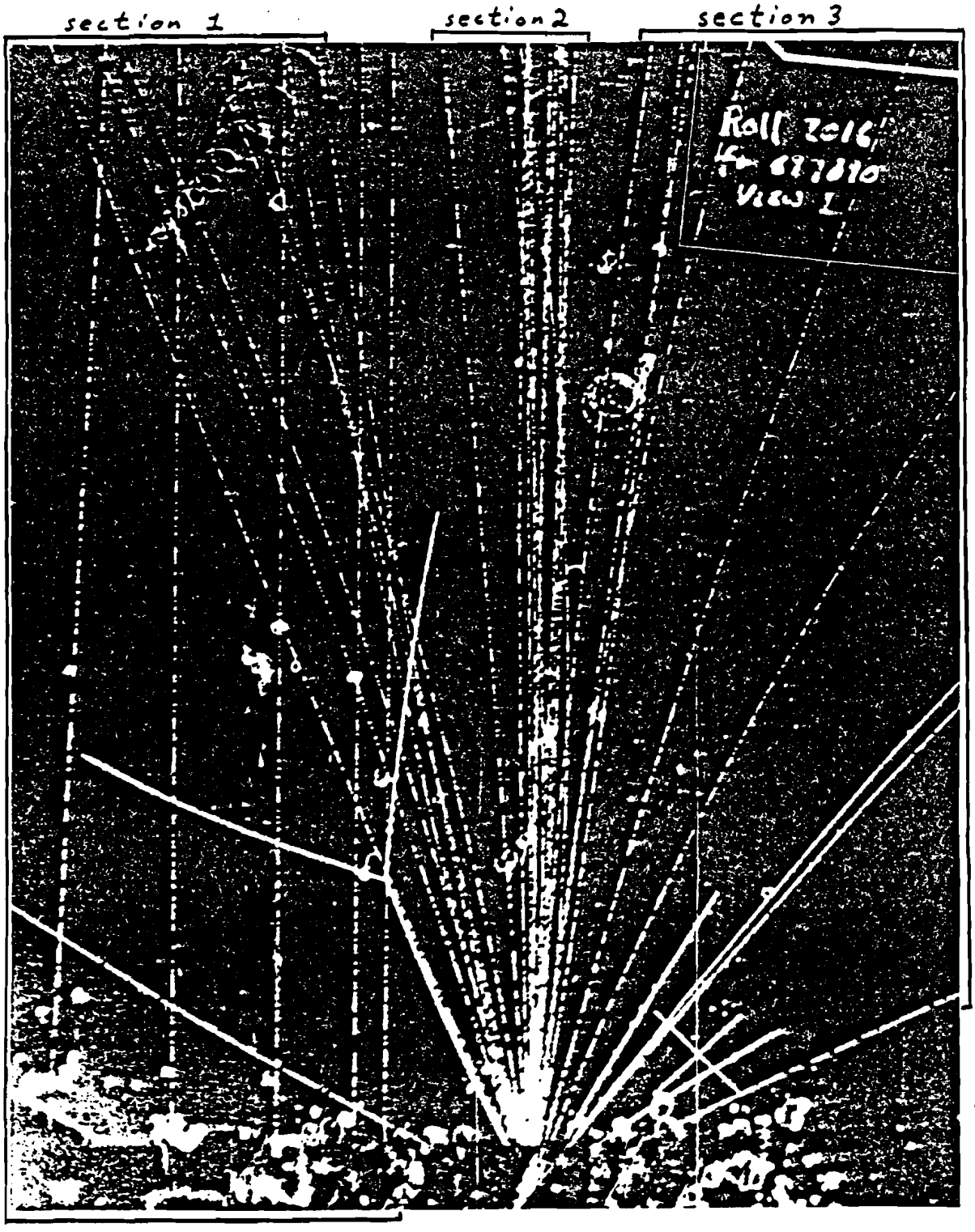

Figure 3-4: Sectioning example, view 1.

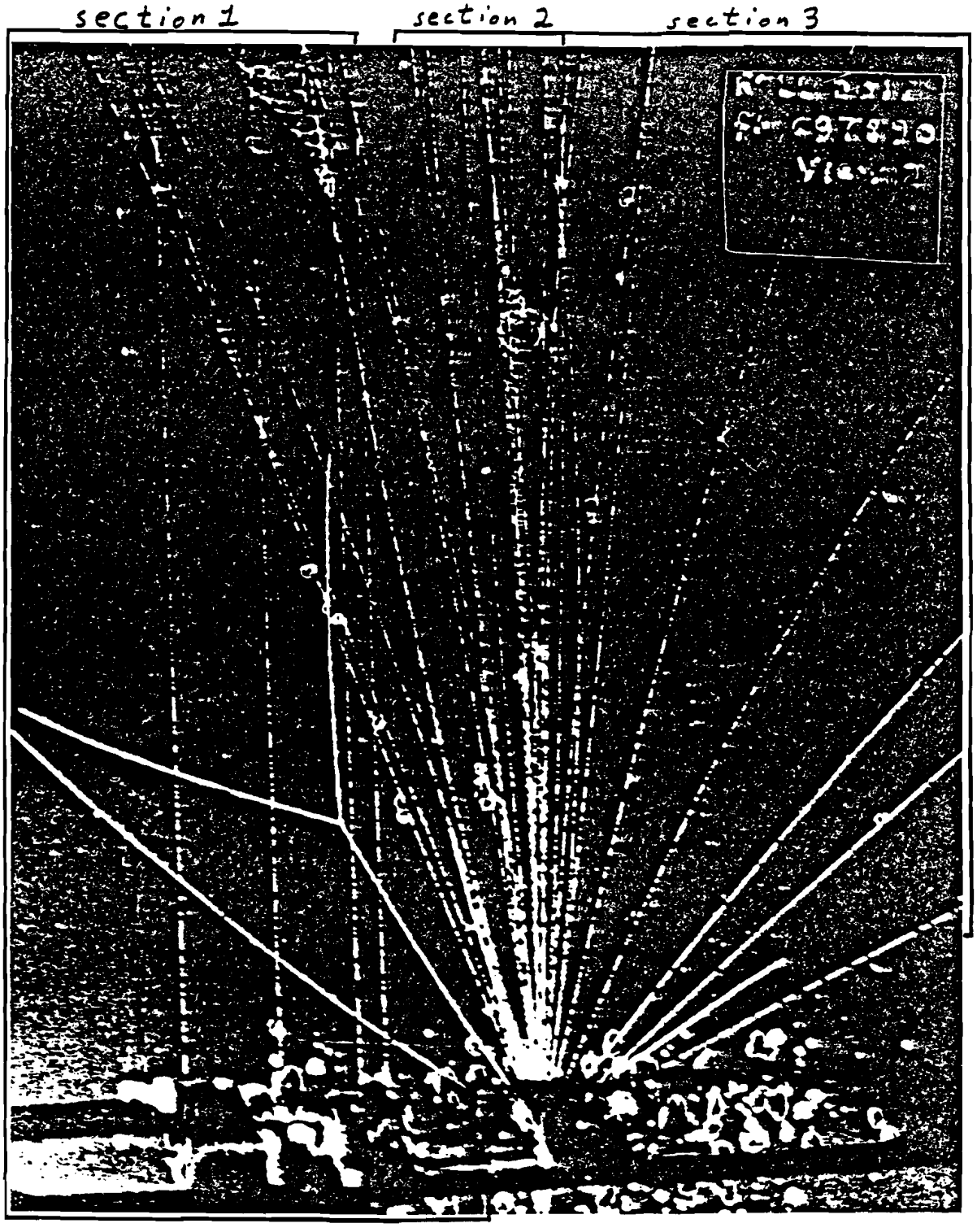

Figure 3-5: Sectioning example, view 2.

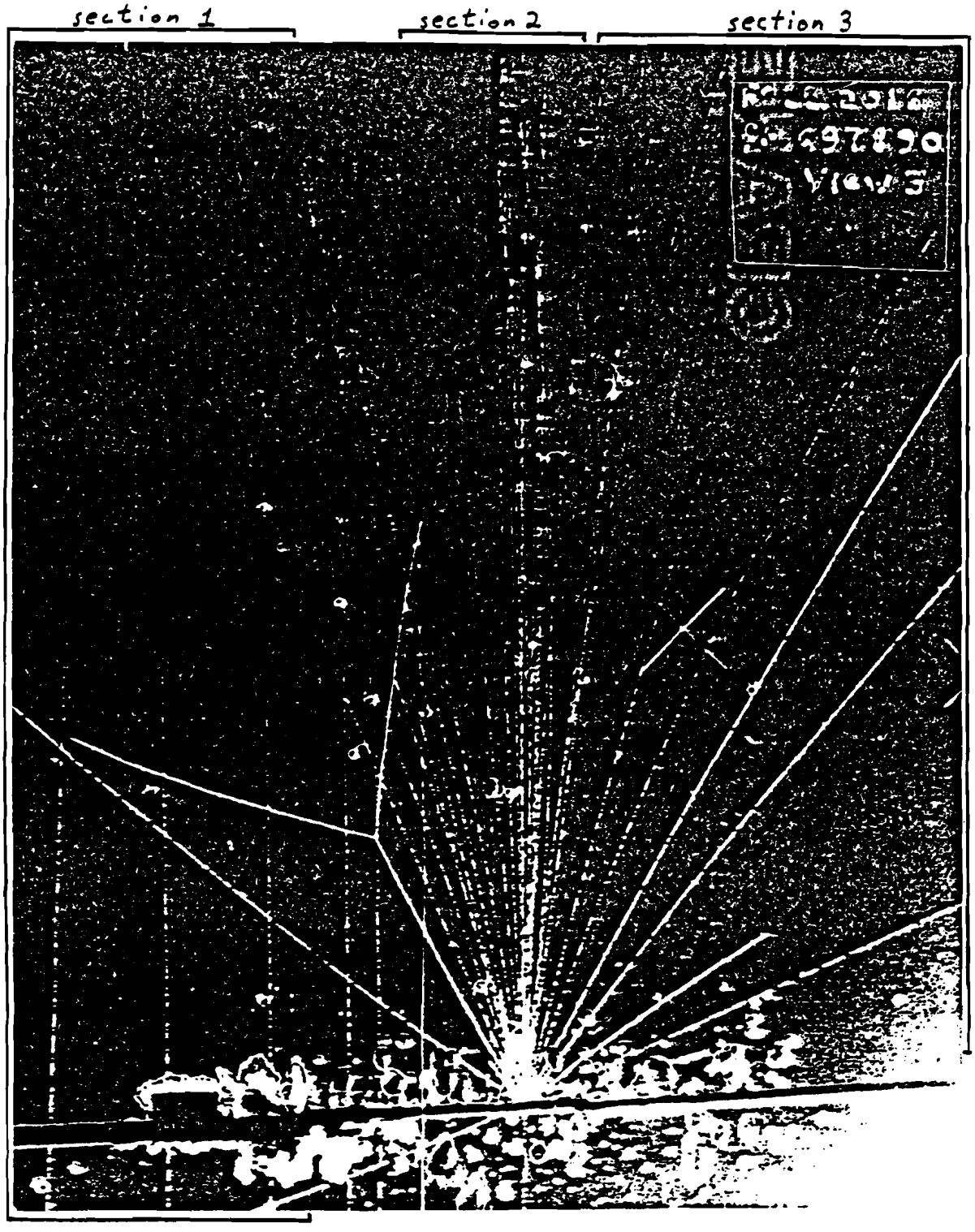

Figure 3-6: Sectioning example, view 3.

extrapolating wide angle tracks from their visible region into the plate shadow. This vertex problem will be discussed later under PRECIS. A second problem caused by the shadow is that short tracks which travel only a few cm. before stopping may be totally covered in some views. In this case the IPD'er is instructed to count all tracks even if they are seen only in one view. These tracks cannot be reconstructed but they are counted during the ID scan (ID scan will be discussed in section 3.5). Third, close secondary interactions and short neutral decays are confused as their vertices may be obscured. For this problem we relax the usual rule that a neutral vertex must be visible in all views. Also, the scanner is encouraged to look very carefully for any clue as to the nature of the obscured interaction. In some cases events must be rejected because it is not possible to figure out what is occuring behind the shadow. None of these problems can be completely remedied, but we have tried to follow procedures that will minimize their effects on the physics.

After the measuring phase, the data is run through several small programs which combine the three PEPR views and reformat the results for input to the large programs that follow, PRECIS and GEOHYB (see figure 3-2). At this point the data consist of measurements from the three views of the film. Some events are split into sections and others are not.

3.3) PRECIS

The next major step in the processing chain is to combine the measurements from the film with the electronics data (see figure 3-2). Although the electronics information was used in TRIFID to help select events, those events were not linked to their associated electronics data (called the timeslot) during the scan. PRECIS is the program which accomplishes this task. The basic ideas of PRECIS have not changed from the earliest hybrid bubble chamber experiments; it still uses the same method for linking bubble chamber measurements to the timeslot. Because our spectrometer is different than in previous experiments, PRECIS performs additional tasks compared to previous versions (for a description of PRECIS for E299 see ref. 29).

In PRECIS the production (main) vertex is reconstructed. That is, a point in space is found from the measured points in the three views. This vertex reconstruction will be discussed later. As in TRIFID, CHUP is used to reconstruct beam tracks from the upstream PWC timeslots. These beams are extended into the chamber and the perpendicular distance from the vertex is calculated at the same X as that of the vertex. If the beam is within tolerance in both dimensions (3 mm in y, 4 mm in z) then the timeslot is flagged as accepted. After all timeslots are tried, any event with more than one or with no accepted timeslot is discarded. Because TRIFID has been used to screen the events the number discarded here is small, about 1%.

After this point our PRECIS differs from the old version. Once a unique timeslot has been accepted the electronics data must be

reformatted into HYDRA banks for transmission and use in GEOHYB. The subroutine UNPURE reads events off the PFC tape and sets up recorded element (RE) banks for the PWC and DC data, and CRISIS data (CD) banks for the CRISIS data (see ref. 33 for a description of the bank formats). At this point in the old PRECIS the processors SEM and CEM were called to produce element multiplets for use in GEOHYB. The current GEOHYB, as will be discussed later, does not use element multiplets so these processors are not needed. In the space left by their absence we have inserted the CRISIS processor.

The CRISIS processor (written by Tom Stoughton and Seog Oh from MIT) takes the raw CRISIS data and forms it into planes which represent charged particles traversing CRISIS. The location and average ionization of each plane is calculated and stored in CRISIS plane (CP) banks while the raw data which make up each plane are stored in an associated extension bank (CPX). Calibration of the raw CRISIS charges is done in the subroutine CHARGE which requires extensive titles (see ref. 34). There is a large title file which contains the relative gain of each of the 9240 capacitors (24 in each of 385 cells). Further, there is a cell by cell gain factor which is in the same file as the rest of the PRECIS titles. Also, there is an overall gain factor which is time dependent. This last factor is read from a separate file (IN1.DAT) which contains gain data as a function of frame number and the drift velocity which also varies with time. The file is generated by a stand alone program CRISP which must be run on each roll of PFC data. A switch (MCRCAL) in the PRECIS titles skips the charge calibration if desired. Another switch (MCRRAW)

allows the output of raw CD banks so that the calibration can be checked at a later time.

PRECIS output is used as input to GEOHYB, the program that reconstructs the charged tracks in an event. It is also possible to skip PRECIS and run UNSTYX (a reformatting program) output directly into GEOHYB (see figure 3-2). In this case no spectrometer information is available, but GEOHYB can reconstruct the event just using the bubble chamber measurements. The errors on fast tracks reconstructed by this method are large and the matching is sometimes wrong. However it is still useful to run this way in order to check for gross problems in an event that would require remeasurement.

The total number of plate events in our sample is small, about 50 events per roll of which typically 25 are IPD'd. Because of these small numbers it is possible to handle each event in detail without expending too much time.

At this point in the processing chain a new step was added for plate events (see figure 3-2). This is called the set-up scan. The goals of this scan are to:

- check all events found by the scanners and make sure that all are properly designated as plate or hydrogen events

- recheck all plate events to make sure plate number, topology, reject code, etc. are correct

- associate the timeslot for each event using the TRIFID output and so remove this task from PRECIS

- use bare bubble chamber GEOHYB output run from UNSTYX to flag bad events to be remeasured.

It is envisioned that this set-up scan should be done by a physicist. For data in this thesis all set-up scans were done by me. The

advantages gained by this scan will be clearer if we examine each goal.

To insure a complete sample of plate events all events found by the scanner are reexamined. An event is considered to be a plate event if its vertex is within the plate in all three views. In view three the plate holder is viewed edge on; the vertex must be obscured behind the holder in this view. In the other views events which occur between or beyond the plates can be detected if their vertex is visible. Boiling of the liquid hydrogen around the plates obscures their edges in most frames, and this problem is worst around the magnesium plates. When the vertex is in this boiling region the visible part of the tracks are extrapolated back to estimate the vertex position. After this scan the plate file should contain all events consistent with being in the plates and only these events.

As each plate event is found it is checked to make sure that the scanner handled it properly. The person doing the set-up scan has the TRIFID output and the notebook with the section drawings. The plate number, topology, and reject code, if any, are reexamined and corrected. Sectioned events are checked to make sure that all tracks are measured and none are included in two sections.

Identifying the timeslot for each plate event is also done during the set-up scan. Normally this would be done in the program PRECIS as described above. We decided that carefully using the TRIFID output to identify the proper timeslot is more accurate for plate events then using PRECIS. The reconstructed vertex from plate events is occasionally bad enough that PRECIS would pick the wrong timeslot or no timeslot at all. This can only happen if one or more of the

vertex measurements is bad. If the measurements were good the vertex would be reconstructed properly and PRECIS would give the correct timeslot. Unfortunately, because the vertex cannot be seen and must be determined by extrapolation, the measurements are sometimes bad. Using TRIFID output it is always possible to identify the right timeslot. The person doing the set-up scan records the timeslot number and the beam type. These are edited into a master list of corrected plate events for each roll. The plate version of PRECIS (PPL) which will be discussed below uses this list as input.

The final purpose of the set-up scan is to make up lists of events to be remeasured. In the complicated sequence of IPD'ing, PEPR'ing, and processing, some events are damaged in ways that will affect the physics. Tracks can be lost or mismatched, badly measured tracks can give inaccurate momenta, and whole events can be lost. We have tried to minimize the losses due to effects like these by redoing events that are affected. Most rolls of film have been through three separate passes of plate event measuring. Most events are fine after one pass. Bad events are remeasured and again most of these are good and are merged with the previous good events. Eventually only pathologically bad events are left. During the set-up scan each event is checked against the bare bubble chamber GEOHYB output (recall that PPL cannot be run until the timeslots are found so it is only possible to run UNSTYX data into GEOHYB at this point). The output for sections are compared with the sheets that were drawn by the IPD'er to make sure that the right tracks were measured and none were lost. After the scan a remeasurement list is drawn up and the bad events, or sections are redone.

The original motivation for doing the set-up scan was to identify the timeslot. In practice this scan developed into a powerful tool for removing errors from the data sample and streamlining the processing.

The version of PRECIS run for plate events is called PPL. PPL differs from PRECIS in two important ways. The event timeslot is taken from the set-up scan file rather than being found in the program. The reason for using the predetermined timeslot rather than finding it as in PRECIS was described above. In PPL an event is read in from the UNSTYX. Next the scan file is read for the information on that frame. The subroutine UNPURE is then called to unpack the desired timeslot. The cerenkov code for that beam is compared to the recorded beam type as a check. The other difference is that the vertex reconstruction is put off till GEOHYB since the vertex is not needed for finding the timeslot.

3.4) GEOHYB

GEOHYB (GEOmetry for HYBrid bubble chamber system) is the program which does the bulk of the event reconstruction. Input to GEOHYB contains raw measurements from the bubble chamber and from the various downstream devices. On output GEOHYB has reconstructed this information into a three dimensional picture of the event with each charged track represented by its momentum and direction at the vertex. This is the information needed to do physics analysis on the charged tracks. GEOHYB uses three methods to reconstruct charged tracks. First it finds straight tracks in the downstream spectrometer and

links these with their bubble chamber images. Next it reconstructs the track images not already matched using only the bubble chamber information. Last it examines these bubble chamber tracks and sees if they can be improved by using downstream data. Any track for which GEOHYB has used downstream information to improve the accuracy of its parameters is said to be "hybridized". A track hybridized by the first method above is called PIG hybridized or PIG'd (this is done in a processor called PIG). A track hybridized by the third method is called SOW hybridized or SOWed (processor SOW). Tracks which are not hybridized will be referred to as bare BC tracks. Both PIG and SOW are new concepts and are described in the appendices. PIG and SOW are used for all events incuding plate events. I will describe the major changes in GEOHYB necessary to reconstruct vertices for plate events.

The problem of reconstructing a vertex seems at first to be trivial. Given a matched point in two-dimensions in each of the three views one must project that point into space. A line called a light ray is calculated from the camera position through the point on the film (XF,YF) for each view. For a given Z the light ray parameters (A1,A2,B1,B2) give the X and Y postion:

$$X = A1*Z + A2 \qquad Y = B1*Z + B2.$$

A bubble at any (X,Y,Z) consistent with these equations yields a bubble at (XF,YF) on that view of the film. The closest approach of the three light rays, one from each view, to each other forms an estimation of the vertex point in space.

Problems arise due to large measurement errors. In particular, because of the geometry of the camera locations, a small shift in X or Y of the measurement can give a very good fit to a vertex at the wrong

Z; where the error in Z is much greater than the original error in X or Y (see figure 3-7). In both PRECIS and GEOHYB much code has been written to solve this problem. An attempt is made to see if two views yield a consistent vertex at a different Z than the three views. If so, each view is dropped in turn and the best pair is taken. This vertex is then used as a starting point in a series of programs that refine the vertex by constraining it to lie at the intersection of the measured tracks in each view. Unfortunately this last trick only works if the tracks are well measured close to the vertex; as we have seen this is not the case with plate events. Using this method without modification on plate events yields very poor results. Vertices from different sections of the same event, which after all are measurements of the same point in space, differ by several mm typically and in some cases up to cms. This is unacceptable. Reluctantly it was decided to discard the old vertex fitting routines, which still work well for the hydrogen events for which they were designed, and to try to reconstruct the plate vertices in a new and more reliable way.

A detailed look at the light rays reconstructed for different sections of the same events showed where the measuring problem lay. The spread in X position in views one and two were in general larger than in view three; and much larger than the spread in Y positions. In most cases the X position for one view was far off while the Y position from that same measurement was fine (see figure 3-8). This result is not surprising if one analyzes the events as seen in each view (see figures 3-4, 3-5 and 3-6). In all three views the beam is usually visible (the beam is sometimes invisible in view one), and

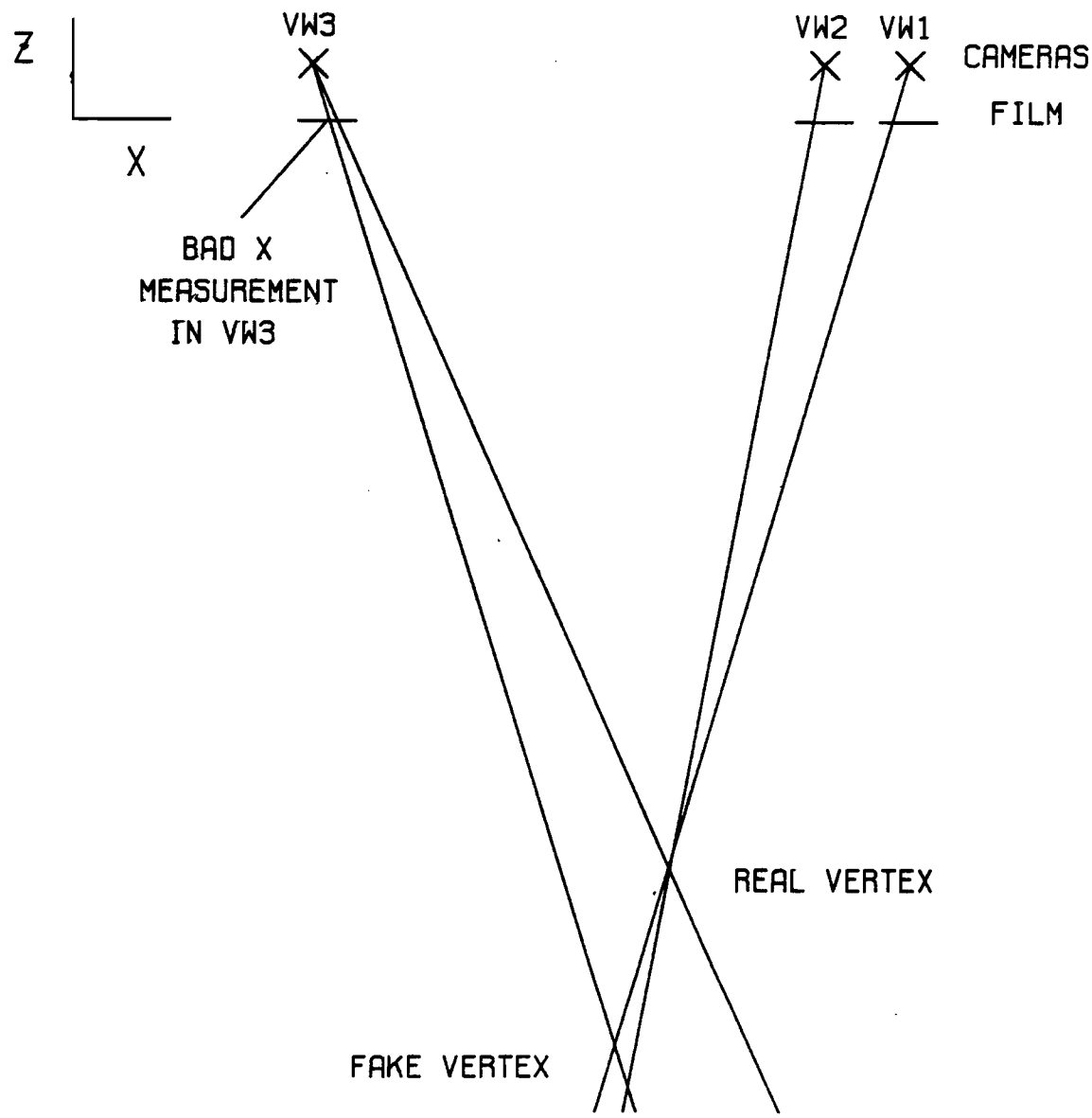

Figure 3-7: Light ray geometry.

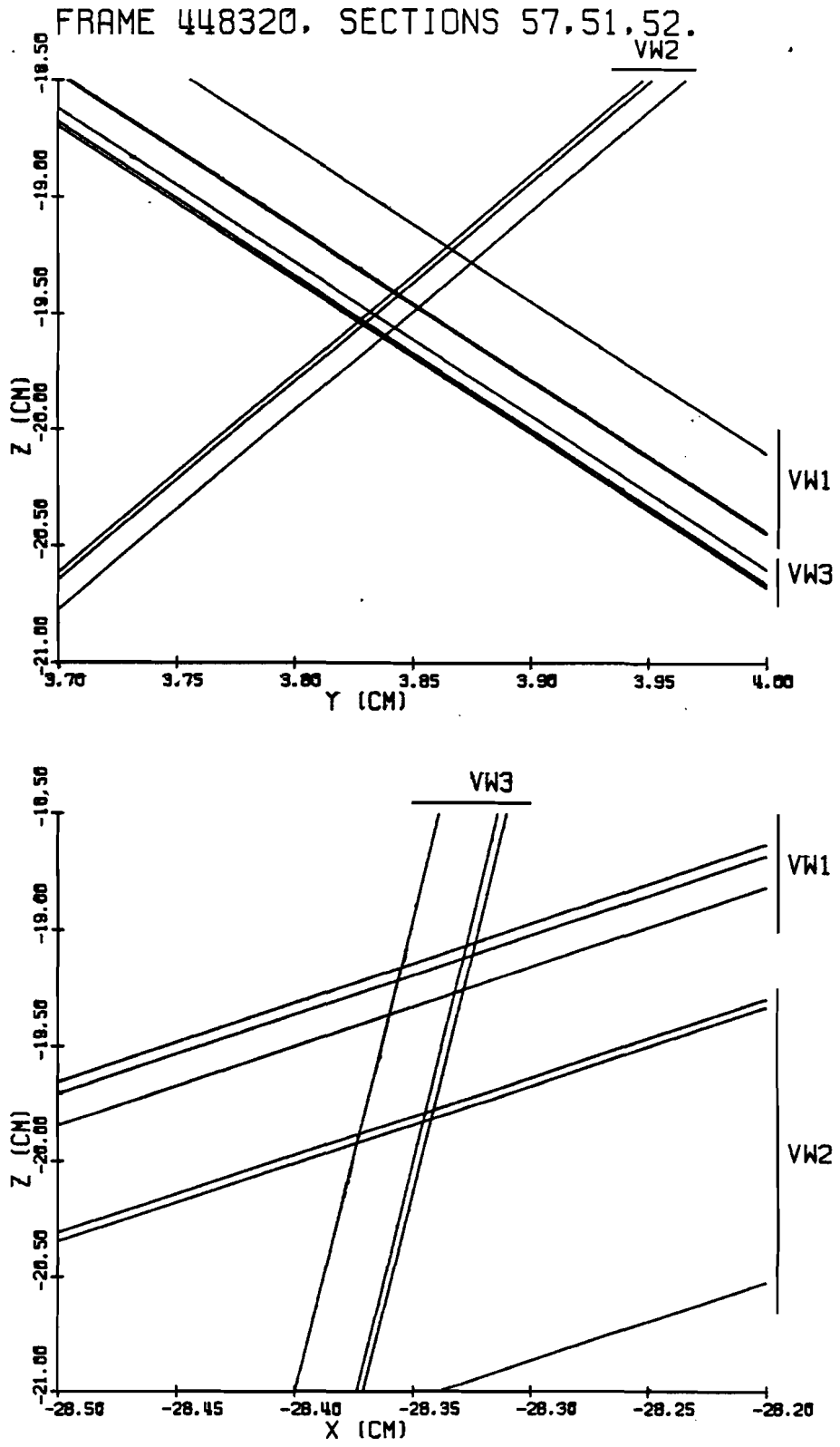

Figure 3-8: Light rays for sections 57, 51, and 52 of frame 448320.

this defines the Y position precisely even though the vertex cannot be seen. The X position is estimated by extrapolating the tracks back to a point, a process sometimes yielding large errors. In view three the plates are seen edge on and the tracks are obscured for only a short distance around the vertex. This accounts for the smaller error in X for this view. PPG, the plate version of GEOHYB, takes advantage of these facts by weighting the measurements separately for X and Y in each view. Y measurements in all views are treated equally; the X from views one and two are weighted less while the X from view three is in between. Analysis of many sectioned events led to setting the relative weights squared for the fit to :

	X	Y
View 1	0.1	1.0
View 2	0.1	1.0
View 3	0.5	1.0.

The vertex is found by a simple chi-squared fit to X, Y, and Z given the equations of the light rays properly weighted. Using this method the plate vertices for sections of the same event differ from their average value by (see figure 3-9):

$$\sigma_x = 0.25 \text{ mm} \qquad \sigma_y = 0.12 \text{ mm} \qquad \sigma_z = 0.77 \text{ mm}$$

It should be noted that vertex measurements of different sections are not entirely independent and so the real errors may be larger than these.

We made some attempt to improve the accuracy of these results by rewriting the code which fits the vertex to the intersection of the tracks. While there was some success we found that in general this would not work for these events. Some events had an improved vertex but others would get much worse, and there was no way to predict which

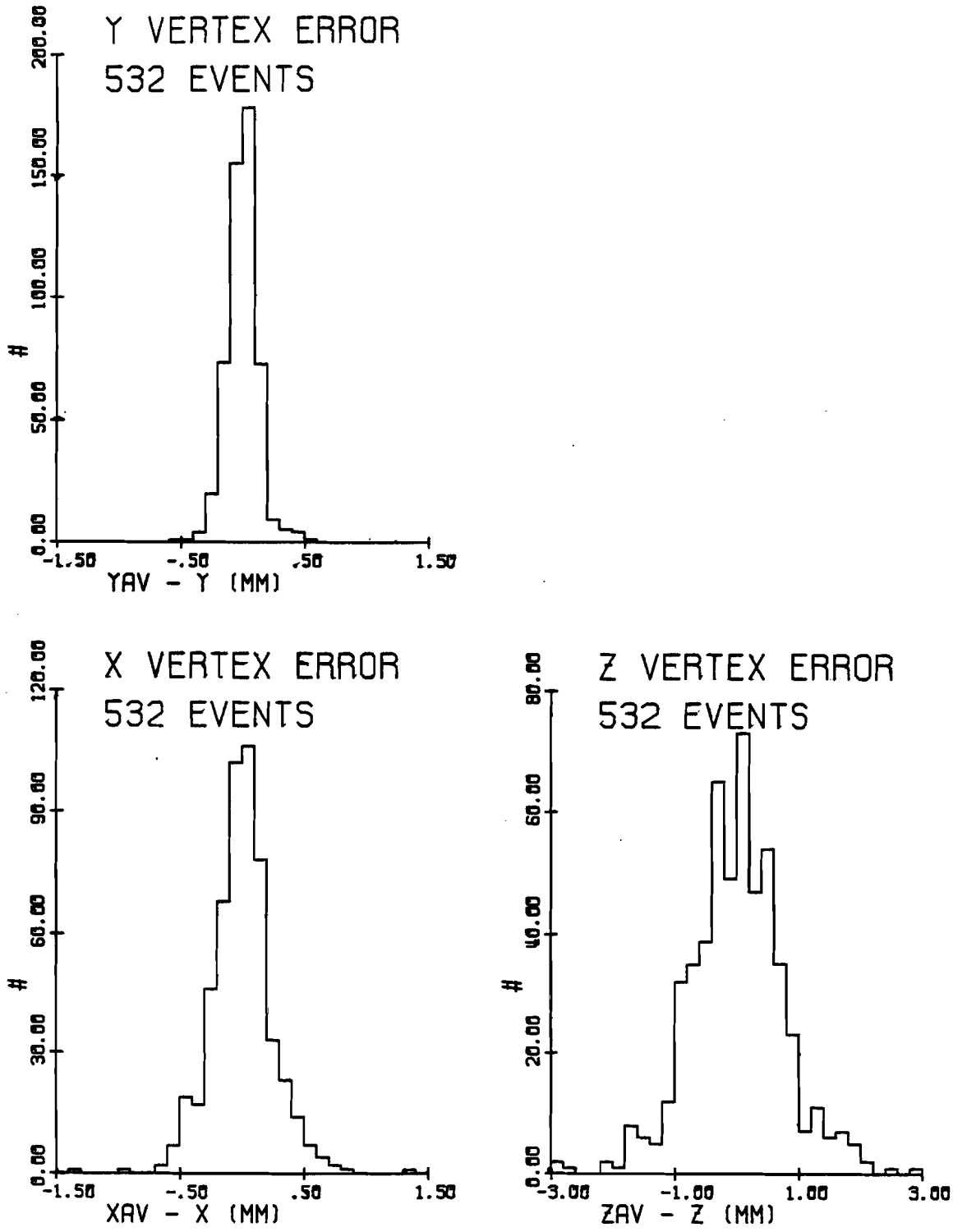

Figure 3-9: Vertex errors for sectioned events.

events would not work. Several suggestions have been made to improve the vertex by using other available information. For example, the Y and Z predictions of the beam location from the upstream PWC's, and the known X location of the plates could be used to help constrain the vertex. For the data used in this thesis only the method described in the preceding paragraph was used to find the vertex.

In order to recombine the different sections of a plate event it is necessary that they all have the same vertex. This is accomplished by using the vertex of the first section processed in PPG for all subsequent sections. The code for this change and for the different vertex fits described above are the only differences between the GEOHYB for hydrogen events and the plate version PPG.

3.5) DST and ID SCAN

The GEOHYB output contains a complete description of each event with all possible information retained. When doing analysis it is convenient to work with a simplified version of the output with only the needed quantities extracted. Such a simplified output is called a data summary tape (DST). My DST for plate events has a very simple format which makes it easy to read and also easy to edit. This second feature is needed because a final check of the data after GEOHYB is done, and the corrections from this check, must be incorporated. The main task of the final check, called the ID scan is to identify low momentum secondaries.

Momentum and angle fits produced by GEOHYB will depend, for low momentum tracks, on the mass of the particle assumed to make the

track. This is because GEOHYB will take into account the energy loss of the particle in the liquid H_2 when performing the final fit. For low (< 3 GeV/c) momentum tracks GEOHYB will try three mass hypotheses; pion, kaon, and proton. After each fit the track is projected into each of the three views and a mean residual or distance to the measured points is calculated. The mass hypotheses are ordered by mean residual with the lowest being output first; all masses which make acceptable fits are output. Choosing a mass for the secondary based upon this information, or the other related quantities available, chi-squared or probability for the fit, is often not accurate. This is especially true in plate events where the secondaries may not be measured near the vertex. We would like to identify low momentum secondaries accurately since this information is available on the film. To do this a second physicist scan, the ID scan, was included in the plate event processing chain (figure 3-2).

The ID scan is a final check of each event in keeping with the philosophy of insuring the maximum information from each of our interactions. While some mistakes cannot be fixed at this stage we at least get a measure of the rate of errors in the data. There are three basic tasks performed in the ID scan:

- protons, pions and electrons with low enough momenta are identified by ionization in the bubble chamber

- all tracks reconstructed by GEOHYB are checked for mistakes in sign, momentum, etc.

- tracks missed or not reconstructed are recorded here.

A charged paricle going through the H_2 in the bubble chamber will ionize the liquid around its path. It is this ionization that produces the cores of the bubbles that will grow and make the visible

track. The energy loss to ionization by a charged particle follows the Bethe-Bloch equation:

$$\frac{dE}{dx} \propto \frac{Z^2}{\beta^2} + \text{higher order terms.}$$

Recall that the momentum of a track is known from its curvature in the magnetic field. Thus for a given momentum the energy loss for different masses varies only by the β^{-2} term above. The relativistic rise in ionization at high momentum which is utilized in the CRISIS detector for particle identification is not seen in liquid H_2. The more energy lost to ionization the more bubbles produced and so the darker the track. By visually examining the darkness of a track and knowing its momentum one can separate electrons from pions up to 140 MeV/c, and pions from protons up to 1 GeV/c. These ranges can be extended a little if the frame is clear and the tracks are not dipping sharply. In addition, if the particle loses enough energy to stop in the bubble chamber it can be identified by comparing its momentum from curvature to its expected momentum from range.

In practice the physicist doing this scan will compare each event to the GEOHYB listing. This listing contains the momentum of each reconstructed track. For all tracks that can be identified the particle type is recorded on the listing. Tracks which are ambiguous are recorded as pions.

If GEOHYB reconstructs a track the odds are very good that it has been done correctly. In a small number of cases however a mistake is made. This happens most often on tracks such as short decays or interactions, when the track length is insufficient to properly reconstruct the sign from the curvature. For both of these cases it

is usually easy to tell what the proper sign should be. Decays and interactions must conserve charge and so by examining the signs of their products the sign of the original particle can be determined. Any track with the wrong sign is corrected on the GEOHYB listing. GEOHYB needs only two views to reconstruct a track. Although three view combinations are always tried first, sometimes these two view tracks are taken. Ocasionally GEOHYB will take the track images left over from these two view reconstructions, put them togeather, and come up with fictitious track reconstructions. Since these tracks do not appear on the film they are usually easy to identify and strike off the listing. This happens for less than 1% of the tracks output by GEOHYB.

Some tracks are not reconstructed by GEOHYB. While this may be due to an error somewhere in the chain the usual reason at this stage of processing is that the track is not visible in two views. Often this is the case for short tracks, tracks at large angles into the cameras, or tracks going backwards in the lab. These tracks are usually slow and their momentum can be estimated from curvature or range. Another class of unreconstructed tracks is slow electrons. GEOHYB does not try an electron hypothesis, and pions below 100 MeV/c will not fit an electron track of that momentum. During the ID scan the estimated momenta, particle ID, sign, and a rough phi angle are recorded on the listing for all tracks which were not reconstructed. This information is not as reliable as the usual GEOHYB fit but it is useful for certain physics problems. In particular complete sign and particle ID data is needed when examining the multiplicity and net positive charge. The number of tracks inserted in this way is only 4%

of all tracks. Most of these tracks are short or backward protons and electrons. The rest, about 1% of all tracks, are tracks which should have been reconstructed but were lost. If the information for these added tracks was used it will be specifically mentioned as the analysis is discussed.

All of the information from the ID scan is edited into the DST format. Tracks whose masses are identified, added tracks, changed tracks, and fictitious tracks are all identified by labels. In addition the original GEOHYB tracks are kept so that they may be examined if desired. This edited DST is the final result of all the work described thus far. Up till now all processing was designed to produce a DST with as much complete information, and as few errors as possible. We can now discuss the physics analysis of this data.

4) PHYSICS ANALYSIS

4.1) DATA SAMPLE

We report on the results from 20 rolls acquired and processed as described in the last two chapters. The total number of events in the sample is 809. Table 4-1 details the nonbiased rejects removed from the sample by scanning and TRIFID criterion. By nonbiased I mean that these events were rejected on the basis of criteria that did not depend on the event, but on the beam or on other events in the frame. These events should not be biased in any physical parameters. This is important since almost half of the events are rejected in this way. Figure 4-1 shows the scanned topology distributions for the nonbiased rejects and completed events. Note that there is no evidence for a difference in these two distributions.

Figure 4-1 also shows the topology distribution for the 15 events which were rejected or lost in a biased fashion. Ten of these events were ones for which the correct topology could not be counted due to interactions close to the vertex. Tracks from these interactions could not be resolved from real secondaries (the topology plotted is a guess of the real topology). The probability that this will occur increases with the number of tracks which can interact so it is expected that these events will be biased towards high multiplicities. In addition five more events were lost in processing. These include events where at least one section failed in PEPR or GEOHYB. Again the probability of this happening increases with the complexity of the event, so these events are also biased. Details of these fifteen events are shown in table 4-2.

	Plate number (element)						
	1(Ag)	2(Ag)	3(Au)	4(Au)	5(Mg)	6(Mg)	Total
Total events	233	122	149	178	87	40	809
Nonbiased rejects							
132	43	22	22	29	8	7	131
133	28	23	17	22	4	2	96
134	0	1	0	0	0	0	1
136	28	9	20	23	15	6	101
	99	55	59	74	27	15	329

132 = too many incoming tracks

133 = beams too close in space (TRIFID)

134 = faint or missing view

136 = Cerenkov failure (TRIFID)

Table 4-1: Nonbiased rejects.

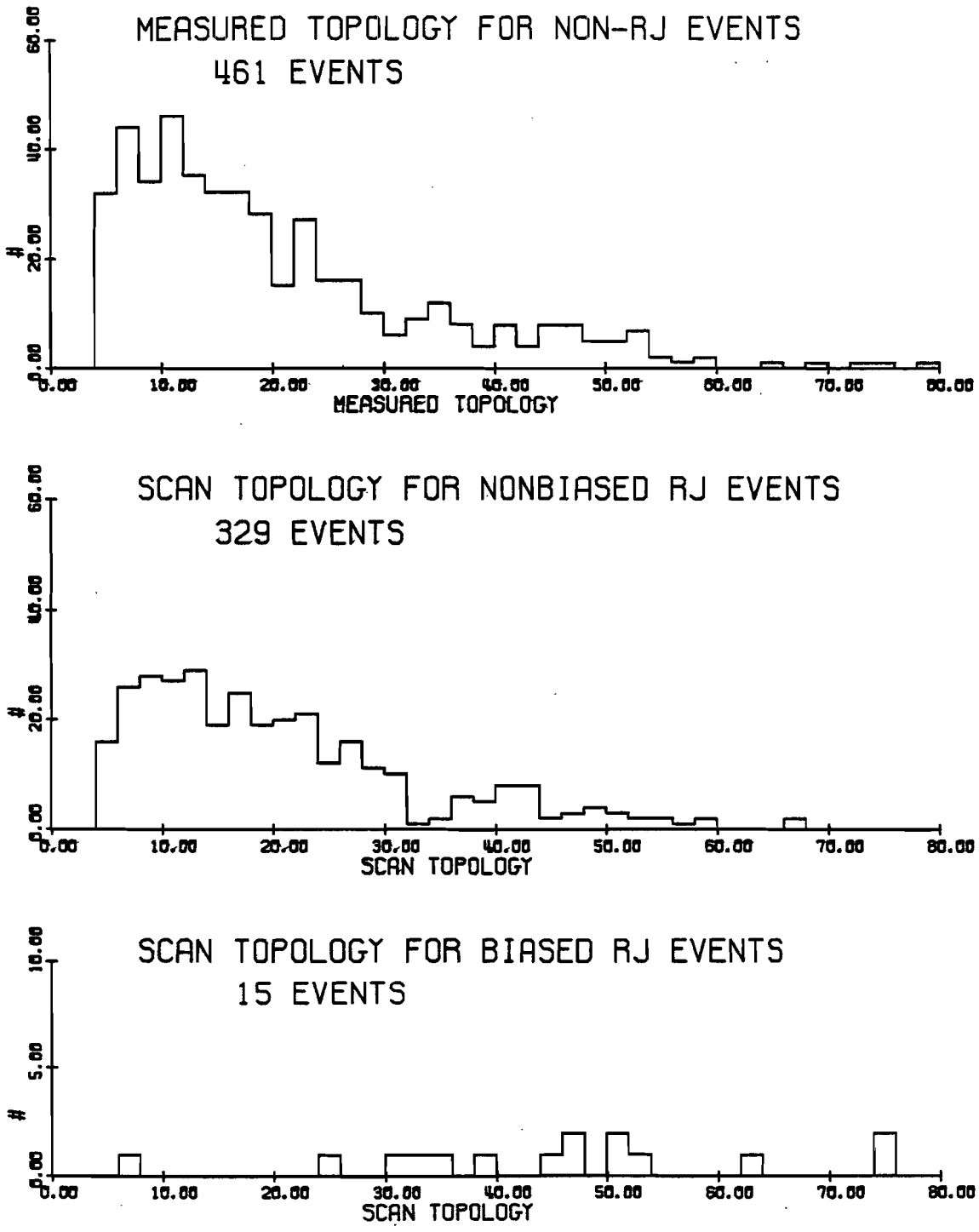

Figure 4-1: Topology distributions for nonrejected events, nonbiased rejected events and biased rejected events.

Biased rejects - Close interactions

Roll	Frame	Scan topology	Plate	Beam
2235	361931	38	2-Ag	p
2248	404598	46	4-Au	K
2249	406093	74	3-Au	p
2255	425964	52	3-Au	p
2257	430875	74	3-Au	π
2257	431348	33	4-Au	p
2259	438441	50	3-Au	p
2264	454722	8	5-Mg	p
2266	459994	62	1-Ag	p
2269	470432	30	5-Mg	π

Biased rejects - Processing loss

Roll	Frame	Topology	Plate	Beam	Where lost
2240	379223	50	4-Au	π	PEPR
2257	430277	44	4-Au	p	GEOHYB
2262	445868	25	3-Au	p	GEOHYB
2264	453408	35	4-Au	π	PEPR
2267	463353	46	1-Ag	π	PEPR

Table 4-2: Biased rejected events.

Nothing can be done with events with close interactions. Considerable effort was expended by both measuring staff and physicists to insure that the additional number of lost events was as small as possible. We are very proud that this data sample contains a majority of complete events up to all multiplicities.

The final sample for analysis contains 461 events. They are distributed over the beams and target types as shown in table 4-3. This sample contains 9160 total tracks. A breakdown of these tracks is shown in table 4-4. Tracks listed as missed were those which were picked up in the ID scan (see section 3.5).

We have restricted ourselves to events with more than three charged secondaries. The efficiency for seeing 2 prong interactions is low and elastic scatters off the nucleus should be treated separately from the inelastic collisions which we will be examining. Three prong events have a significant inelastic component but this is hidden by a large background of apparent 3 prong events consisting of the original projectile and an $e^+ e^-$ pair produced by electromagnetic interactions with the nucleus. Our inability to distinguish these events from real three prongs leads us to throw out this category as well.

In the following, some results will be compared to H_2 events. These H_2 events are also from E565/570. They were measured and processed at Rutgers in the usual way and are included to give a high statistics sample with low systematic differences to compare with the plate events.

		π	K	p	all
Plate -	1-Ag	45	18	66	129
	2-Ag	28	10	28	66
	3-Au	39	18	27	84
	4-Au	46	15	38	99
	5-Mg	16	9	33	58
	6-Mg	11	2	12	25
Element -	Ag	73	28	94	195
	Au	85	33	65	183
	Mg	27	11	45	83
Total		185	72	204	461

Table 4-3: Final analysis sample.

461 Events

Total Tracks	9160			
Fast unidentified	4609			
Pions	2405			
Protons	1577			
Electrons	109			
Scanned dalitz electrons	185			
Missed	275	⟶	133	pion or fast
			103	proton
			39	electron

Fictitious tracks $\frac{84}{9160} = 1\ \%$

Missed tracks $\frac{275}{9160} = 3\ \%$

Table 4-4: Track summary.

4.2) CROSS-SECTIONS

This experiment was not designed as a precision measurement of the cross-sections as our statistics are limited. The cross-sections are presented for completeness and to show that we are in the right range.

For each roll TRIFID prints out a summary which includes a count of the number of beams which traverse each plate (see section 3.1). These totals are also broken down by beam type. This beam count includes all beams; before comparing to our events we must correct for the fraction of rejected events. The ratio of good events in each plate to all events in that plate is used to correct the beam totals from TRIFID.

We then calculate the cross-section:

$$\sigma = \frac{A}{\rho\ L\ N_0} \frac{N_{ev}}{N_{beam}}$$

N_{ev} = number of events A = atomic weight

ρ = density L = plate thickness

N_{beam} = number of beams N_0 = Avogadro's number

Table 4-5 shows the value of $(A/\rho L N_0)$, N_{ev}, and the corrected N_{beam} for each plate. We combine the two plates of each element and calculate the cross-sections shown in table 4-6. The errors include statistical errors on the number of events and also on the correction factors for the beams. The nominal cross-sections from ref. 35 are included for comparison. Our values are systematically low as we have not included one through three pronged inelastic interactions. It is

Plate	$\frac{A}{\rho L N_0}$ (cm^2)	N_{beam}			N_{ev}		
		π	K	p	π	K	p
1-Ag	9.49×10^{-23}	8082	2548	5544	45	18	66
2-Ag	2.85×10^{-22}	13540	4258	9122	28	10	28
3-Au	5.77×10^{-22}	15367	5510	11393	39	18	27
4-Au	1.92×10^{-22}	7732	2439	5343	46	15	38
5-Mg	6.27×10^{-23}	6809	2166	4838	16	9	33
6-Mg	2.09×10^{-23}	1848	574	1327	11	2	12

Table 4-5: Quantities used in cross-section calculation.

Carroll et al., ref. 35.

Element	Beam:	π	K	p
Au		1447	1349	1728
Ag		916	844	1120
Mg		295	264	383

This experiment, uncorrected for 1-3 prongs.

Element	Beam:	π	K	p
Au		1290 ± 220	1560 ± 270	1370 ± 280
Ag		550 ± 145	670 ± 185	1050 ± 165
Mg		140 ± 70	230 ± 85	360 ± 90

This experiment, corrected.

Element	Beam:	π	K	p
Au		1380 ± 220	1660 ± 270	1460 ± 280
Ag		600 ± 145	720 ± 185	1130 ± 165
Mg		160 ± 70	260 ± 85	410 ± 90

Table 4-6: Cross-sections in millibarns.

known that KNO scaling gives a very good fit to the topological cross-section for hadron-nucleus interactions (see for example ref. 36 and 37). We use KNO scaling, and the parameters of the topological cross-section for pp from ref. 38, to estimate the events lost. Above the smooth KNO backround are spikes at 1 and 3 in the topological cross-section for coherent production, we also correct for these events using the data in ref. 39. Table 4-6 shows the cross-section after correcting by 6 % for Au, 7 % for Ag, and 13 % for Mg. An overall chi-squared for all values is 11.6 for 9 degrees of freedom showing that our result is consistent with ref. 35.

4.3) MULTIPLICITIES

As discussed in the introduction, the charged multiplicity is an important observable in hadron-nucleus interactions. Great care was taken in the data analysis to insure that a record of each visible track is included on the DST. Still there are large corrections to be made to these raw data. We must correct for electrons that come from pi-zeros. These electrons are either directly produced in dalitz decays of the pi-zero or are produced when gamma rays from the pi-zero decays convert in the metal plate. In either case we would like to remove these electrons from the charged multiplicity.

We assume that the number of pi-zeros produced is equal to half the number of charged pions (this is true in hadron-hadron interactions, see ref. 40). Since we cannot identify all pions and since the background from protons is much larger in the positive than the negative secondaries we will take the number of pi-zeros produced

to be equal to the number of negative pions. Define B and BN to be the observed multiplicity and the observed negative multiplicity respectively. Let A and AN denote corresponding real multiplicities (corrected for electrons). Then :

$$B = A + AN*C$$ where C is the number of electrons produced per pi-zero. Also for the negatives:

$$BN = AN + \frac{AN*C}{2} .$$

Solving for A in terms of measurable quantities:

$$A = B - \frac{2*BN*C}{2 + C} .$$

To calculate C we look at the possible decay modes of the pi-zero. Pi-zeros can decay to 2 γ's (98.802 %) or to $e^+ e^- \gamma$ (1.198 %). The γ's which are produced can convert to $e^+ e^-$ pairs inside the plates (conversions in the H_2 can be seen and are not included in the observed multiplicity). Thus:

$$C = (98.802\%)(2)(2)(1 - e^{-L/X}) + (1.198\%)(2)(1 + 1 - e^{-L/X}).$$

Where X is the radiation length of the metal, and L is one half the thickness of the plate (the average distance traveled by a γ inside the plate). Table 4-7 shows the value of C for each plate.

Using these results we can correct each event for the average number of electrons included in its charged multiplicity. Since we are correcting for electrons we must include the identified electrons in B and BN. Table 4-8 shows the raw and corrected average multiplicities for each beam and target. All future reference to multiplicities will be to the corrected values.

The events which are biased rejects are not included in these calculations as we do not have complete information for them. We can

Plate	L (cm)	X (cm)	C	$\frac{2\,C}{2 + C}$
1-Ag	0.090	0.86	0.419	0.346
2-Ag	0.030	0.86	0.160	0.148
3-Au	0.015	0.34	0.196	0.178
4-Au	0.045	0.34	0.517	0.411
5-Mg	0.135	14.39	0.061	0.059
6-Mg	0.550	14.39	0.173	0.159

Table 4-7: Quantities for calculating mutiplicity correction factor.

Element	Beam	Raw Multiplicity	γ corrected Multiplicity	RJ corrected Multiplicity
Au	π	20.2 ± 1.5	17.4 ± 1.3	18.3
	K	19.7 ± 2.2	17.1 ± 2.0	18.0
	p	28.0 ± 2.3	24.2 ± 2.0	25.5
Ag	π	18.8 ± 1.4	16.3 ± 1.2	16.6
	K	17.1 ± 2.3	14.6 ± 2.0	14.6
	p	21.0 ± 1.5	18.0 ± 1.3	18.6
Mg	π	13.0 ± 1.2	11.7 ± 1.1	12.2
	K	13.7 ± 2.1	12.6 ± 2.1	12.6
	p	14.6 ± 1.4	13.5 ± 1.3	13.3

Table 4-8: Average multiplicities.

estimate the effect of not including these events on the average multiplicity. The third column of table 4-8 gives the corrected multiplicities; significant changes occur only in a few bins. In the analysis that follows we will examine average multiplicities versus variables that we cannot supply for the missing events and so we will not be able to correct for them.

4.4) NET CHARGE & OBSERVED PROTONS

The net charge of an event (positive secondaries - negative secondaries) is an important indication of how many collisions took place inside the nucleus. If one assumes that collisions may be considered independently, at least in the sense that they must conserve charge, then on average the net charge Δ is:

$$\Delta = 1 + \nu \frac{Z}{A}$$

where ν is the number of collisions and $\frac{Z}{A}$ is the fraction of protons in the nucleus. The first term comes from the charge of the beam. Each collision with a neutron adds zero to the net charge, while proton collisions add plus one. It is not necessary to correct the net charge for pi-zero conversions since these always yield a plus-minus pair. The average net charge for each beam and target type is shown in table 4-9.

The distribution of net charge with momentum is important in determining the features of the multiple collisions inside the nucleus. Previous work published by the E565/570 consortium based on data from an engineering run (ref. 14) indicated that there was a larger than expected net positve charge at high momentum. This result

Average net charge

Element	π	K	p
Au	5.87 ± 0.60	6.15 ± 0.94	8.42 ± 0.88
Ag	5.23 ± 0.47	5.18 ± 0.97	5.72 ± 0.63
Mg	2.81 ± 0.39	2.00 ± 0.52	3.60 ± 0.37

Table 4-9: Average net charge.

was unexpected because it would mean that fast secondaries must be reinteracting inside the nucleus. As noted in the introduction, this is not expected when one considers the formation lengths of these secondaries. The distribution of net charge with momentum is shown in figure 4.2. Note that this is an integrated plot, at each momentum the net charge of all secondaries of lower momentum is shown. For comparison the same quantity is plotted for E565/570 H_2 events.

Table 4-10 shows a comparison of the net charge data from our previous paper (ref. 14) and from the current data sample. The older result had a cutoff at low momentum so the lowest bin is not as large as in this sample where no explicit cutoff was made. Note that the higher momentum bins have a lower net charge in the new data; and that this number is more consistent with the H_2 values given for comparison. The new data is also consistent with the data presented in references 18 and 19. Our current data indicate that the net charge of the plate events is consistent with being caused by slower secondaries reinteracting, while the projectile carries its charge through the nucleus as in a collision with one nucleon.

The particle type of the extra positive secondaries is also of interest. Other results have indicated an excess of positive protons (ref. 16), with some protons too fast to be identified. If the excess is due to protons it is easy to explain as the nucleus is full of protons which can be knocked out in low energy collisions. We have identified protons up to about 1 GeV/c. Protons which could not be identified by ionization are referred to as unidentified protons. The average number of protons per event and the average below 0.9 GeV/c

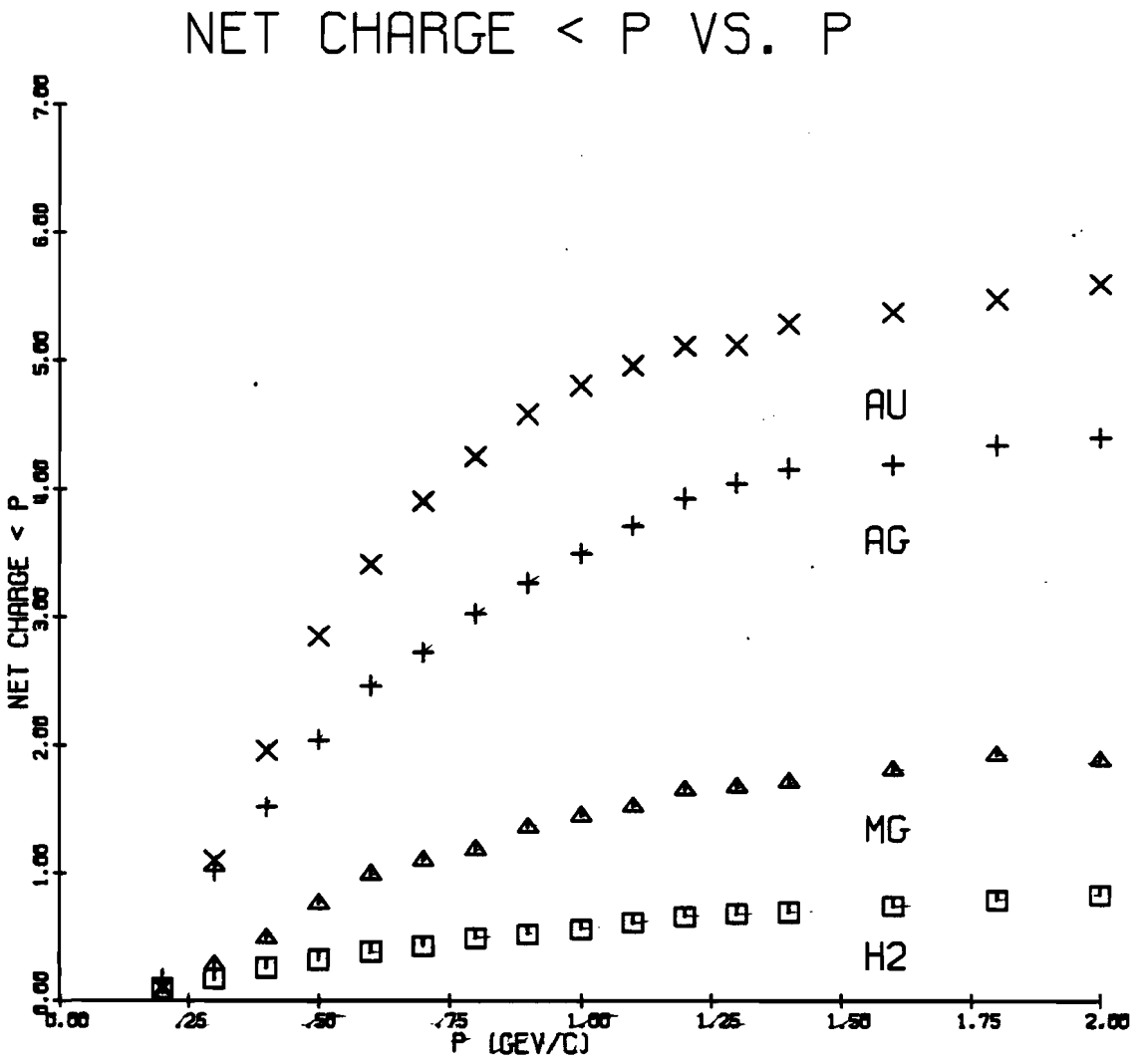

Figure 4-2: Net charge less than p versus p.

Net charge integrated over beam type.

	Au	Ag	Mg	H_2	Ref. 14
p < 0.9 GeV/c	4.54±.38	3.34±.31	1.36±.25	0.52±.04	——
p < 2.0	5.54±.44	4.36±.38	1.88±.27	0.83±.04	1.20±.35
2.0 < p < 4.0	0.41±.12	0.19±.10	0.22±.15	0.14±.03	0.60±.30
4.0 < p	0.87±.12	0.89±.10	1.04±.14	1.03±.04	1.85±.30
all p	6.83±.46	5.46±.38	3.13±.25	2.00*	

* - only events with a net charge of 2 were used in the H_2 sample

Protons $\langle n_p \rangle$ integrated over beam type.

	Au	Ag	Mg
p < 0.9 GeV/c	4.40±.36	3.32±.28	1.27±.19
all p	4.74±.40	3.58±.30	1.36±.19

Table 4-10: Net charge and protons binned by momentum.

are given in table 4-10. Note that the average number of protons below 0.9 GeV/c, where our efficiency is high for identifying protons, is the same as the net charge below 0.9 GeV/c within errors. We will look at this problem graphically in two ways. First, figure 4-3 shows the identified protons below momentum p versus p. This plot is to be compared with figure 4-2, which is the same kind of plot for Δ. Overlaying these two plots shows that up to about 0.9 GeV/c the two distributions are the same. Above this value we can make the following observations. The charge excess is small compared to that below 0.9 GeV/c. Our efficiency for identifying protons also decreases here. We claim that these data indicate that the net positive charge is made up, at least in large part, by protons knocked out of the nucleus. Another way to see this is to plot the positive pions below p vs. p (figure 4-4). These curves are significantly different at all momenta than those in figure 4-2. The multiplicity of positive pions is greater for Mg and less for Au than the net charge. The curves for Ag are close. The net charge in pions is shown in figure 4-5. These curves are consistent with zero up to 0.9 GeV/c. Some of the increase for momenta higher than 0.9 GeV/c must be due to unidentified protons.

To reiterate, our data show that the net positive charge is made up of slow particles, except for a fast projectile component that looks like hp scattering. These slow particles are almost all protons and are consistent with being entirely protons. They are probably knocked out of the nucleus in the collisions of slow secondaries as they percolate out of the nucleus.

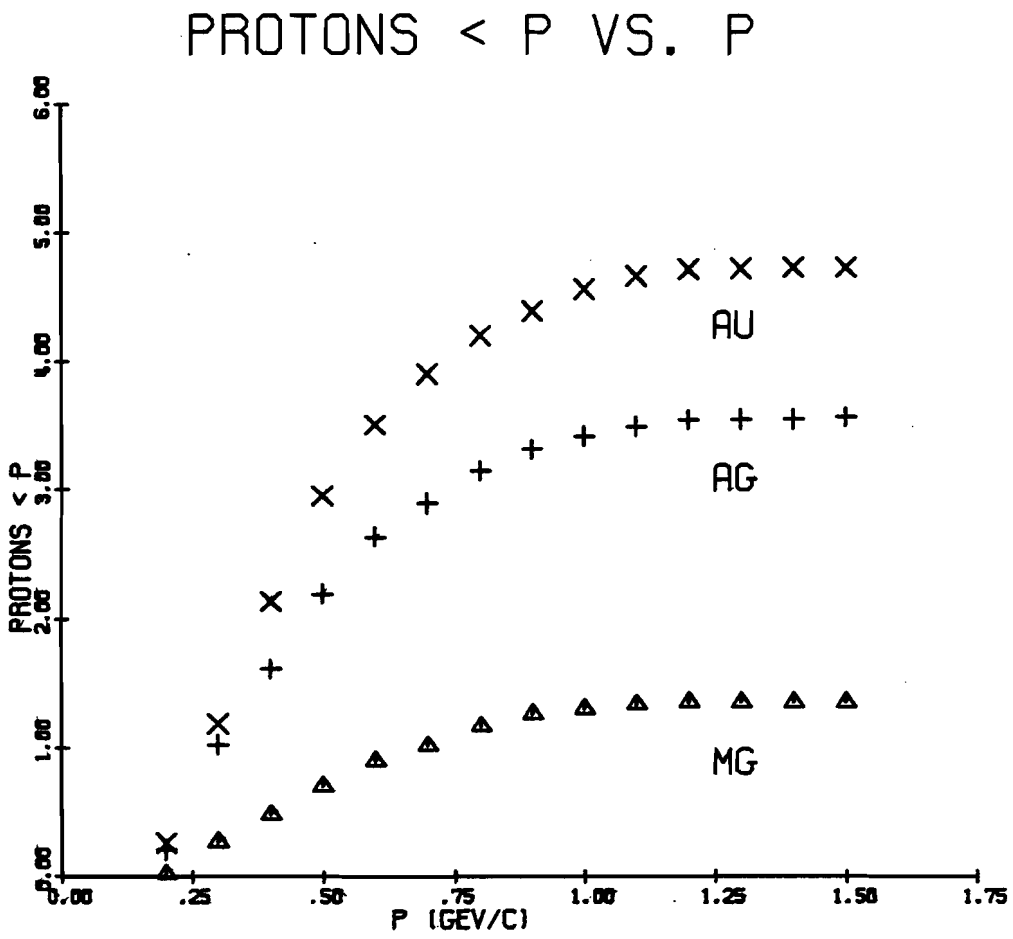

Figure 4-3: Protons with momentum less than p versus p.

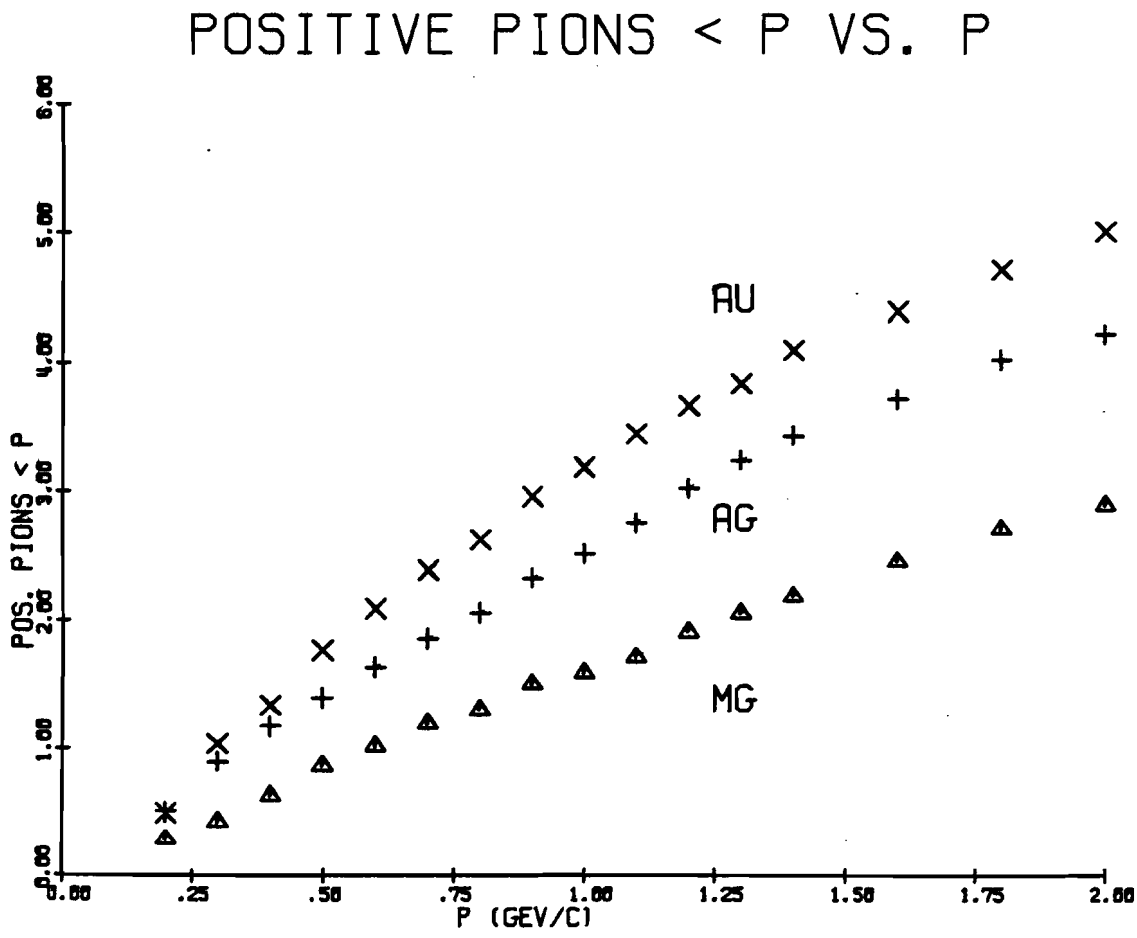

Figure 4-4: Positive pions with momentum less than p versus p.

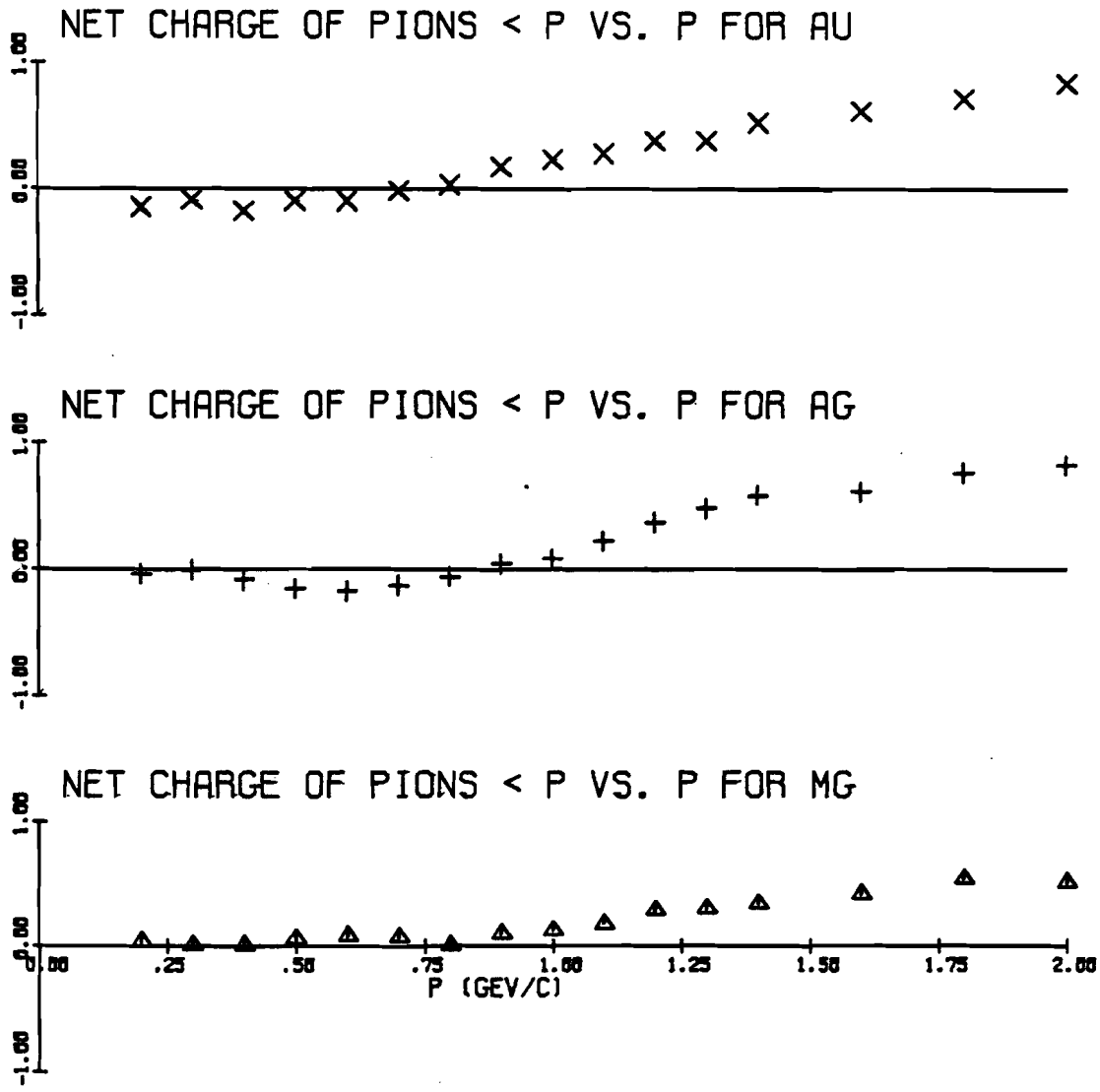

Figure 4-5: Net charge of pions with momentum less than p versus p.

4.5) PROJECTILE COLLISIONS

In the past few sections we have been considering differences between the interactions by different beams in different plates. We have known for some time that hadron-nucleus interactions have some features which depend only on the impact parameter of the event. If events are grouped by impact parameter then the nucleus type or beam type are not important; of course different nuclei will contribute different portions of their events to each impact parameter bin. The impact parameter cannot be directly measured but it is believed that it can be estimated by such parameters as ν_p the number of projectile collisions. As stated in the introduction, the average value $\langle\nu_p\rangle$ can be calculated for each nucleus; table 4-11 shows the average values of ν_p for each of our beams and targets.

The divergence about the average value of ν_p is large. We could avoid that problem by using ν_p for each event but unfortunately ν_p cannot be measured directly. Several methods have been proposed to relate ν_p to n_p the number of protons identified in the data (see ref. 3 and 4 and introduction). Using $\nu_p(n_p)$ has several advantages over using $\langle\nu_p\rangle$. First the dispersion is less in $\nu_p(n_p)$ (ref. 5). Also the range is larger; we have data out to over seven in $\nu_p(n_p)$ while $\langle\nu_p\rangle$ does not go over four. We use the relation due to Chao, et al. (ref. 5):

$$\nu_p(n_p) = \langle\nu_p\rangle \sqrt{n_p / \langle n_p\rangle} \quad .$$

The charged particle multiplicity depends on ν_p and not on target type as seen in figure 4-6. In this plot the corrected charge

Element	Average number of projectile collisions $\langle \nu_p \rangle$		
	π	K	p
Au	2.76	2.53	3.65
Ag	2.39	2.22	3.09
Mg	1.68	1.60	2.03

Table 4-11: Average number of projectile collisions by beam and target.

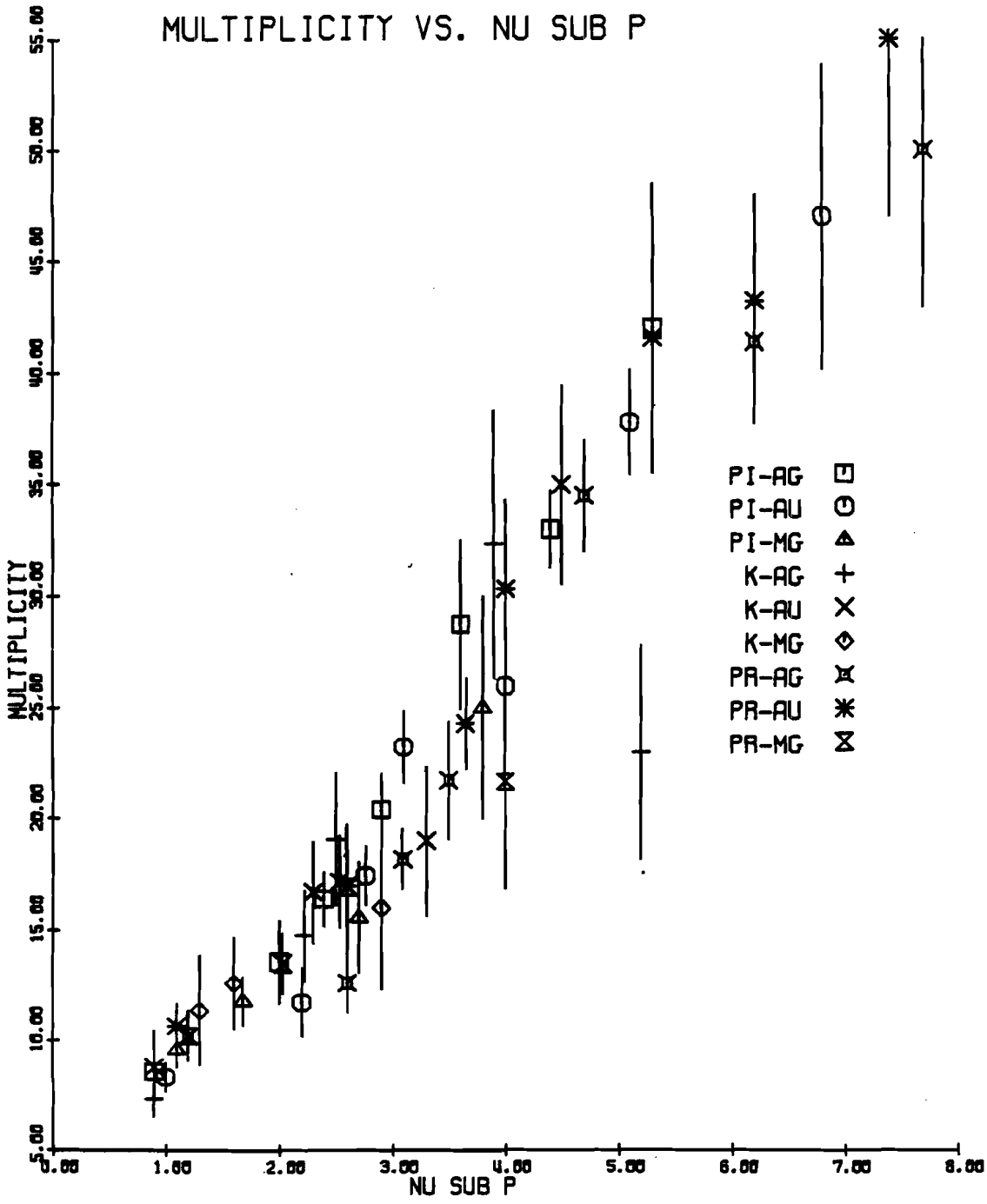

Figure 4-6: Average multiplicity versus projectile collisions.

multiplicity is plotted versus ν_p using the number of observed protons and the equation above. Points for different beams and targets are plotted separately, also the average multiplicity for each beam and target is plotted at $\langle\nu_p\rangle$ from table 4-11. The data covers a range of ν_p out to 7.7. Note that the points for different beams and targets all seem to lie along the same line. Many other experiments have noticed the linear trend in the multiplicity with ν_p. Different groups have measured the slope of the line to be different (see the data from several experiments plotted in ref. 5). We average over targets and fit the slope C in the standard form:

$$\frac{\langle N(\nu_p)\rangle}{\langle N_{hp}\rangle} = C\ (\nu_p(n_p) + 1)$$

, where $\langle N_{hp}\rangle$ is the average multiplicity for hadron-proton interactions, and $\langle N(\nu_p)\rangle$ is the average multiplicity as a function of projectile collisions. The results for our three beams are consistent with each other:

$$C_\pi = 0.70 \pm 0.11, \quad C_K = 0.68 \pm 0.20, \quad C_p = 0.73 \pm 0.12.$$

The slope is larger than that seen in some other data (ref. 20) but this is probably due to our inclusion of all charged tracks. Other groups use a low momentum cutoff and present the multiplicity of "produced particles". Depending on where the cutoff is set the slope will change; the fact that the data still lies along a straight line indicates that such a cutoff is unnecessary. One experiment which measured produced particles using some momentum cutoff has reported larger multiplicities (a larger slope) in K^+-A interactions than in π^+-A (ref. 6). This does not seem to be the case in our data.

We can also extract the dependence of secondary collisions ν_s on the number of projectile collisions from our data. From the raw data

we find the net charge Δ as a function of observed protons n_p. Using the equation above we can plot Δ versus $\nu_p(n_p)$, figure 4-7. Note that Δ depends on the beam and target as well as ν_p. This is expected as we know that Δ is roughly linear with n_p (see sec. 4.4), and so cannot be linear with ν_p. Now we can use the relation between Δ, ν_p, and ν_s given in section 4.4 to plot:

$$\nu_s = (\Delta - 1)\frac{A}{Z} - \nu_p \ .$$

The number of secondary collisions versus projectile collisions is shown in figure 4-8. The solid line in each plot is $\nu_s = \nu_p^2 - 1$ which fit the data reported in ref. 20. This function also fits our data if it is averaged over targets, but it does not fit the data for each target separately. The Mg data are consistently below this curve while the Au data are above the curve. These facts are an indication that the secondary collisions, while depending strongly on the impact parameter of the event, also depend on the nucleus involved. This is not too surprising since regardless of the impact parameter secondaries exiting the nucleus will have more nucleus to travel through in Au than in Mg. It seems from the data that the secondary collisions also depend on the beam type but not as strongly as on the target. For all targets the proton data adhere more closely to the solid line than do the meson data. The errors are too large to make more definitive statements.

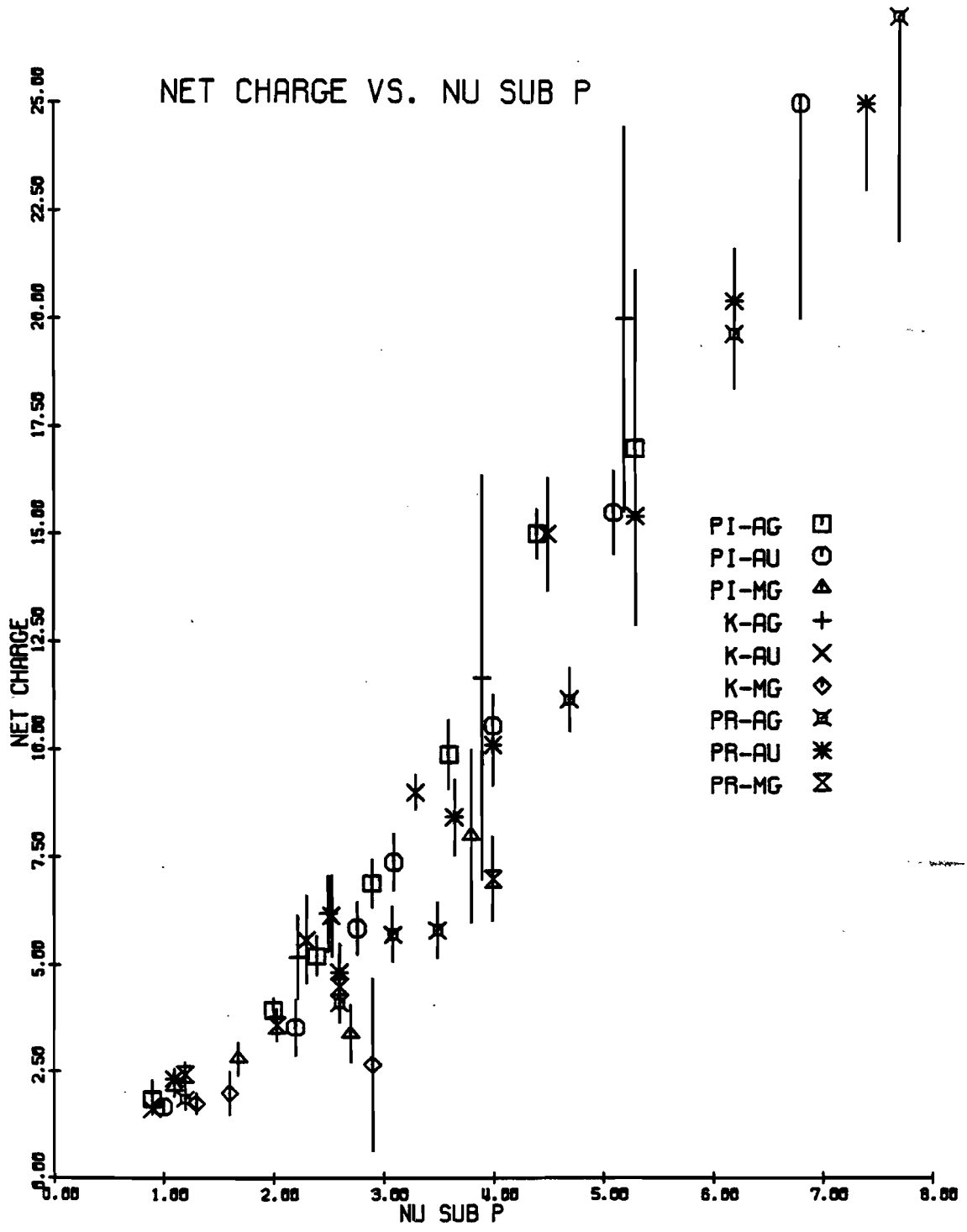

Figure 4-7: Net charge versus projectile collisions.

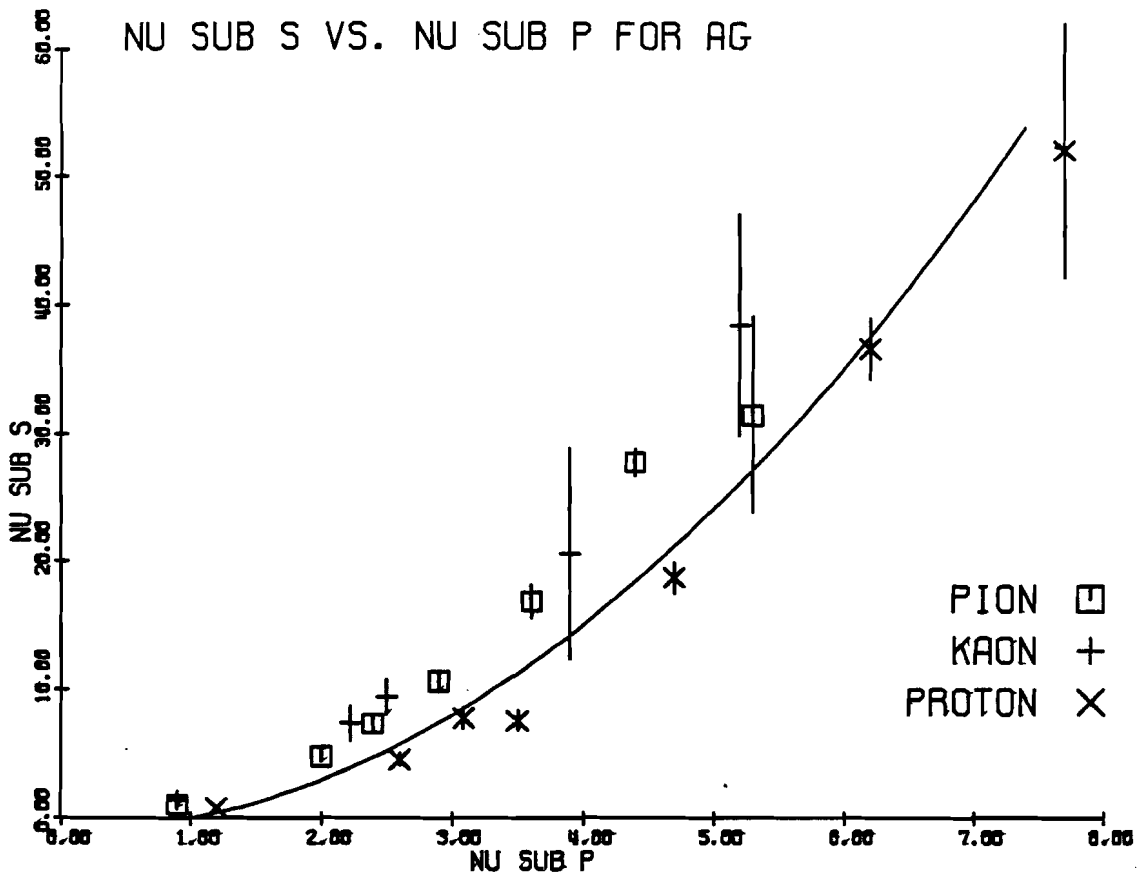

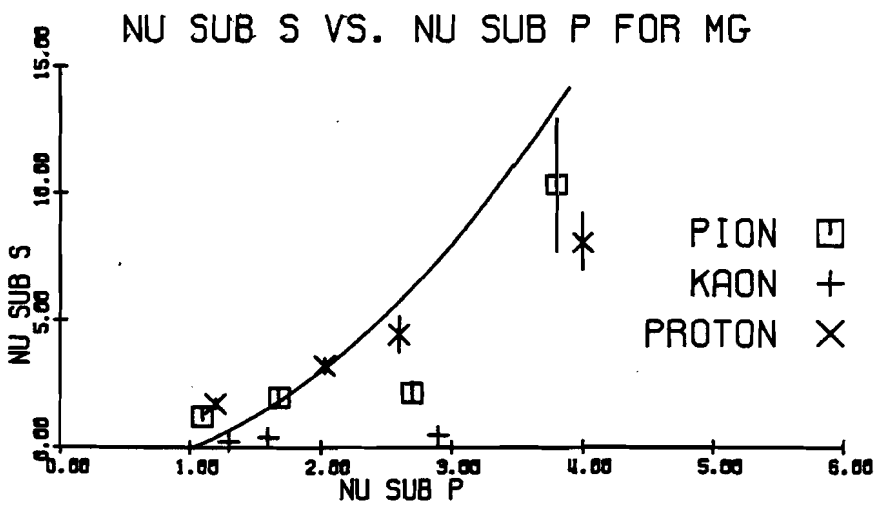

Figure 4-8a: Secondary collisions versus projectile collisions, Mg and Ag.

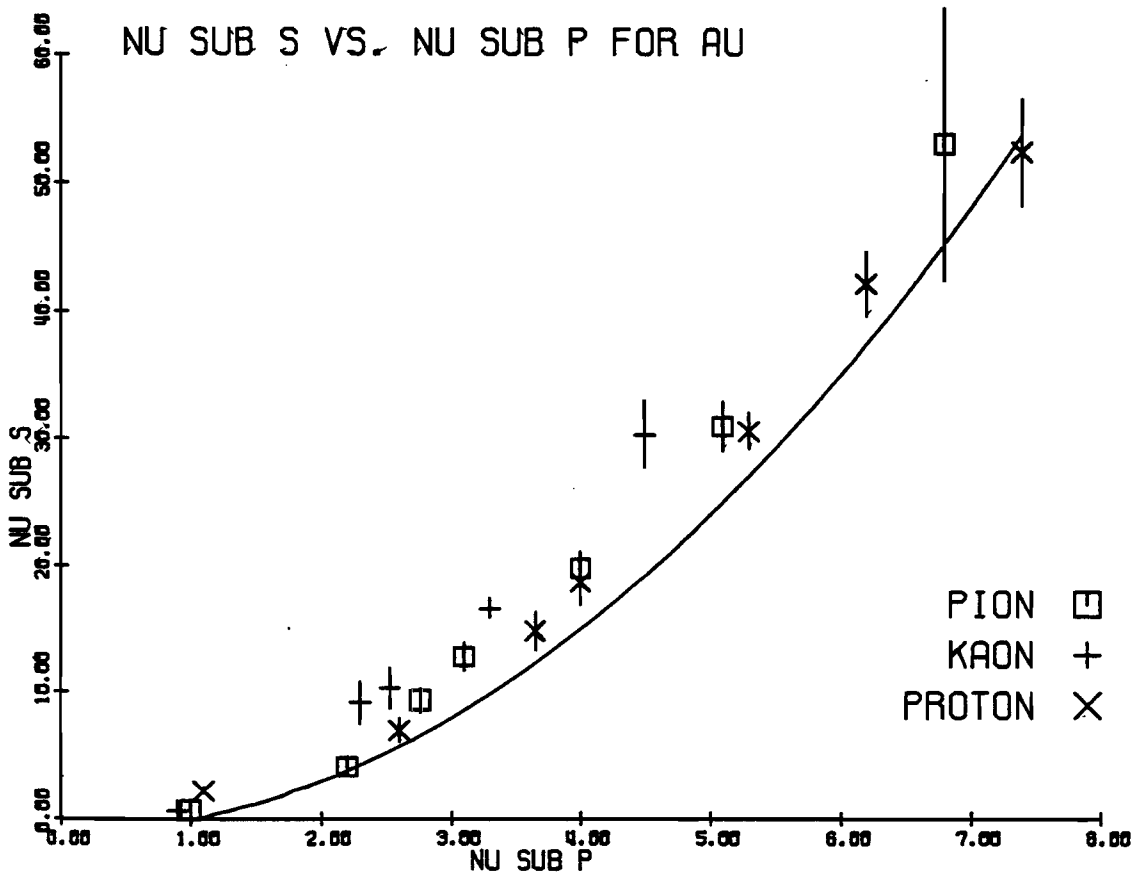

Figure 4-8b: Secondary collisions versus projectile collisions, Au.

4.6) RAPIDITY SHIFTS

In the introduction we discussed the secondary interactions in the nucleus in terms of the rapidity of the produced charged particles. The conclusions reached were that as A increases the number of secondaries should increase and this increase will be larger in the low rapidities where cascading can occur. Figure 4-9 shows the rapidities of charged pions normalized to the number of events for pions and protons on H_2, Mg, Ag, and Au. The same trends are seen in the kaon data but the statistics are much lower so this data is not reported. The rapidity is plotted in the center of mass (CM) with the target assumed to have a proton mass; the transformation to CM does depend on the mass of the beam. Identified protons and electrons are discarded but unidentified protons cannot be removed. Secondaries added during the ID scan (sec. 3.5) are not included as their momenta and angles are uncertain. Table 4-12 shows the average rapidity of the distributions in figure 4-9 as well as the kaon data averages.

We can make several observations from this figure and table. First, as expected, the multiplicity increases with A over most of the rapidity range. Above a rapidity of about 2 the curves cross over and the multiplicity decreases with A. Also the average rapidity shifts negative as we increase A. These features are seen in all of the reported experimental results.

All of these effects are due to the multiple collisions which are possible inside the nucleus. As described in the introduction, cascading of low momentum secondaries produces the large multiplicity increase at low rapidity. At higher rapidity the increased

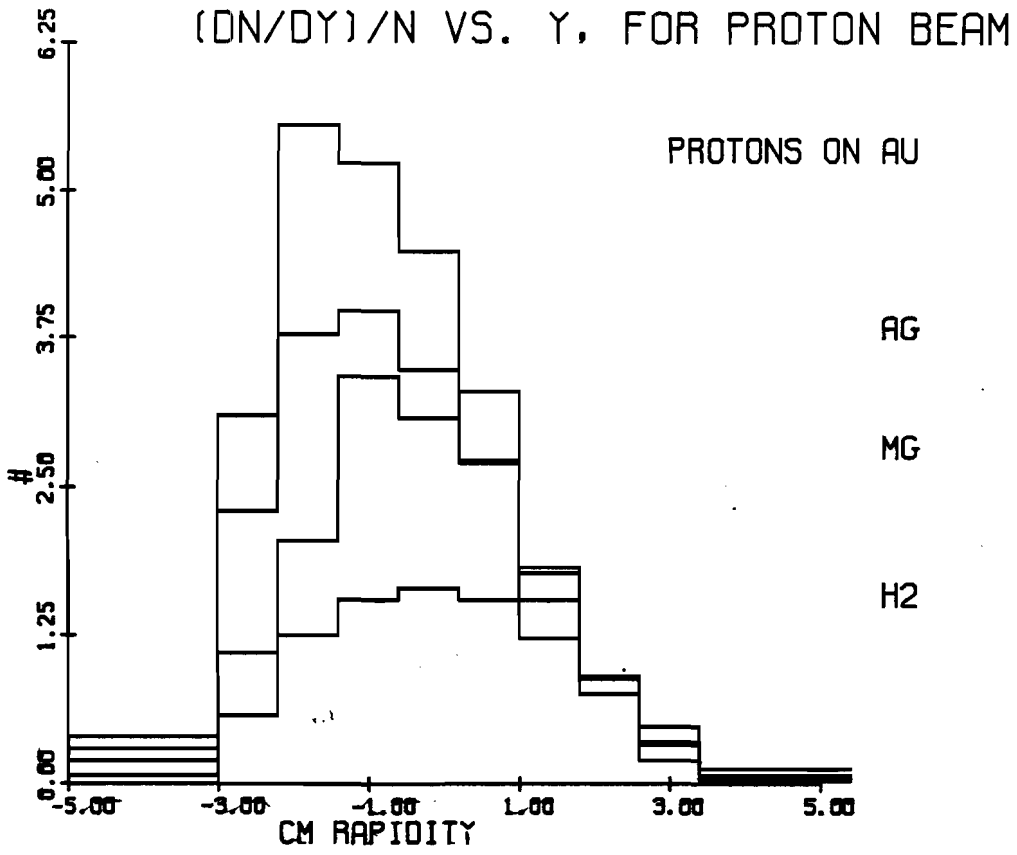

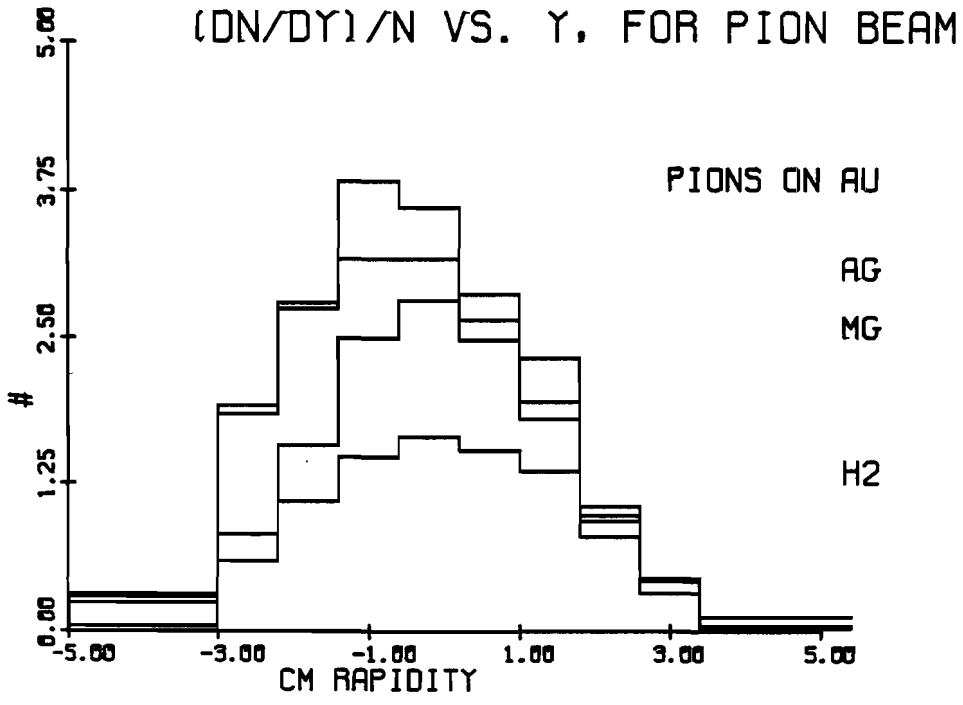

Figure 4-9: Normalized rapidity distribution for hydrogen, Mg, Ag, Au.

Element	π	K	p
Pions			
H_2	0.17 ± .04	0.18 ± .04	0.09 ± .03
Mg	-0.15 ± .08	-0.08 ± .12	-0.31 ± .06
Ag	-0.40 ± .05	-0.36 ± .08	-0.64 ± .04
Au	-0.48 ± .04	-0.47 ± .07	-0.76 ± .04
Protons			
Mg	-2.67 ± .05	-2.80 ± .10	-2.76 ± .04
Ag	-2.83 ± .02	-2.85 ± .03	-2.82 ± .02
Au	-2.82 ± .02	-2.86 ± .03	-2.84 ± .02

Table 4-12: Average rapidity for pions and protons.

multiplicity is due solely to multiple projectile collisions; recall that the fast secondaries cannot interact as they do not form until they are outside the nucleus. Even so, at each projectile collision more fast secondaries are formed, so in the middle rapidity range the multiplicity still increases with A. The projectile only has a finite amount of energy however and more projectile collisions will mean a lower average energy for the produced particles. Also the projectile itself is slowed down more by repeated collisions; thus the cross over of the curves at high rapidity.

The differences seen with beam type can also be explained by considering multiple collisions. We know (table 4-11) that incoming protons have more projectile collisions than pions and pions more than kaons. This is reflected again in figure 4-9 and table 4-12. The peak of the distributions are higher for protons and the shift of the average rapidity is greater than for pions. In fact if we plot the average rapidity versus $\langle \nu_p \rangle$ the result is consistent with a straight line, figure 4-10. At this level we cannot see any difference in the rapidity data for different beams that cannot be explained by considering only the average number of projectile collisions. With increased statistics we should notice a difference in the proton beam data due to its three quark structure; since there are three quarks their momentum on average should be lower than for quarks in mesons. This lower average momentum should be reflected in a greater shift to lower rapidity than would be expected just from considering the number of projectile collisions.

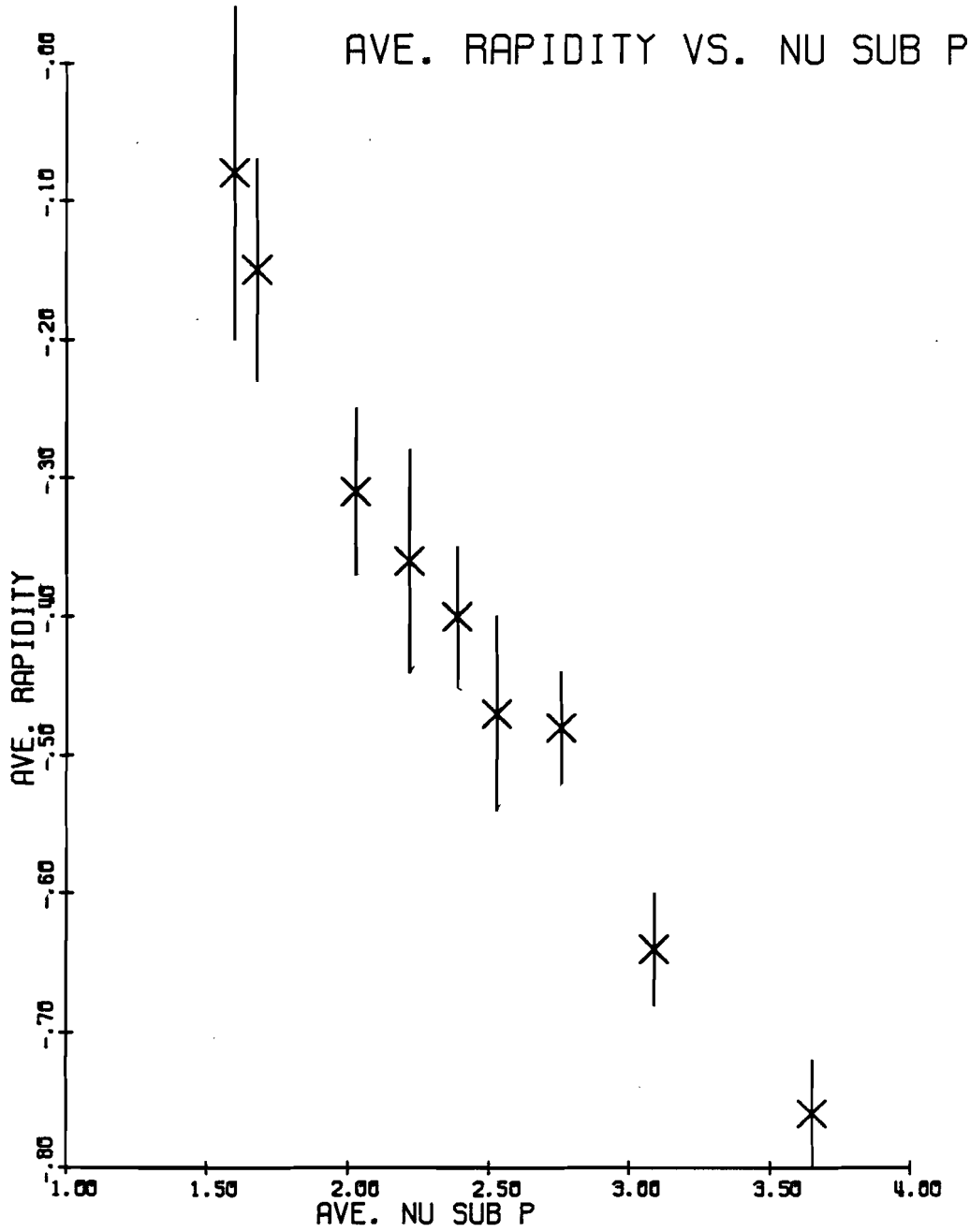

Figure 4-10: Average rapidity versus average projectile collisions.

5) CONCLUSION

We report on data from experiment 565/570 at Fermilab. The data were taken with the FNAL 30" bubble chamber and the Fermilab hybrid spectrometer. A beam of tagged π^+, K^+, and p at 200 GeV/c was used incident on targets of Mg, Ag, Au, and the H_2 in the bubble chamber. The upstream arm of the spectrometer provided beam tagging, while the downstream arm was used to improve the momentum measurement of fast secondaries.

Special procedures were used to process hadron-nucleus events with large multiplicities. These procedures included measuring the events in sections and using a modified chain of programs for the event reconstruction. Using these methods, described in previous chapters, we have produced a sample of 461 fully reconstructed hadron-nucleus events with small biases even in high mutiplicity events. Cross-sections are calculated for each beam and target type corrected for inelastic interactions with less than 4 charged tracks. These cross-sections are consistent with previously reported results.

The charged particle multiplicities are corrected for gamma ray conversions in the targets. An estimate is made of the correction for rejected events biased in multiplicity. In all cases this correction is less than one standard deviation. The trends seen in the average multiplicities are the same as have been reported before. Average multiplicity increases with A for a given beam type, and increases from kaon to pion to proton beam for a given A. Both of these features may be understood as an increase in the average multiplicity due to an increase in the average number of projectile collisions.

We examine the average net charge and average number of protons with no cutoff for low momentum secondaries. The momentum distribution of the average net charge over 4 GeV/c is similar to that in hadron-proton interactions. This result supersedes an earlier result published by this group which indicated a larger average net charge in hadron-nucleus events at high momentum. At low momentum, below 0.9 GeV/c, the average net charge is equal to and distributed in momentum just like the average number of protons. The average number of positive pions shows a different momentum distribution below 0.9 GeV/c and the average net charge of pions is approximately zero below 0.9 GeV/c. These facts lead us to conclude that below 0.9 GeV/c the average net charge is made up of protons, and not of produced pions. The lack of antiprotons in this momentum range indicates that these protons are being knocked out of the nucleus rather than being produced. Above 0.9 GeV/c we cannot efficiently identify protons but our data are consistent with the entire net positive charge being made up of slow protons except for a leading component which is similar to that seen in H_2 events.

Following the presciption of Chao, et al. we relate the number of projectile collisions to the number of protons observed in an event. The average multiplicity (corrected for gamma ray conversions) is linear with the number of projectile collisions out to $\nu_p = 7.7$. The slopes for each beam type are consistent with each other in our data. We do not see a larger slope in the kaon events than in the pion events as has been reported by the NA22 collaboration. The average net charge is not linear in the number of projectile collisions. This is expected since we know that the average net charge is mostly

observed protons and the number of projectile collisions goes like the square root of the number of protons. The number of secondary collisions versus the number of projectile collisions can be extracted from the average net charge distributions. It is clear from these curves that the number of secondary collisions depend on both beam and target type as well as on the number of projectile collisions. Averaged over beam and target type the data lies roughly along the curve $\nu_s = \nu_p^2 - 1$, Mg data is below this curve and Au data is above it when plotted separately. The large number of secondary collisions resulting from few projectile collisions can be understood in terms of the cascading of slow (in the lab frame) secondaries percolating out of the nucleus.

Rapidity distributions and rapidity shifts give a nice demonstration of the important features of hadron-nuceus interactions. Cascading slow secondaries produce or knock out large numbers of low rapidity particles. We have seen that the number of secondary collisions increases rapidly with the number of projectile collisions. We expect and observe increases at low rapidity as the average number of projectile collisions increases. At larger rapidity cascading is not possible but the projectile collisions themselves will still produce more secondaries. Finally, in the range of rapidity for leading particles, the curves cross over. Here the projectile will be slowed down more by each successive projectile collision and so the rapidity distribution will decrease with A.

We have seen that a simple intuitive picture can describe the broad features of hadron-nucleus interactions. This picture leads one to define variables like the number of projectile and secondary

collisions which can be used to clarify the data. What remains to be done is to relate this simple picture to a more realistic model of the interaction. Much more work, both in theory and experiment, must be done before this goal is realized.

APPENDICIES

A) PIG

The processor PIG is a new piece of software for E565/570, written at Rutgers by R. J. Plano and myself. The job of PIG is to reconstruct the path of charged particles through the downstream system. It was designed to replace the processors SEM and CEM used for similar purposes in the last experiment. Rather than just being an update of these two processors for our new setup, PIG uses a totally different approach to accomplish its task.

The components of the downstream spectrometer used here are the PWC's and DC's which will be referred to as wire chambers, and the CRISIS detector (see figure 2-5). Each wire chamber plane and CRISIS will have information from all the charged particles that traversed them during a timeslot, in addition to spurious data caused by oscillating wires, etc. To reconstruct a track PIG must decide which data from each device to associate together, i.e. which hits were made by that track. Then all these hits are combined to fit the trajectory of the particle. There is no magnetic field in the downstream arm so a charged particle will travel in a straight line. The way PIG works is to take a combination of hits and see if they fall along a straight line (within prescribed errors). Typical events will have over 100 hits in the fourteen chambers and several CRISIS tracks. To try all possible combinations of these hits while allowing for such things as chamber inefficiency and noise, would take an impossibly long time. Some algorithm must be found that reduces the number of combinations to examine without losing real tracks.

The method used is to first take a small number of hits with enough information to constrain a straight line fit. Different combinations are tried until a good fit is obtained. PIG then looks in a tube around the fitted line and picks up data inside from unused planes. The track is refit and the pickup is iterated until all data for the track are used. A new start combination is then chosen and the process continues until all start combinations have been tried. I will discuss the following aspects of PIG in detail:

- selecting the starting combination
- fitting a line to the data
- picking up associated hits
- dropping unassociated hits
- special handling for DC ghosts
- selecting good tracks
- reformatting for output.

To fit a straight line we need four parameters, the ones used in PIG are y, z, dy/dx, and dz/dx where y and z specify the position of the track at an arbitrary x coordinate called XOLINE. A hit in a wire chamber can be represented by a line in the yz plane (at the x of the chamber) which makes an angle β with the z axis (see ref. 41). β is the angle of the wires. The perpendicular distance from the hit wire to the x axis is called ρ and: $\rho = - y \sin(\beta) + z \cos(\beta)$. Each wire chamber plane used in the fit adds one constraint. A charged particle going through CRISIS produces a plane with an angle $(dy/dx)_{CR}$ and a position y_{CR} but no information on z. Thus a CRISIS plane adds two constraints to the fit. We have found it useful to also use the BC vertex (which has been reconstructed earlier in the program) to

help constrain the fit. Although a charged particle will bend in the magnetic field as it moves in the BC, the field is only in the z direction. So all bending is done in the xy plane. This means that the trajectory of the particle in the xz plane is still a straight line. We can use this information by treating the vertex as a wire chamber with its wires parallel to the y axis ($\beta = 90°$). In this case ρ is just the z of the vertex. Using the vertex in this way adds one constraint to the fit.

PIG has numerous starting options. By changing title parameters CRISIS can be used, the vertex "wire" can be used, the original number of wire chambers, which plane to start with, and which plane to end with can be selected. For example, in most of our running we used a CRISIS plane, the vertex, and two wire chamber planes. This gave us five constraints to fit the four parameters of the line. The wire chambers that we used were the three DC's in front of CRISIS. All combinations of hits from these three planes were taken two at a time (only one hit per plane is taken since the particle cannot produce two real hits in one plane). Any particle which left a hit in two out of three of these planes could then be reconstructed. Allowing more total planes causes you to miss fewer tracks due to inefficient chambers but the time required to cycle through all combinations grows geometrically with the number of hits in each additional plane. Taking a larger number of planes to start will cut down the cycle time but will cause more tracks to be missed due to inefficiency. Obviously the correct parameters to choose will depend on the number, placement and efficiency of the chambers used; that is why flexibility in this selection was built into PIG.

The track fit is a simple chi-squared fit to a straight line. Wire chamber terms have the form:

$$\chi^2 = \sum_i (\rho_i - (y_i \sin(\beta_i) + z_i \cos(\beta_i))^2 / \sigma_i^2)$$

$$\text{where } y_i = (x_i - \text{XOLINE})(dy/dx)_0 + y_0, \text{ and}$$

$$z_i = (x_i - \text{XOLINE})(dz/dx)_0 + z_0.$$

σ_i is the error which depends on the type of device being used. For CRISIS we add terms of the form:

$$\chi^2 = \frac{((dy/dx)_{cr} - (dy/dx)_0)^2}{\sigma_s^2} + \frac{(y_{cr} - y_i)^2}{\sigma_y^2} .$$

Note that the second term is just like a wire chamber term if $y_{cr} = \rho_i$ and the z components are ignored. Similarly, the angle term also has the same form but the slope appears in the position normally occupied by a coordinate. The initial hits are stored in a 4 X (number of constraints) matrix called DM. ρ for each hit is also stored in a vector. The components of DM are set up so that the product DM*DM' yields the derivative matrix for the fit. As more hits are picked up they are also stored in this way. Whenever a fit is desired the subroutine PCFIT is called. This subroutine inverts the derivative matrix and then finds parameters using the inverted matrix and the ρ vector. PCFIT also calculates and outputs the error matrix and the total chi-squared for the fit.

If the original fit with one set of initial hits is no good then that combination is discarded and the next set is tried. When an acceptable fit is found the pickup phase is entered. In this routine called PCPU we try to find hits other then the starting set which are associated with the track. If no hits can be found then the original fit probably did not represent a real track. In PCPU the parameters

of the straight line and their errors are known. The subroutine does a loop on all planes which have not yet been used. The track is propagated to each plane and a predicted ρ with errors is calculated. The program looks in the list of hits for that plane for hits in the range $\rho \pm C*d\rho$ where C is a constant set in the data bank (typically C=2). If there are no hits in the range it goes on to the next plane. If there is one hit, we store its parameters in DM and add 1 to the number of constraints. If there is more than one hit inside the range the plane is skipped until the errors of the fit are reduced. After all planes have been cycled through, the track is refit using PCFIT as before. This fit will have smaller track errors so after the fit PCPU is called again to see if any more hits can be added. This cycle continues until no more hits are picked up in PCPU.

Occasionally PCPU will pick up a point which does not really belong to the track. This can happen because the planes are somewhat inefficient (see ref. 22) and the density of hits in the plane can be large. That is, there is no hit where one should have been due to inefficiency, but there is a nearby hit which has nothing to do with the track we are seeking to reconstruct. In this case the chi-squared from the fit in PCFIT will usually be larger then expected. If so all hits are examined to see which one has contributed the largest to the chi-squared sum. That hit is deleted from the fit and it is marked so that it cannot be picked up again until a new initial combination is tried. PCFIT is redone without the bad point and the cycle continues. If all picked up points are discarded in this way than PIG will automatically jump to the next initial combination.

DC hits have an ambiguity as to which side of the sense wire they originated from. This left-right ambiguity is handled by treating each hit as two separate hits; the ghost hit should not fit any real track unless it is close to a sense wire and so adds to the processing time but does not hurt the final data. If the hit is close to the sense wire, the track parameters may never be good enough to exclude the ghost hit using the pickup procedure described in the last paragraph. Still we would like to use the real hit since it is good information. Planes where this is a problem are flagged in PCPU. After the track is otherwise complete the flagged planes are examined in turn. Each of the two possible hits is tried in the fit separately with the results being stored. The one which produces the lowest chi-squared is accepted.

We now have a track with some number of degrees of freedom and some chi-squared. We need to decide whether these hits are the best representation of the real charged track or if some other initial combination with slightly different positions is the real one. Well fit tracks with hits in almost all planes are necessarily correct. However because of the inefficiencies of our chambers not all secondaries produced hits in all planes. Also secondaries which exit the side of the spectrometer will be shorter. Spurious tracks can be generated out of hits which happen to lie along a line, or from hits that lie close to a real track if the wrong initial combination is taken; since the combinations are taken at random this cannot be avoided. These tracks will never have a large number of hits; unfortunately some of the short good tracks which we would like to get are indistinguishable from these spurious tracks. Also, once a track

is accepted its hits and CRISIS plane cannot be used again. So if a bad track is taken we will likely lose information on a good track.

If CRISIS is being used we can avoid this problem at the cost of processing time by trying all starting combinations for a given CRISIS plane. This works because CRISIS is very efficient due to its 192 cells along the track direction, and because there are very few spurious tracks in CRISIS. After each PCFIT, PCPU cycle for which some track was found this track is compared to the previous best track for that CRISIS plane. We keep the track with the larger number of degrees of freedom, or the lowest chi-squared if the number of constraints is the same. After all initial combinations have been tried the best track is accepted as correct.

If CRISIS is not being used the problem of spurious tracks cannot be completely solved. The program makes a cut and accepts any track with more than a certain number of constraints. These tracks must be taken in the order that they appear and so it is possible to accept a bad track which uses hits that belong to a real track. To help alleviate this problem two passes are made through the data, for each pass different criteria and initial parameters can be set up. During the first pass a more stringent criterion is used so that only real tracks will be accepted. Then the second pass is made with lower cuts; since hits that were used in the first pass are no longer available the chance for error is lessened.

Once a track is accepted its parameters and error matrix are stored in a DTF bank (see ref. 33) as in the old SEM, and CEM routines. In fact the output from PIG is indistinguishable from that of SEM and CEM except that the CRISIS data banks are linked to the DTF

structure so that the CRISIS ionization information is available for hybridized tracks.

As mentioned earlier (sec. 2.4) the use of PIG for this experiment enabled us to get the most tracking information out of our spectrometer consistent with the equipment that we had. In events where the downstream system was not totally flooded by data PIG found most of the tracks which entered CRISIS (events with too much data in the downstream system were not attempted because of time limitations). Figure A-1 shows the percentage of PIG hybridized tracks for all secondaries. The sharp cutoff at low momentum is due to tracks which do not enter the spectrometer. The actual efficiency of PIG is greater than shown in the plot as there was no subtraction for tracks which missed CRISIS, which CRISIS did not reconstruct, and which were found in PIG but not fit by GEOHYB.

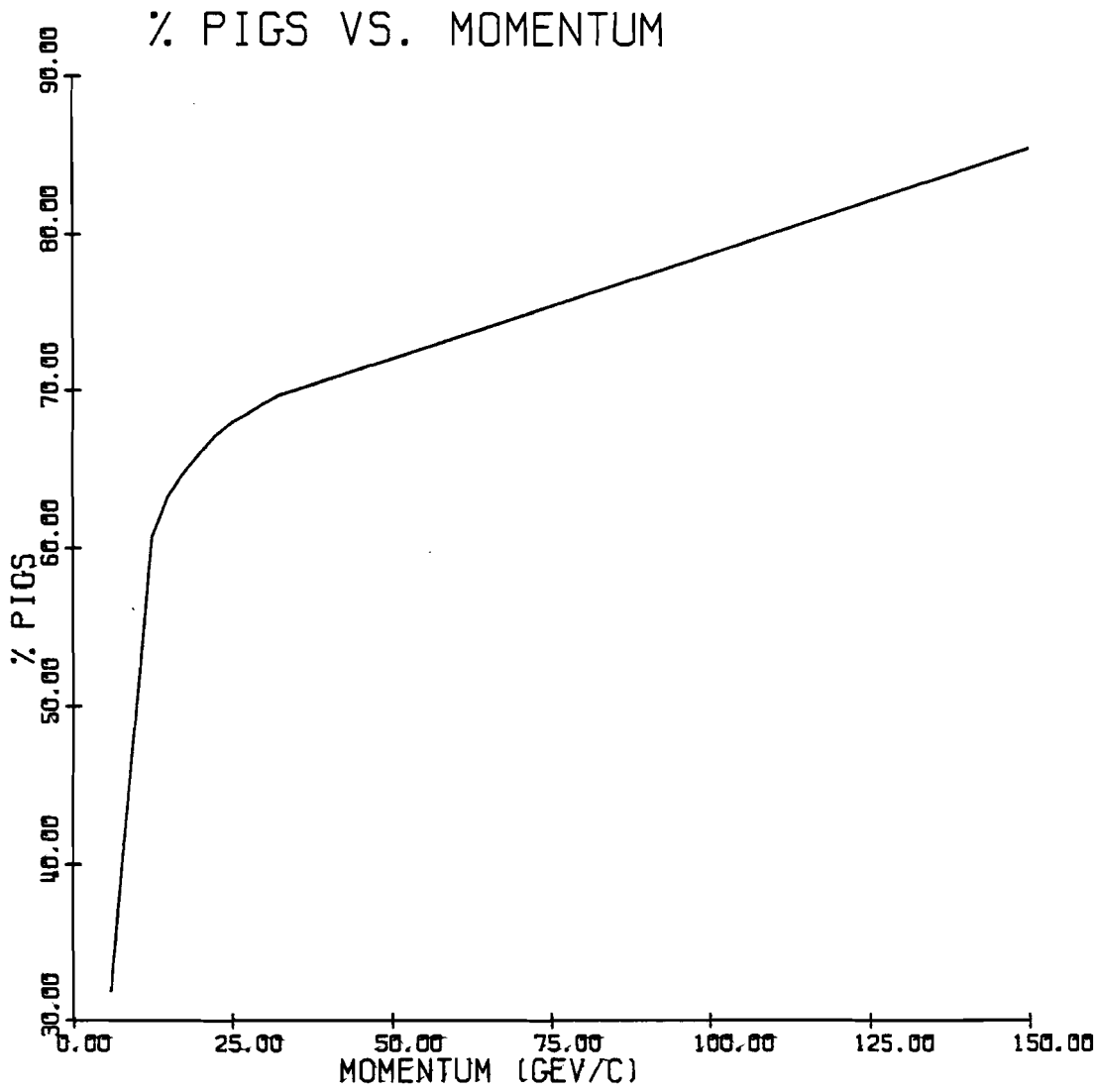

Figure A-1: PIG hybridizations.

B) SOW

The procesor SOW is a new piece of software for E565/570, written at Rutgers by R. J. Plano and myself. Unlike PIG, SOW is not a replacement of old GEOHYB parts, it is a new addition to GEOHYB. The job of SOW is to look at tracks which have been reconstructed using only BC track images but which should enter the downstream spectrometer. SOW tries to improve the track's parameters and reduce the errors using information from the downstream spectrometer that is left over after PIG. To do this SOW must:

- select tracks to try
- swim them into the spectrometer, with errors
- pick up associated hits in the spectrometer and refit
- perform final fit in the BC.

Each of these will be examined in turn.

SOW fits into GEOHYB after PIG and STDW2 have hybridized tracks in the normal way and after MIT has reconstructed the left over BC images (MIT is the processor that does track reconstruction using just the measured tracks in the BC). SOW is meant to work on tracks which entered the downstream spectrometer but were not PIG'ed because they did not reach CRISIS or because of inefficiencies in the programs. From the BC reconstructed tracks, SOW selects those whose momenta and angles are consistent with entering the spectrometer. Tracks which interact in the BC are noted at the IPD stage and these are discarded. Some of the left over tracks are ones which interacted in the BC exit window or somewhere in the spectrometer. These interactions cannot be

seen and the only way to tell these tracks is that they do not work in PIG or SOW.

For each accepted track SOW swims the track through the magnetic field into the spectrometer using the momentum and angles from MIT. Inside the BC the track is described by the vertex (XV, YV, ZV), and its inverse momentum (k), dip angle (λ), and phi angle (ϕ). In the spectrometer the variables used are y, dy/dx, and dz/dx evaluated at the x of the vertex XV. Since the magnetic field is parallel to the z axis there is no bending in the xz plane and z is 100% correlated with dz/dx and ZV. We know the error correlation matrix of the track in k, λ, and ϕ at the vertex. We need to know how this matrix transforms into a correlation matrix in y, dy/dx, and dz/dx outside the magnetic field. To find this matrix the track is swum through the magnetic field three more times with the parameters changed to k + dk, $\lambda + d\lambda$, and $\phi + d\phi$ in turn. The change in the parameters y, dy/dx, and dz/dx are found after each swim. A 3X3 matrix is set up with terms like dy/dk, $dy/d\lambda$, etc. This matrix, when multiplied into the error correlation matrix for k, λ, and ϕ in the BC, gives the error correlation matrix for y, dy/dx, and dz/dx in the spectrometer.

We now have a straight line and its errors outside the magnetic field. With a procedure similar to that used in PCPU the SWPU subroutine picks up hits in a tube around the fit line. A slightly different algorithm is used than in PCPU. For each plane if only one hit is inside the region then it is taken. If there is more than one hit (but not more than 3) the one closest to the prediction is taken, unless the plane is a drift chamber and there is a close "ghost" hit nearby. The reason for accepting the closest of several hits is that

the errors from the BC fit can be very large and accepting only unique hits would pick up very few hits.

After hits have been picked up there is a subroutine SWFIT which refits the parameters y, dy/dx, and dz/dx using the both the old values and the new constraints. As in PIG if the chi-squared for the fit is too large the hit with the largest chi-squared contribution is dropped. This hit is marked so that it cannot be used again. Because of the procedure described in the last paragraph bad hits are often picked up. Hits are dropped until a good fit is obtained. Then SWPU is called again and more hits can be tried. SWFIT and SWPU are cycled through until no more hits are picked up in SWPU.

We now have a BC track and a set of associated hits in the spectrometer. The fit in the spectrometer system is discarded at this point; it cannot be swum back into the BC because the momentum is not known. A new fit is done at the vertex in the BC. The original k, λ, and ϕ are added to the fit along with their error correlation matrix. Each picked up wire is then added to the fit. The error to be used for the wires is found by inverting the 3X3 matrix that we used to go from dk, $d\lambda$, and $d\phi$ to dy, d(dy/dx), and d(dz/dx). The details of this fit can be found in ref. 42.

When SOW is finished with a track the new track parameters are stored in its MF bank and a DTF bank is lifted with the spectrometer fit information. The hits used for the track are flagged and the hits that were dropped during the SWPU, SWFIT cycle are released to be used again. Then SOW goes on to the next BC track which enters the spectrometer.

SOW works well when it is used after PIG has hybridized most of the tracks and the only tracks left have lower momentum and miss CRISIS. SOW can also work by itself (without PIG) on clean events if the BC fits are good. However SOW does not work well by itself on complicated events. It is too easy to pick up the wrong hit on a crowded event, especially since the BC fits in these events are more likely to be incorrect or to have large errors. We are satisfied that the PIG-SOW combination used in E565/570 allowed us to use most of the information from our downstream spectrometer.

REFERENCES

1 W. Busza, Proceedings XV International Symposium on Multipartilcle Dynamics, Lund, 1984 (to be published).

2 N. N. Nikolaev, Sov. J. Part. Nucl. 12, 63 (1981).

3 M. K. Hegab and J. Hufner, Nucl. Phys. A384, 353 (1982).

4 Bo Andersson, Ingvar Otterlund, and Evert Stenlund, Phys. Lett. 73B, 343 (1978).

5 W. Q. Chao, M. K. Hegab, and J. Hufner, Nucl. Phys. A395, 482 (1983).

6 NA22 Collaboration, Proceedings XV International Symposium on Multipartilcle Dynamics, Lund, 1984 (to be published).

7 G. Berlad, A. Dar, and G. Eilam, Phys. Rev. D 13, 161 (1976).

8 K. Gottfried, Phys. Rev. Lett. 32, 957 (1974).

9 N. N. Nikolaev and A. Ya. Ostapchuck, CERN Report TH.2575-CERN, 1978 (unpublished).

10 A. Capella and J. Tran Thanh Van, Phys. Lett. 93B, 146 (1980).

11 A. Capella and J. Tran Thanh Van, Z. Phys. C 10, 249 (1981).

12 W. Busza, Acta Phys. Polon. B8, 333 (1977).

13 Ingvar Otterlund, Nucl. Phys. A418, 87c (1984).

14 D. H. Brick, et al., Nucl. Phys. B201, 189 (1982).

15 D. H. Brick, et al., Proceeding XIV International Symposium on Multiparticle Dynamics, Lake Tahoe, 1983, pg. 964.

16 W. M. Yeager, et al., Phys. Rev. D 16, 1294 (1977).

17 S. A. Azimov, et al., Phys. Rev. D 23, 2512 (1981).

18 W. D. Shephard, et al., Proceedings XIV International Symposium on Multiparticle Dynamics, Lake Tahoe, 1983, pg. 954.

19 C. DeMarzo, et al., Phys. Rev. D 26, 1019 (1982).

20 C. DeMarzo, et al., Phys. Rev. D 29, 2476 (1984).

21 A. Klar and J. Hufner, Phys. Rev. D 31, 491 (1985).

22 R. DiMarco, Rutgers Int. Note:RIHSC 82-16A, 1982, unpublished.

23 J. T. Bober, Ph.D. dissertation, M.I.T., 1984, unpublished.

24 A. M. Shapiro, et al., Rev. Sci. Instrum. 53, 393, (1982).

25 T. A. J. Frank, Ph.D. dissertation, M.I.T., 1985, unpublished.

26 F. Bruyant, EHS Software Note-EHS 790001, 1979, unpublished.

27 H. Taft and R. Steiner, "E570 Online Multi Modificatons", 20-April-1981, unpublished.

28 R. J. Plano, Rutgers Int. Note:RIHSC 82-7B, 1983, unpublished.

29 B. M. Whyman, Ph.D. dissertation, Univ. of Cambridge, 1980, unpublished.

30 Tungching Ou, Ph.D. dissertation, Rutgers Univ., 1979, unpublished.

31 HYDRA System Manual, doc. 79-5-12 d, CERN, 1979, unpublished.

32 H. Klein and J. Zoll, CERN Program Library: PATCHY Reference Manual, 1977, unpublished.

33 R. J. Plano, Rutgers Int. Note:RIHSC 82-12D, 1983, unpublished.

34 R. J. Plano, Rutgers Int. Note:RIHSC 82-13C, 1983, unpublished.

35 A. S. Carrol, et al., Phys. Lett. 80B, 319 (1979).

36 Z. Koba, et al., Nucl. Phys. B40, 317 (1972)

37 M. A. Faessler, Anal. of Phys. 137, 44 (1981)

38 P. Slattery, Phys. Rev. Lett. 29, 1624 (1972).

39 E. G. Boos, et al., Nucl. Phys. B137, 37 (1978).

40 J. Whitmore, Phys. Reports 10C, 273 (1973).

41 F. Bruyant, EHS Software Note-EHS 790012, 1979, unpublished.

42 R. J. Plano, Rutgers Int. Note:RIHSC 82-19A, 1982, unpublished.

VITA

Robert Louis DiMarco

1974	Graduated from South Brunswick High School, Monmouth Junction, New Jersey.
1974-78	Attended Rutgers College, Rutgers, the State University of New Jersey. Majored in Physics.
1978	B.A. Rutgers, the State University of New Jersey.
1978-85	Graduate work in Physics, Rutgers, the State University of New Jersey.
1978-82	Graduate fellow, Department of Physics.
1982	Teaching assistant, Department of Physics.
1982-85	Graduate assistant, Department of Physics.
1985	Ph.D. in Physics.